August 2014

Field and Analytical Studies of the First Folded Plate Girder Bridge

Man Hou Sit
University of Massachusetts Amherst

FIELD AND ANALYTICAL STUDIES OF THE FIRST FOLDED PLATE GIRDER BRIDGE

A Thesis Presented

by

MAN HOU SIT

Submitted to the Graduate School of the
University of Massachusetts Amherst in partial fulfillment
of the requirements for the degree of

MASTER OF SCIENCE IN CIVIL ENGINEERING

May 2014

CIVIL AND ENVIRONMENTAL ENGINEERING
STRUCTURAL ENGINEERING

FIELD AND ANALYTICAL STUDIES OF THE FIRST FOLDED PLATE GIRDER BRIDGE

A Thesis Presented

by

MAN HOU SIT

Approved as to style and content by:

_____
Scott A. Civjan, Chair

_____
Sergio F. Breña, Member

_____
Richard N. Palmer, Department Head
Civil and environmental engineering

ACKNOWLEDGMENTS

I would like to thank to my advisor, Dr. Scott A. Civjan, for his inclusive, patient guidance and support. I would also like to thank my committee members, Dr. Sergio Breña, for his thoughtful suggestion and assistance on the research. I would also like to extend my gratitude to all the people that have guided me and given me ideas on the research.

ABSTRACT

FIELD AND ANALYTICAL STUDIES OF THE FIRST FOLDED PLATE GIRDER BRIDGE

MAY 2014

MAN HOU SIT, B.S., NATIONAL CHENG KUNG UNIVERSITY, TAIWAN

M.S.C.E., UNIVERSITY OF MASSACHUSETTS AMHERST

Directed by: Associate Professor Scott A. Civjan

Integral abutment bridges are very common for short span bridges in the United State due to their less construction and maintenance cost and generally good performance. This thesis studies the first integral abutment bridge using Folded Plate Girder (FPG) Bridge System[1]. The bridge is instrumented with a variety of gauges to capture the behavior of the bridge, and a total of two year and one month [11/2011~12/2013] of data are collected and long-term data monitoring is performed. Live load test and long term temperature effect on the bridge are studied using finite element modeling and compared with actual field data. Girder strain/stress at mid-span and quarter-span and abutment rotations were investigated. From the result, first the bridge was found to show good performance. Shear lag effect was found to be happening at the bottom flange-to-web junction of the steel girder when subjected to concentrated loading. Thermal gradient was found to be significant on the girder strain and abutment rotations.

TABLE OF CONTENTS

Page

ACKNOWLEDGMENTS iii

ABSTRACT iv

LIST OF TABLES viii

LIST OF FIGURES x

CHAPTER

1 INTRODUCTION 1

1.1 Background 1
1.2 Scope of research 1

1.2.1 Bridge behavior and long term data monitoring 2

1.3 Literature review 2

1.3.1 Integral Abutment Bridge 2
1.3.2 Accelerated Bridge Program (ABP) 2
1.3.3 Folded Plate Bridge System 3
1.3.4 Hot-Dip Galvanizing coating 3
1.3.5 Shear Lag Effect 4

1.4 Actual bridge overview 6

1.4.1 Material properties 6
1.4.2 Section properties 7

1.5 Bridge instrumentation 12

2 FINITE ELEMENT MODELING 19

2.1 SAP2000 model 19

2.1.1 SAP2000 model testing 24

2.2 ANSYS APDL model 1 – shear lag model 25
2.3 ANSYS APDL model 2 – thermal behavior model 29
2.4 Soil properties and modeling 33

3 CONSTRUCTION AND SELF-WEIGHT EFFECT 36

3.1 Construction data 36
3.2 Maximum effects during bridge construction 36
3.3 Induced strain in deck due to girder self-weight 38

4 LIVE LOAD TESTING 40

4.1 Load test theoretical 2d moment calculation: 40
4.2 Effect of change in temperature during load test 44
4.3 Theoretical induced strain in deck and fpg due to load test: 45
4.4 Composite girder strain profile (at mid and ¼ span) 48

4.4.1 Summary 50

4.5 Moment distribution along the cross section (at mid and ¼ span) 55

5 SHEAR LAG EFFECT AT FPG 64

5.1 Live load testing (in selected live load positions) 64
5.2 Effect of bottom flange tie-plate 70
5.3 Comparison between wide flange steel girder 71
5.4 Shear lag effect under self-weight of bridge 73
5.5 Shear lag effect under thermal loading 75

6 LONG TERM MONITORING 78

6.1 Bridge temperature 78
6.2 Concrete strains 79

6.2.1 Concrete longitudinal strains 79
6.2.2 Concrete transverse strains 87

6.3 Folded Plate Girder steel strains 90
6.4 Bridge global effects 98
6.5 Summary 101

7 THERMAL BEHAVIOR 102

7.1 Parametric analysis models 102
7.2 Abutments rotation 109
7.3 Superstructure longitudinal strain 116

7.3.1 General behavior of thermal induced strain 116
7.3.2 Field data behavior 118

7.3.3 Parametric analysis result and comparison to field data 122
7.3.4 Daily temperature fluctuation 124
7.3.5 Summary of superstructure longitudinal strain 135

8 BRIDGE PERFORMANCE 136

9 CONCLUSION 142

BIBLIOGRAPHY 144

LIST OF TABLES

Table Page

Table 1-1 Coefficient of Thermal Expansion 7

Table 1-2 Section Properties of bare steel girder FPG 11

Table 1-3 Section Properties when closure pour is not included 11

Table 1-4 Section Properties when closure pour is included 12

Table 1-5 Gauge division w.r.t. depth from top of deck 13

Table 2-1 Material properties of the SAP2000 model 20

Table 2-2 Summary of SAP2000 FEM 22

Table 2-3 Joint number corresponding to deck gauges positions 23

Table 2-4 Hand calculations of self-weight of SAP2000 bridge model 25

Table 2-5 Reactions at supports due to self-weight only and self-weight plus 100k 25

Table 2-6 Material properties of the bridge used in the ANSYS model 27

Table 2-7 Soil Properties used in FEM 34

Table 3-1 Construction Reading Descriptions 37

Table 3-2 Construction Maximum Effects 37

Table 3-3 Theoretical longitudinal strain induced at mid-span due to self-weight 39

Table 4-1 Live Load Test Maximum Effects 40

Table 4-2 Concentrated load P position and far end reaction R 42

Table 4-3 Calculated moment in mid-span and ¼-span 42

Table 4-4 Induced strain in deck and FPG due to Load test at mid-span 46

Table 4-5 Induced strain in deck and FPG due to Load test at ¼ span 47

Table 4-6 Elastic neutral axis of each girder based on strain gauge readings 56

Table 4-7 Increment region on each girder 57

Table 4-8 Actual moments at mid-span compared with FEM results and hand calculation. 58

Table 4-9 Actual moments at ¼ -span compare with FEM results and hand calc. 58

Table 5-1 Predicted strain values at web-to-flange junction for test Position 4 67

Table 5-2 Comparison between model with and without bottom flange tie-plates 71

Table 6-1 Gauges Used for Temperature Calculation 78

Table 6-2 Concrete strain readings of precast deck and closure pour before the record of long term data at mid-span 81

Table 6-3 Concrete strain readings of precast deck and closure pour before the record of long term data at quarter-span 82

Table 7-1 Soil properties of backfill and soil around piles 106

Table 7-2 Temperature values used in the parametric analysis 106

Table 7-3 Summary of different models used in parametric analysis 107

Table 7-4 Parametric analysis abutment rotation results 116

Table 7-5 Maximum strain readings at different locations 122

Table 7-6 Parametric analysis longitudinal strain results at interior girders 123

Table 7-7 Parametric analysis longitudinal strain results at exterior girders 123

Table 7-8 Difference between parametric results in interior and exterior girders 124

Table 7-9 FPG strain field data 124

Table 7-10 Field data readings and ANSYS results of Girder 3 at the 4 points of the daily cycle in summer 133

Table 7-11 Field data readings and ANSYS results of Girder 3 at when maximum compressive strain is recorded at spring 133

LIST OF FIGURES

Figure Page

Figure 1-1 Standard FPG section 5

Figure 1-2 Actual FPG section 5

Figure 1-3 Typical shear lag on Box Girder under bending: (a) Positive Shear Lag, (b) Negative Shear Lag (Chang and Zheng, 1987) [With permission from American Society of Civil Engineers, this material may be downloaded for personal use only. Any other use requires prior permission of the American Society of Civil Engineers.] 5

Figure 1-4 FPG unit elevation (Reproduced by permission of MassDOT) 7

Figure 1-5 Plan view of concrete deck (Reproduced by permission of MassDOT) 8

Figure 1-6 Entire bridge section at mid-span (Reproduced by permission of MassDOT) 8

Figure 1-7 Abutment elevation and plan (Reproduced by permission of MassDOT) 9

Figure 1-8 Abutment sections (Reproduced by permission of MassDOT) 10

Figure 1-9 Gauges located on abutments (elevation view) 14

Figure 1-10 Bridge instrumentation overview 15

Figure 1-11 Instrumented mid-span and quarter-span sections 16

Figure 1-12 Location of deck strain gauges 17

Figure 1-13 Location of FPG strain gauges 18

Figure 2-1 Insert point of FPG girders in SAP2000 in extrude view 20

Figure 2-2 Isometric views of bridge model in SAP2000 20

Figure 2-3 Meshing of East, West abutment, and deck after auto-meshing in SAP2000 21

Figure 2-4 Plan view of 100k concentrate joint force applied at the lower right corner of top of the deck 24

Figure 2-5 Isometric view of ANSYS model 1 27

Figure 2-6 Section view of ANSYS model 1 28

Figure 2-7 Close-up exterior section view of ANSYS model 1 28

Figure 2-8 Loading condition of Position 4 in ANSYS model 1 29

Figure 2-9 Isometric view of ANSYS model 2 with lower abutments modeled with shell elements 31

Figure 2-10 Side view of ANSYS model 2 with lower abutments modeled with shell elements 31

Figure 2-11 Isometric view of ANSYS model 2 with abutments modeled with solid elements 32

Figure 2-12 Sample thermal gradient at the superstructure and the abutments 32

Figure 2-13 East (West) abutment and pile soil springs elevation 35

Figure 3-1 Load condition and moment diagram under self-weight of girder 39

Figure 4-1 Single load acting on fixed end beam 41

Figure 4-2 Live load test Positions 1 to 9 43

Figure 4-3 Live load test Positions 10 to 13 44

Figure 4-4 Stress distributions on a section due to concentrated load based on the distance to location of load 50

Figure 4-5 Strain profile along the depth of each girder at mid-span in Positions 1~7 52

Figure 4-6 Strain profile along the depth of each girder at mid-span in Positions 8~14 53

Figure 4-7 Strain profile along the depth of each girder at quarter-span 54

Figure 4-8 Illustration of calculation force profile from strain profile 56

Figure 4-9 Transverse distribution of longitudinal moment at mid-span in Pos1~7 61

Figure 4-10 Transverse distribution of longitudinal moment at mid-span in Pos8~14 62

Figure 4-11 Transverse distribution of longitudinal moment at quarter-span 63

Figure 5-1 ANSYS result query path and legend of strain profile plots used in this Chapter 68

Figure 5-2 Mid-span longitudinal strain distribution in Position 4 68

Figure 5-3 Strain distribution versus gauges locations 68

Figure 5-4 Mid-span strain profile plots of Pos3, Pos4 and Pos7 69

Figure 5-5 Quarter-span strain profile plots of Pos3, Pos4 and Pos7 69

Figure 5-6 Longitudinal strain on FPG bottom flange of Girder 2 due to Live Load Position 4 70

Figure 5-7 Comparison between model with and without bottom flange tie-plates 71

Figure 5-8 Section view of the modified ANSYS model 72

Figure 5-9 Strain distribution of FPG and w-shape steel under Position 4 load conditions 72

Figure 5-10 Strain profile of FPG and w-shape steel under Position 4 load conditions 73

Figure 5-11 Longitudinal strain distribution of cross-section due to self-weight effect at mid-span 74

Figure 5-12 Strain profile of interior and exterior section at mid-span due to self-weight effect 74

Figure 5-13 Longitudinal strain on FPG bottom flange of Girder 2 due to self-weight effect 75

Figure 5-14 ANSYS strain profile results under different thermal loadings 76

Figure 5-15 Longitudinal strain on FPG bottom flange of Girder 2 due to thermal loading 77

Figure 6-1 Bridge temperature 79

Figure 6-2 Precast deck embedded concrete longitudinal strain gauges 82

Figure 6-3 Precast deck embedded concrete transverse strain gauges 82

Figure 6-4 Closure pour embedded concrete longitudinal and transverse strain gauges 83

Figure 6-5 Girder Concrete Longitudinal Strains at Mid-span....84
Figure 6-6 Girder 2 Concrete Longitudinal Strains at Mid-span....84
Figure 6-7 Girder 3 Concrete Longitudinal Strains at Mid-span....85
Figure 6-8 Girder 4 Concrete Longitudinal Strains at Mid-span....85
Figure 6-9 Girder 3 Concrete Longitudinal Strains at Quarter-Span....86
Figure 6-10 Girder 4 Concrete Longitudinal Strains at Quarter-Span....86
Figure 6-11 Precast Concrete Transverse Strains at Mid-span....88
Figure 6-12 Closure Pour Concrete Transverse Strains at Mid-span....88
Figure 6-13 Precast Concrete Transverse Strains at Quarter-Span....89
Figure 6-14 Closure Pour Concrete Transverse Strains at Quarter-Span....89
Figure 6-15 Steel FPG longitudinal strain gauges....92
Figure 6-16 FPG bottom flange tie-plate transverse strain gauge and displacement transducer on Girder 3....92
Figure 6-17 Plan view of bridge showing locations of transverse strain gauges on tie-plates and displacement transducer between bottom flange....93
Figure 6-18 Girder 1 FPG Bottom Flange Strain at Mid-span....93
Figure 6-19 Girder 2 FPG Bottom Flange Strain at Mid-span....94
Figure 6-20 Girder 3 FPG Bottom Flange Strain at Mid-span....94
Figure 6-21 Girder 4 FPG Bottom Flange Strain at Mid-span....95
Figure 6-22 Girder 3 FPG Bottom Flange Strain at Quarter-Span....95
Figure 6-23 Girder 4 FPG Bottom Flange Strain at Quarter-Span....96
Figure 6-24 Difference between bottom flange reading at mid-span and quarter-span....96
Figure 6-25 FPG Girder Tie Plate Transverse Strain....97
Figure 6-26 FPG Bottom Flange Transverse Displacements....97
Figure 6-27 Abutment rotation tilt-meter....99

Figure 6-28 Retaining wall transverse displacement transducer 99

Figure 6-29 Abutment rotations 100

Figure 6-30 Abutment Displacements 100

Figure 7-1 Average FPG and concrete deck temperature 107

Figure 7-2 Temperatures of different gauges during the hottest days of 2013 108

Figure 7-3 Temperatures of different gauges during the coldest days of 2013 108

Figure 7-4 Abutments rotation plotted against ambient temperature change 113

Figure 7-5 Abutments rotation plotted against increasing and decreasing instantaneous temperature change 114

Figure 7-6 Comparison between parametric analysis result and west abutment field rotation readings 115

Figure 7-7 Comparison between parametric analysis result and east abutment field rotation readings 115

Figure 7-8 Example of different parts of strain under thermal loading 118

Figure 7-9 Example of thermal expansion without end restraint 118

Figure 7-10 FPG longitudinal strain Girder 1 and Girder 2 plotted against ambient temperature change 120

Figure 7-11 FPG longitudinal strain at Girder 3 and Girder 4 plotted against ambient temperature change 121

Figure 7-12 Longitudinal strain readings of girder 1 during the hottest and coldest 5 days in each year alongside with the temperatures fluctuation 126

Figure 7-13 Longitudinal strain readings of girder 2 during the hottest and coldest 5 days in each year alongside with the temperatures fluctuation 127

Figure 7-14 Longitudinal strain readings of girder 3 during the hottest and coldest 5 days in each year alongside with the temperatures fluctuation 128

Figure 7-15 Longitudinal strain readings of girder 4 during the hottest and coldest 5 days in each year alongside with the temperatures fluctuation 129

Figure 7-16 Maximum longitudinal FPG strain readings alongside with the temperature 130

Figure 7-17 The 4 points on the daily cycle 133

Figure 7-18 Strain profiles of field data and ANSYS results of Girder 3 at the 4 points of the daily cycle 134

Figure 7-19 Strain profiles of field data and ANSYS results of Girder 3 at when maximum compressive strain is recorded at spring 135

Figure 8-1 Cracks found on the concrete deck 137

Figure 8-2 Cracks locations and dimensions 138

Figure 8-3 Leakage from top of deck to FPG 139

Figure 8-4 Rusts found at the bottom of FPG 140

Figure 8-5 Upper abutments to lower abutments interface condition 140

Figure 8-6 Closure pour condition 141

CHAPTER 1
INTRODUCTION

1.1 Background

Many short-span bridges (20 to 125 foot [6 to 38 m] in length[2]) in the United State are aging and becoming structurally and functionally deficient. According to the U.S. Government Accountability Office[3] (U.S. GAO), one in four bridges in the United States is either structurally deficient and in need of repair. Therefore, it is essential to develop economic alternatives to current bridges that can be constructed using light construction equipment and have a long service life. One possible alternative is the Folded Plate Girder (FPG) Bridge System[4], which is an innovation type of prefabricated girder section. In the case studied it incorporates precast, post-tensioned integral abutments for additional construction efficiency and durability. The bridge has been instrumented to allow comparison between field data and expected performance based on calculations and analytical models. Future design and implementation of this innovative new bridge system will benefit from an independent verification of system performance as provided in this research.

1.2 Scope of research

This thesis research analyzed the FPG bridge system to address any design issues and verify field performance. The behaviors of the bridge under live load testing and long-term thermal loading were investigated.

1.2.1 **Bridge behavior and long term data monitoring**

The FPG Bridge being studied is the first of its kind ever constructed and is located in Uxbridge, MA. The bridge is instrumented with a variety of gauges (stain gauges, displacement transducers, tiltmeters, and pressure cells) to monitor the actual behavior of the bridge. Instrumentation will be described in Section 1.5. Hand calculations and Finite Element Models (FEM) developed in SAP2000 and ANSYS were used to analyze the behavior of the bridge during construction, live load testing, and seasonal thermal load stages. Actual field data were used to validate the analytical results.

1.3 Literature review

1.3.1 **Integral Abutment Bridge**

Integral Abutment Bridges are bridges with the superstructure rigidly connected to the abutments without any expansion joint in order to eliminate the long term expansion joint/bearing problems. Due to their well-established advantage of reducing maintenance costs, integral abutment bridges have become a popular bridge type and are widely used in highway departments' design.

1.3.2 **Accelerated Bridge Program (ABP)**

ABP[5] represent a monumental investment in Massachusetts bridges signed into law by Governor Deval Patrick in August 2008. The goal of the program is to

improve the condition of the Commonwealth's bridges by reducing the number of structurally deficient bridges in the state. In this program, accelerated bridge construction that involved a lot of prefabrication and innovative techniques is normally used. The FPG system is one of the innovative techniques used in the program. One of the objectives of the program is to provide faster construction experience and less maintenance cost.

1.3.3 **Folded Plate Bridge System**[4]

The FPG system is an economical and innovative bridge system for bridges up to 60 foot in length. In this system, the deck is precast on the girder as a single composite girder unit in the factory and this provide a fast construction process. The girders used in the system is the folded plate girder (FPG), which built by bending flat plates into inverted tub sections, Figure 1-1 and Figure 1-2 show standard schematic and as-built FPG section, respectively. This type of girder can easily accommodate different span length requirements by changing bending locations to obtain the suitable width of the top and bottom flanges and the depth of the web while keeping the plate thicknesses to either 3/8 inch [0.95 cm] or 1/2 inch [1.27 cm] Besides, the FPG steel girder went through a process called "hot-dip galvanizing" before erection to obtain a superior level of corrosion resistance.

1.3.4 **Hot-Dip Galvanizing coating**

Hot-dip galvanizing (HDG) is a process provided by American Galvanizers Association (AGA)[6] to provide superior corrosion resistant to steel. In the process,

first dirt and grease on the steel surface are removed by using caustic or degreasing solution. Second, the steel goes through a process called “pickling”, in which oxides and mill scales on the steel are removed by submerging the steel into either hydrochloric or sulfuric acid. Last, the steel is then dipped into molten zinc and a hot-dip galvanized coating (strong metallic bond is formed between the molecules of the zinc and the steel) is formed on the steel surface. Under corrosion, the zinc in the hot-dip galvanized coating forms an adherent corrosion byproduct – a protective surface layer of oxide and carbonate, which will slow down the corrosion process and protect the steel from oxidization.

1.3.5 **Shear Lag Effect**

Shear Lag Effect is used to describe the phenomenon that shear deformation at the flange of a beam will cause non-uniform longitudinal stress/strain distribution along the flange. Shear Lag is a concern in Wide Box Girder[7] as it will lead to stress concentration at the web-to-flange intersection, and it will increase when the width of the girder increase. (Mohannad and Ghaidak, 2012) [7]

There are two type of shear lag effect. One is called Positive Shear Lag, where the longitudinal bending stress/strain at web-to-flange intersection is larger than that at the mid-point of the flange [Figure 1-3 (a)]. The other one is called Negative Shear Lag, where the longitudinal bending stress/strain at web-to-flange intersection is smaller than that at the mid-point of the flange [Figure 1-3 (b)]. (Chang and Zheng, 1987)[8]

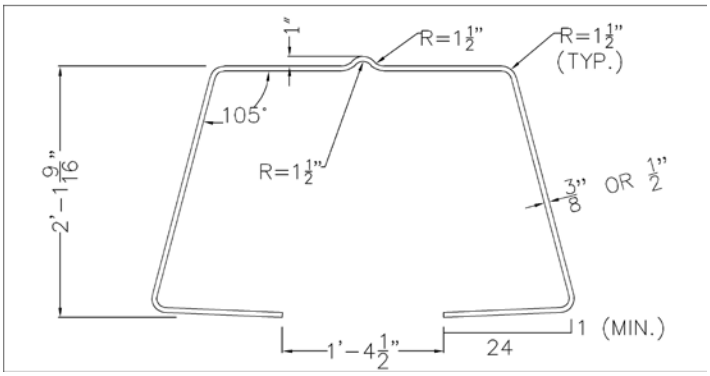

Figure 1-1 Standard FPG section

Figure 1-2 Actual FPG section

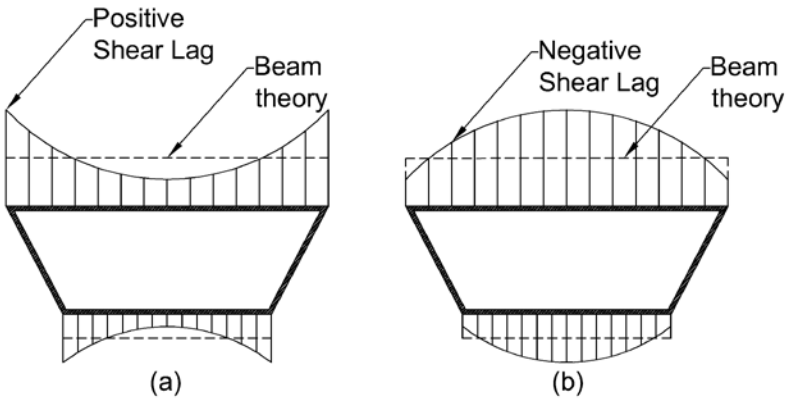

Figure 1-3 Typical shear lag on Box Girder under bending: (a) Positive Shear Lag, (b) Negative Shear Lag (Chang and Zheng, 1987)[8] [With permission from American Society of Civil Engineers, this material may be downloaded for personal use only. Any other use requires prior permission of the American Society of Civil Engineers.]

1.4 Actual Bridge Overview

The actual FPG steel bridge was constructed in Uxbridge, Massachusetts. The bridge included precast, post-tensioned integral abutments supported by four H-piles at each abutment. The bridge consists of four FPG with precast concrete deck on top, numbered Girder 1 to 4 from North to South. The girders were placed side by side on the abutments, and were connected by cast-in-place closure pours between the concrete slabs, numbered closure pour 1 to 3 from North to South. The bridge includes precast, post-tensioned lower abutments with cast in place upper abutments providing integral abutment response. For complete details, Figure 1-4 shows the elevation of a single FPG unit which indicates the location of bottom flange tie-plates, Figure 1-5 shows the plan view of the concrete deck, Figure 1-6 shows the bridge section, Figure 1-7 shows the plan and elevation views of abutments, and Figure 1-8 shows the abutment sections.

1.4.1 Material properties

Material properties that were used for the data analysis are shown in this section. The assumed coefficient of thermal expansion for all materials is shown in Table 1-1. The yield strength of steel girder is 50 ksi [345 MPa], the modulus of elasticity of steel and concrete are $29x10^3$ ksi [$200x10^3$ MPa] and $3.8x10^3$ ksi [$26.2x10^3$ MPa] respectively. Note that the modulus of elasticity of concrete are calculated based on assumed values 150 pcf [23.6 kN/m^3] for unit weight and compressive strength of f'_c = 4000 psi [27.6 MPa].

Table 1-1 Coefficient of Thermal Expansion

Material	Coefficient of Thermal Expansion [με /°F (με /°C)]
Steel Girder	6.78 (12.2) [1]
Concrete	5.78 (10.4) [1]
Steel Vibrating Wire	6.78 (12.2) [1]

- [1] Values for the Coefficient of Thermal Expansion (CTE) of steel, concrete, and the steel vibrating wire were provided in the Geokon instrumentation manuals.

1.4.2 Section properties

Section properties of the bare steel FPG are provided in Table 1-2. Section properties of the composite section of the FPG and concrete deck were computed for two conditions: when closure pour is included and when it is not included. This is done because the closure pour was cast in place, section properties without the presence of closure pour will be used in dead load analysis of which data are recorded before the closure pouring, whereas properties with the presence of closure pour will be used in live load testing stage. The calculation of composite section properties was done by transforming the concrete deck into equivalent steel sections. The results of the composite section properties under the two conditions are shown in Table 1-3 and Table 1-4. Note that the sections were modified to have sharp angles in the calculation.

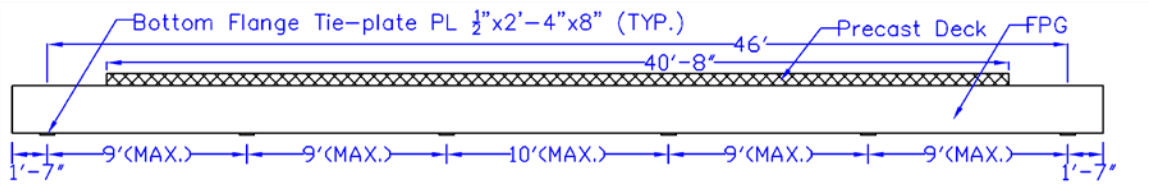

Figure 1-4 FPG unit elevation (Reproduced by permission of MassDOT)

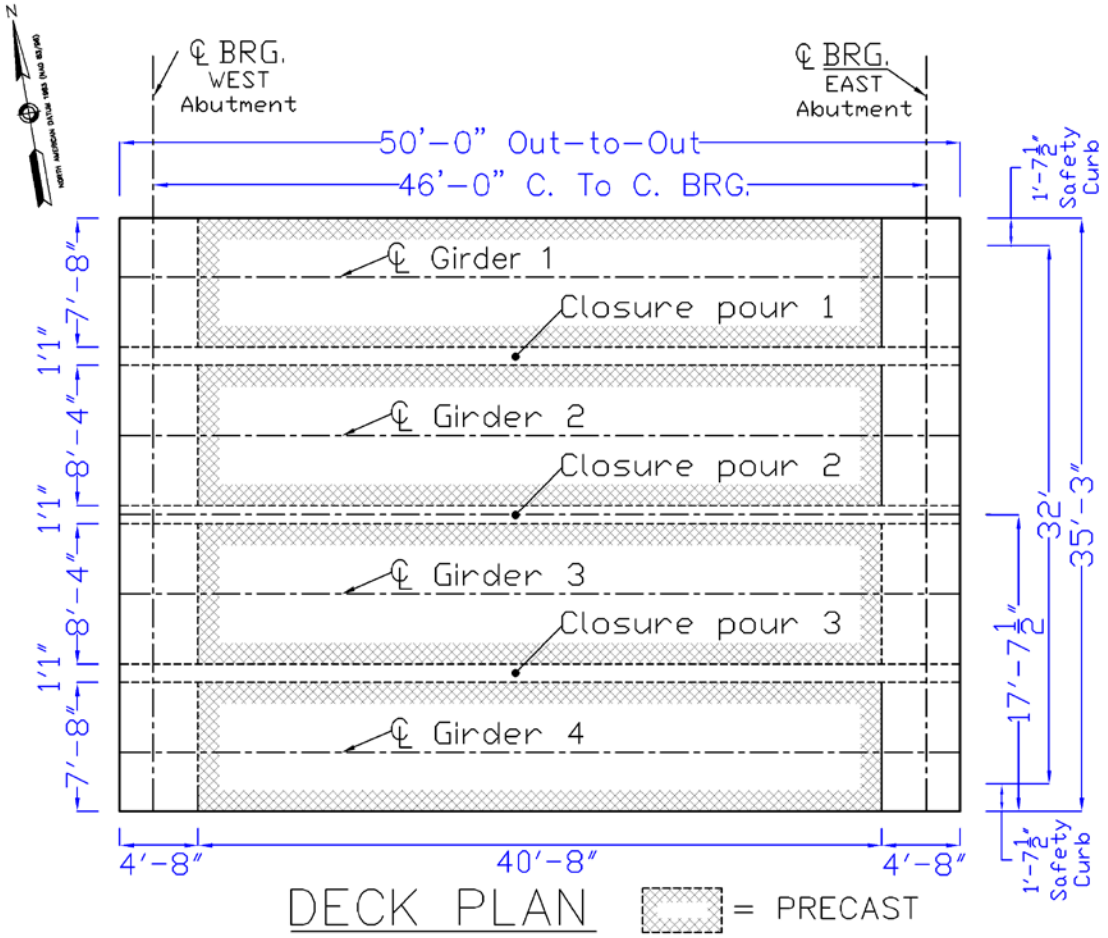

Figure 1-5 Plan view of concrete deck (Reproduced by permission of MassDOT)

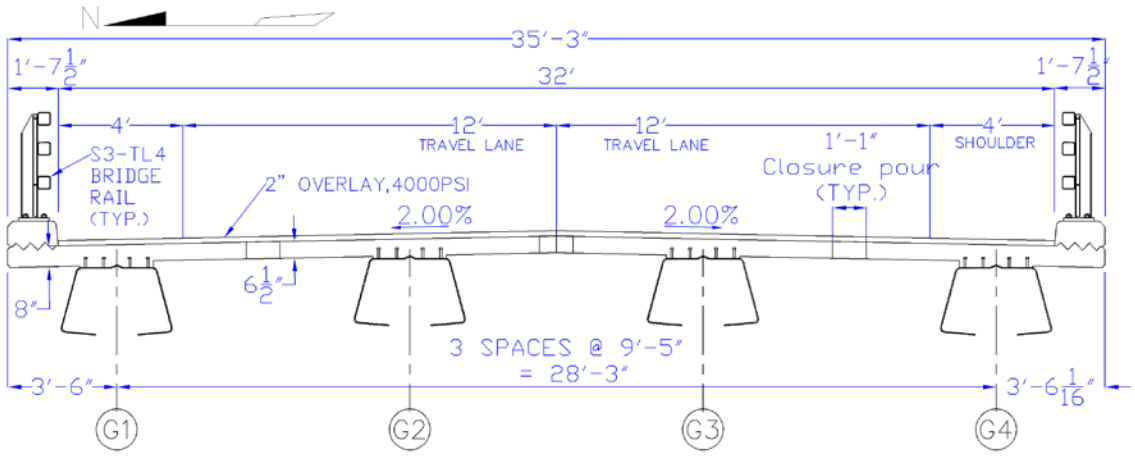

Figure 1-6 Entire bridge section at mid-span (Reproduced by permission of MassDOT)

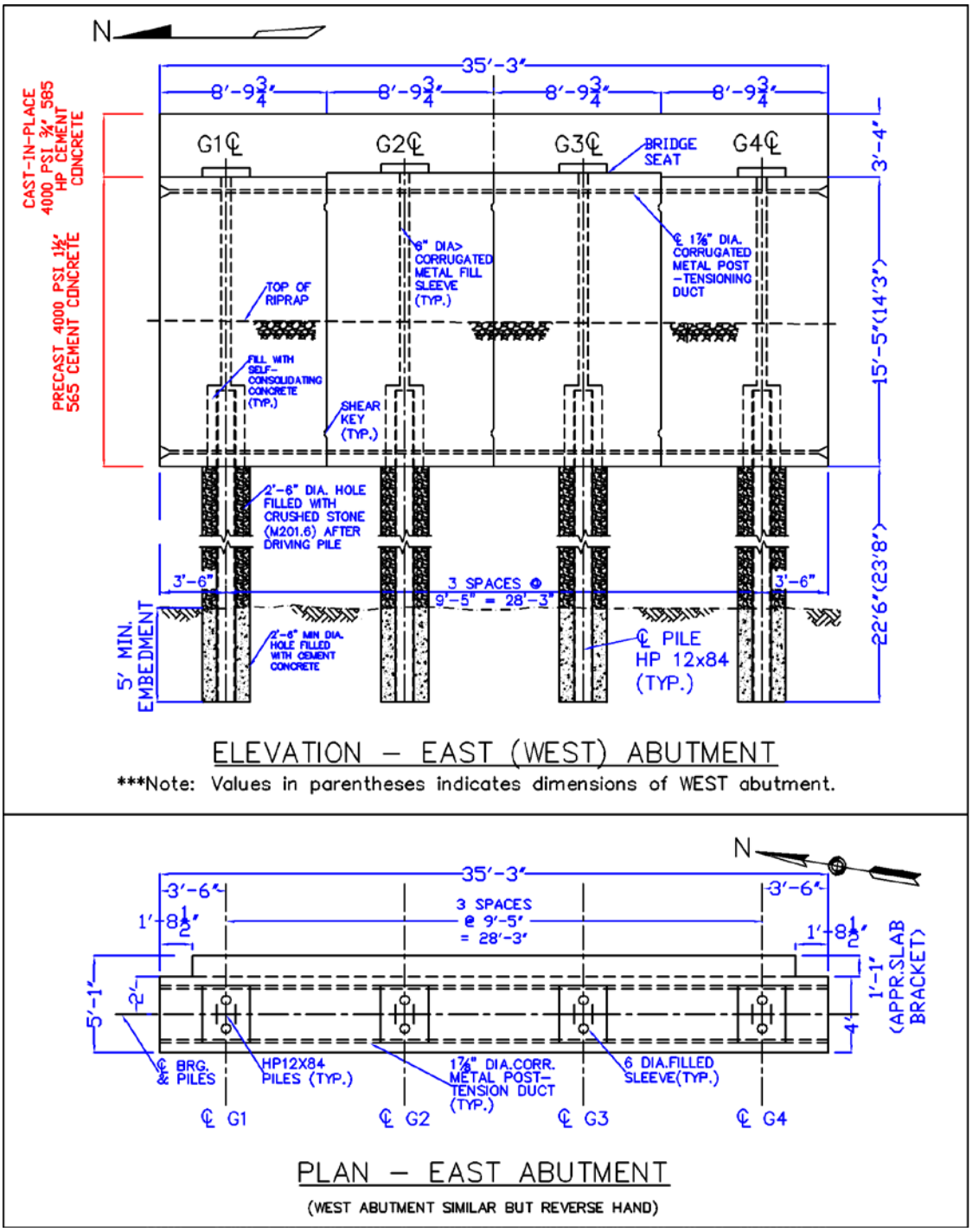

Figure 1-7 Abutment elevation and plan (Reproduced by permission of MassDOT)

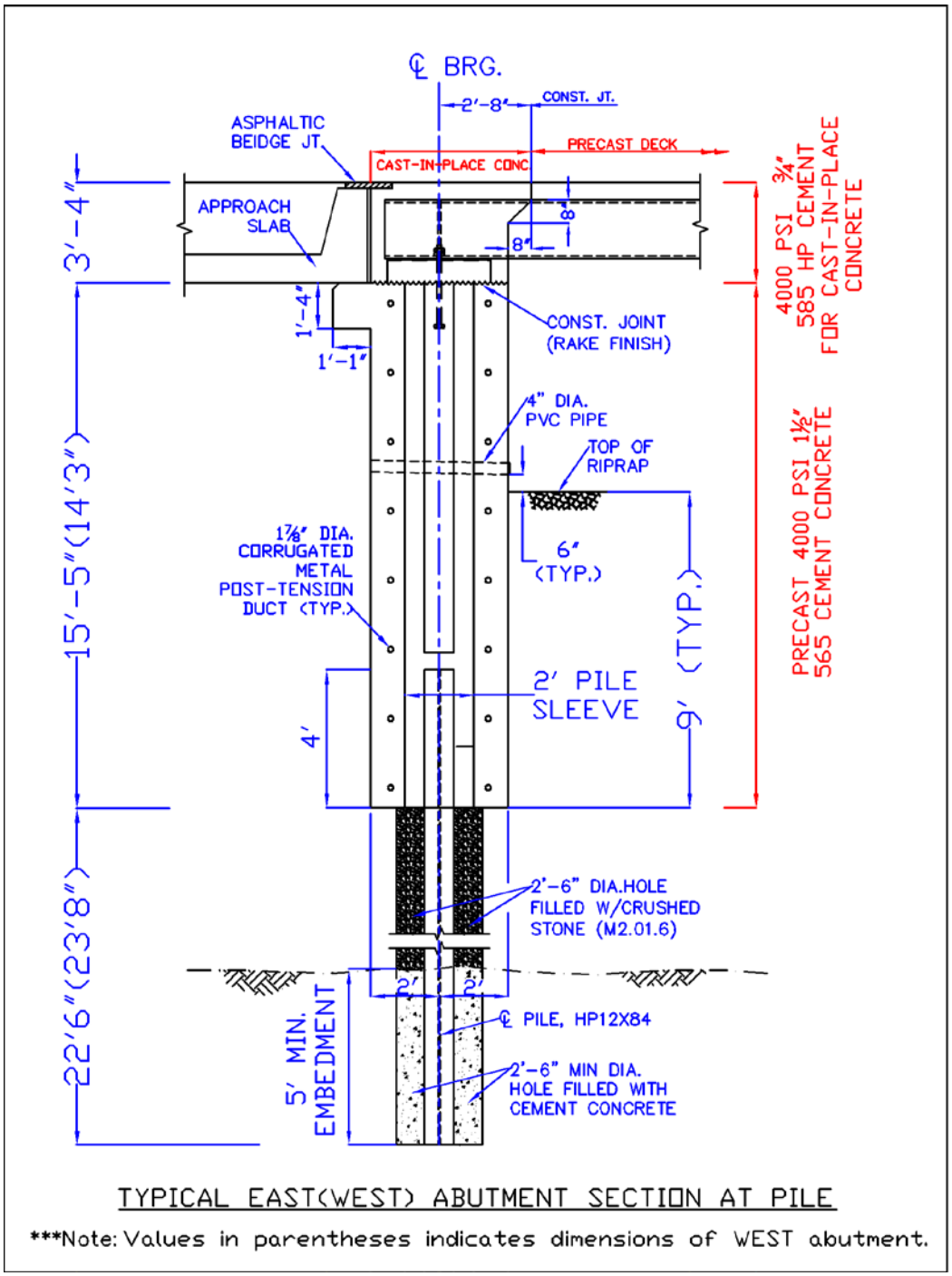

Figure 1-8 Abutment sections (Reproduced by permission of MassDOT)

Table 1-2 Section Properties of bare steel girder FPG

1. Section Properties of FPG		
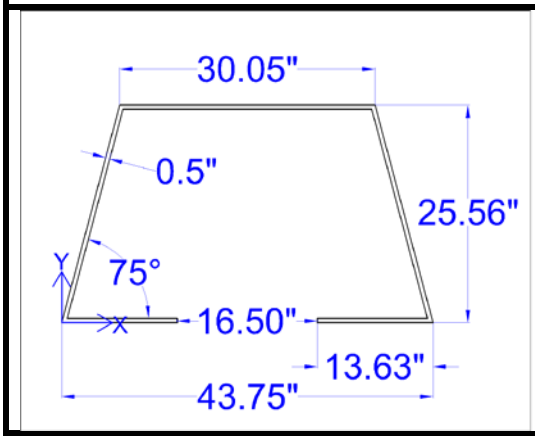	Area [in^2(cm^2)]	54.08 (348.9)
	Centroid [in (cm)] (X,Y-axis @lower left corner)	X: 21.875 (55.6)
		Y: 13.14 (33.4)
	Moments of inertia [in^4 (cm^4)] (@centroid)	I_x: 5771 (240x10^3)
		I_y: 12924 (540x10^3)

Table 1-3 Section Properties when closure pour is not included

2. Section Properties without the presence of Closure Pour		
Transformed Interior Section	Area [in^2(cm^2)]	139.29 (898.6)
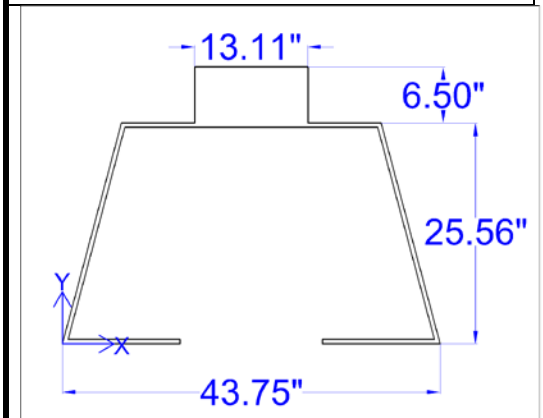	Centroid [in (cm)] (X,Y-axis @lower left corner)	X: 21.875 (55.6)
		Y: 22.73 (57.7)
	Moments of inertia [in^4 (cm^4)] (@centroid)	I_x: 14144 (589x10^3)
		I_y: 14201 (591x10^3)
Transformed Exterior Section	Area [in^2(cm^2)]	143.68 (927.0)
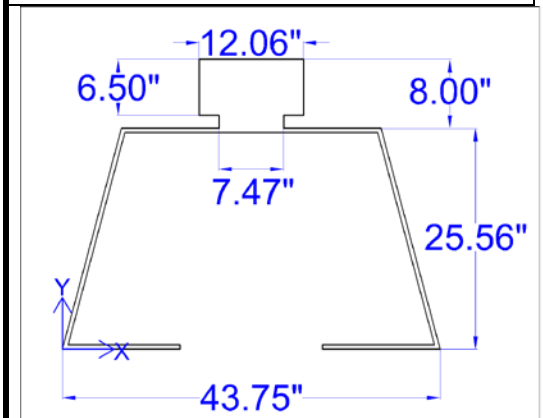	Centroid [in (cm)] (X,Y-axis @lower left corner)	X: 21.875 (55.6)
		Y: 23.54 (60.0)
	Moments of inertia [in^4 (cm^4)] (@centroid)	I_x: 13926 (580x10^3)
		I_y: 15584 (649x10^3)

Table 1-4 Section Properties when closure pour is included

3. Section Properties with the presence of Closure Pour		
Transformed Interior Section 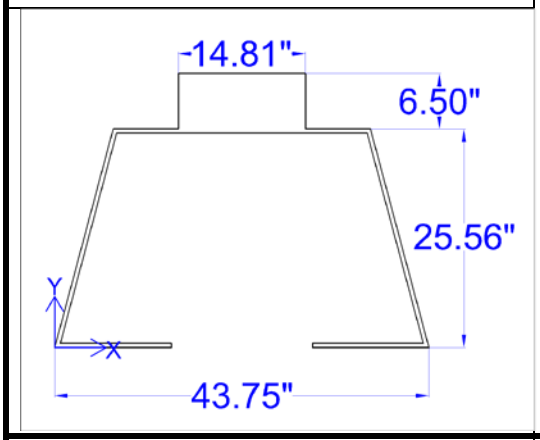	Area [in^2(cm^2)]	150.34 (970.0)
	Centroid [in (cm)] (X,Y-axis @lower left corner)	X: 21.875 (55.6)
		Y: 23.17 (58.9)
	Moments of inertia [in^4 (cm^4)] (@centroid)	I_x: 14619 (608x10^3)
		I_y: 14683 (611x10^3)
Transformed Exterior Section 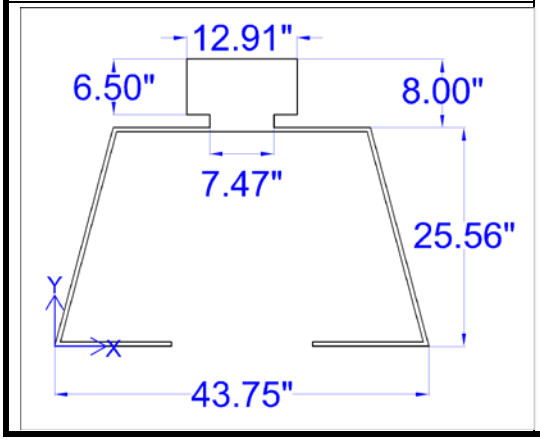	Area [in^2(cm^2)]	149.21 (962.6)
	Centroid [in (cm)] (X,Y-axis @lower left corner)	X: 21.875 (55.6)
		Y: 23.79 (60.4)
	Moments of inertia [in^4 (cm^4)] (@centroid)	I_x: 14141 (589x10^3)
		I_y: 15848 (660x10^3)

1.5 Bridge instrumentation

As part of the construction, the bridge was instrumented with a variety of gauges including embedded concrete strain gauges in the precast slabs and cast-in-place closure pours, arc-weldable strain gauges attached to the folded plate section, tiltmeters, pressure cells, and displacement transducers. The exact locations of the gauges are shown in Figure 1-9 to Figure 1-13. Figure 1-10 shows the locations of instrumented mid-span and quarter-span, and all other gauges in the top view of the

bridge deck. Figure 1-11 shows the elevation view of the instrumented mid-span and quarter-span sections, and more detailed location of strain gauges in the deck and FPG were shown separately in Figure 1-12 and Figure 1-13. Figure 1-9 shows the gauges location on the abutments. Note that in Figure 1-12, the deck thickness was enlarged 10 times in order to show the vertical positions of gauges in the deck.

For analysis ease, longitudinal strain gauges were divided into groups based on the depth of gauges from top of deck, shown in Table 1-5. Due to construction errors, gauges in Detail 1 of Figure 1-10 were incorrectly oriented and do not measure slip of the composite slab as intended, and none of the displacement transducers in Figure 1-10 measure longitudinal displacements, but captured lateral movement of the gravity retaining walls away from the bridge abutment. All girder quarter span gauges were pre-installed at the incorrect side of mid-span prior to galvanizing and were field corrected to be re-welded in their correct locations.

Table 1-5 Gauge division w.r.t. depth from top of deck

Depth from top of deck [in (cm)]		Mid-Span, (1/4 Span)
Deck	3 (7.6)	SG101, 106, 109, 111, 115, 116, 120, 122, (SG112, 121, 125, 126, 129, 130)
	4 (10.2)	SG105, 110, 119, (SG129)
	5 (12.7)	SG102
FPG	6.9 (17.5)	SG147, 152, (SG166)
	8.4 (21.3)	SG142, 159, (SG171)
	19.1 (48.5)	SG148, 151, 153, 156, (SG167, 170)
	20.6 (52.3)	SG144, 146, 160, 163, (SG172, 175)
	31.7 (80.5)	SG149, 150, 154, 155, (SG168, 169)
	33.2 (84.3)	SG143, 145, 161, 162, (SG173, 174)

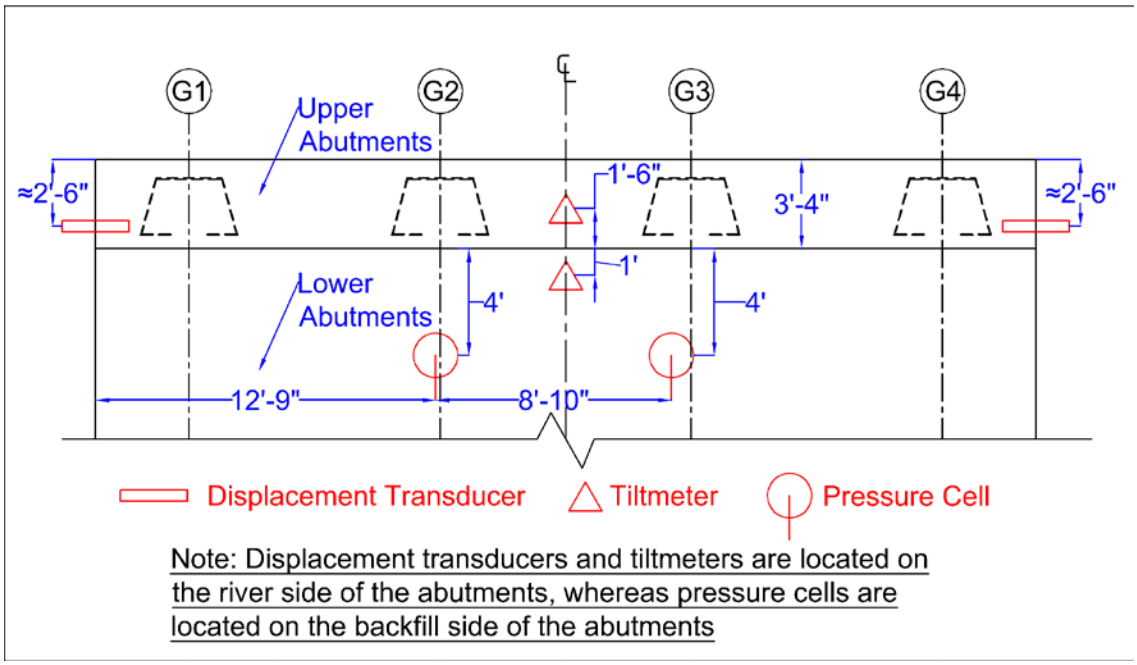

Figure 1-9 Gauges located on abutments (elevation view)

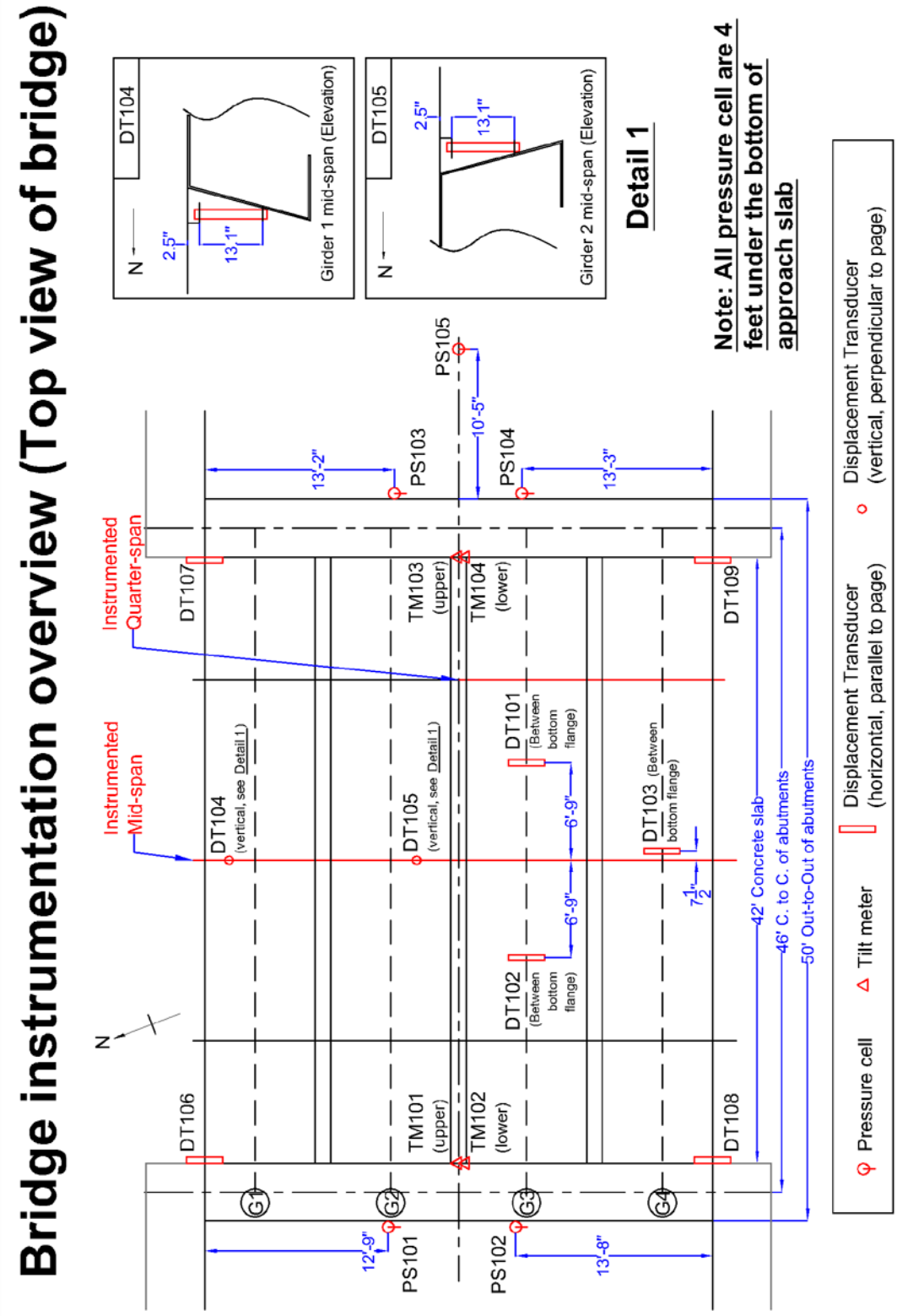

Figure 1-10 Bridge instrumentation overview

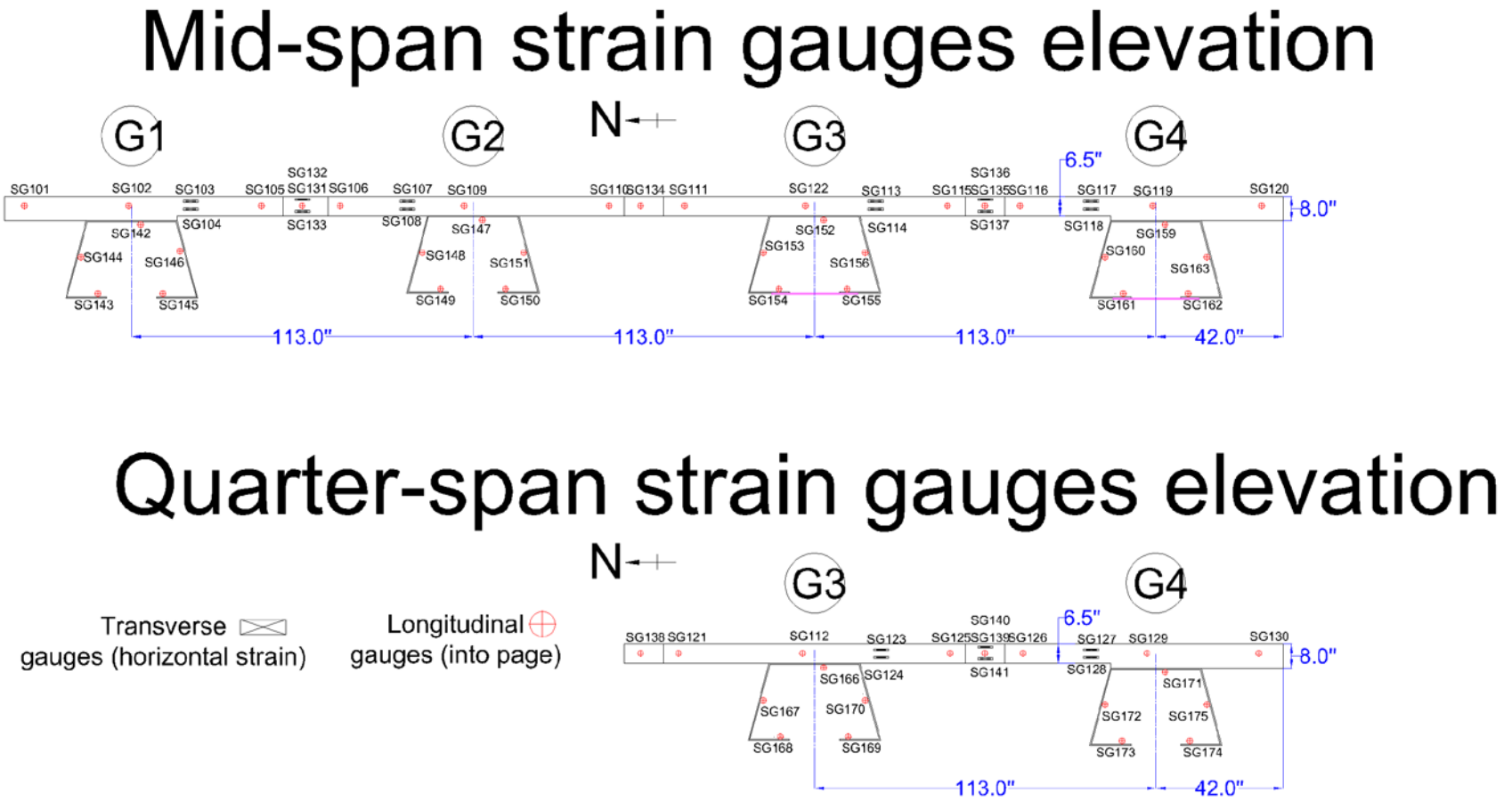

Figure 1-11 Instrumented mid-span and quarter-span sections

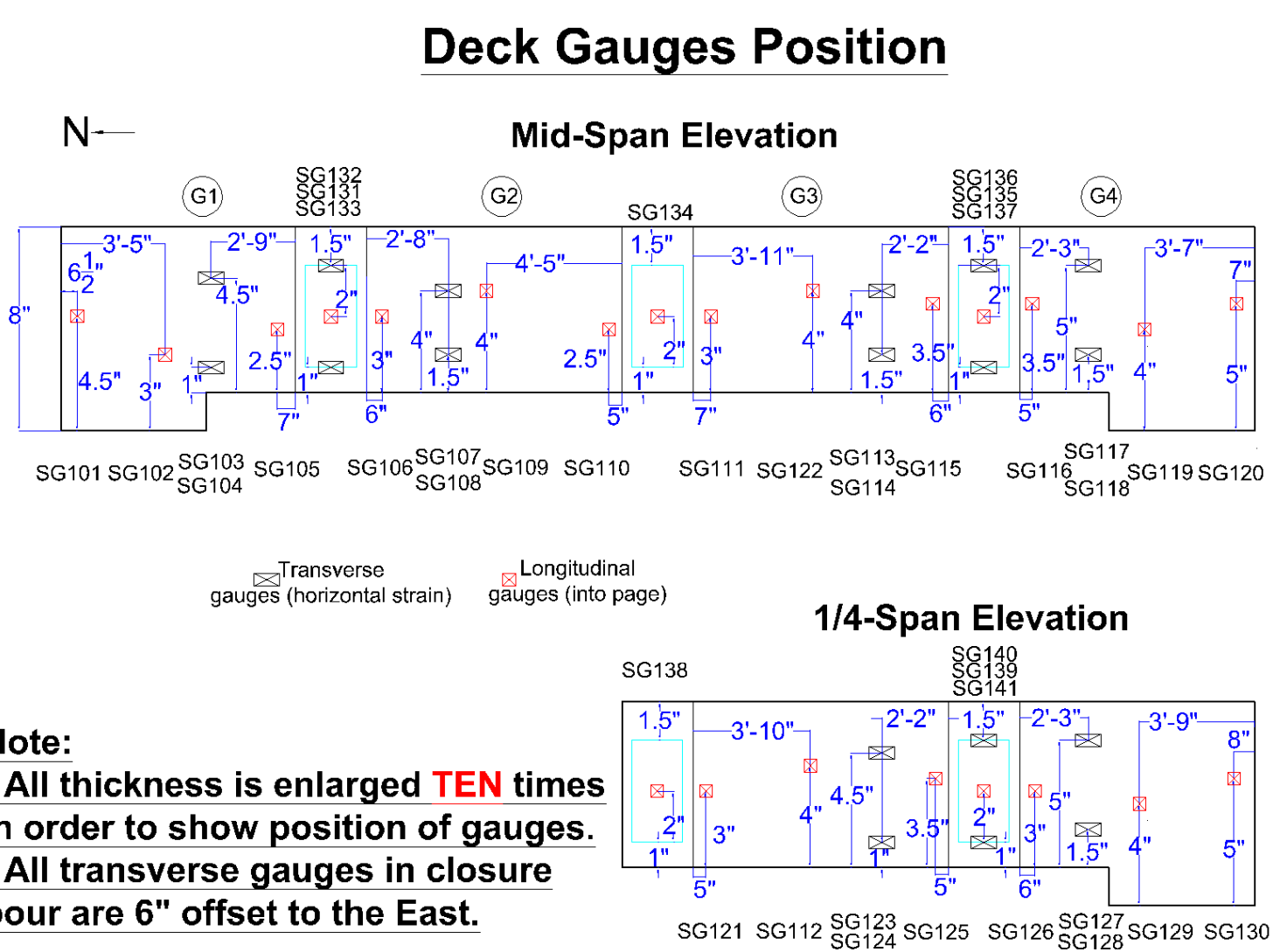

Figure 1-12 Location of deck strain gauges

Note:

- All thickness is enlarged TEN times in order to show position of gauges.

- All transverse gauges in closure pour are 6" offset to the East.

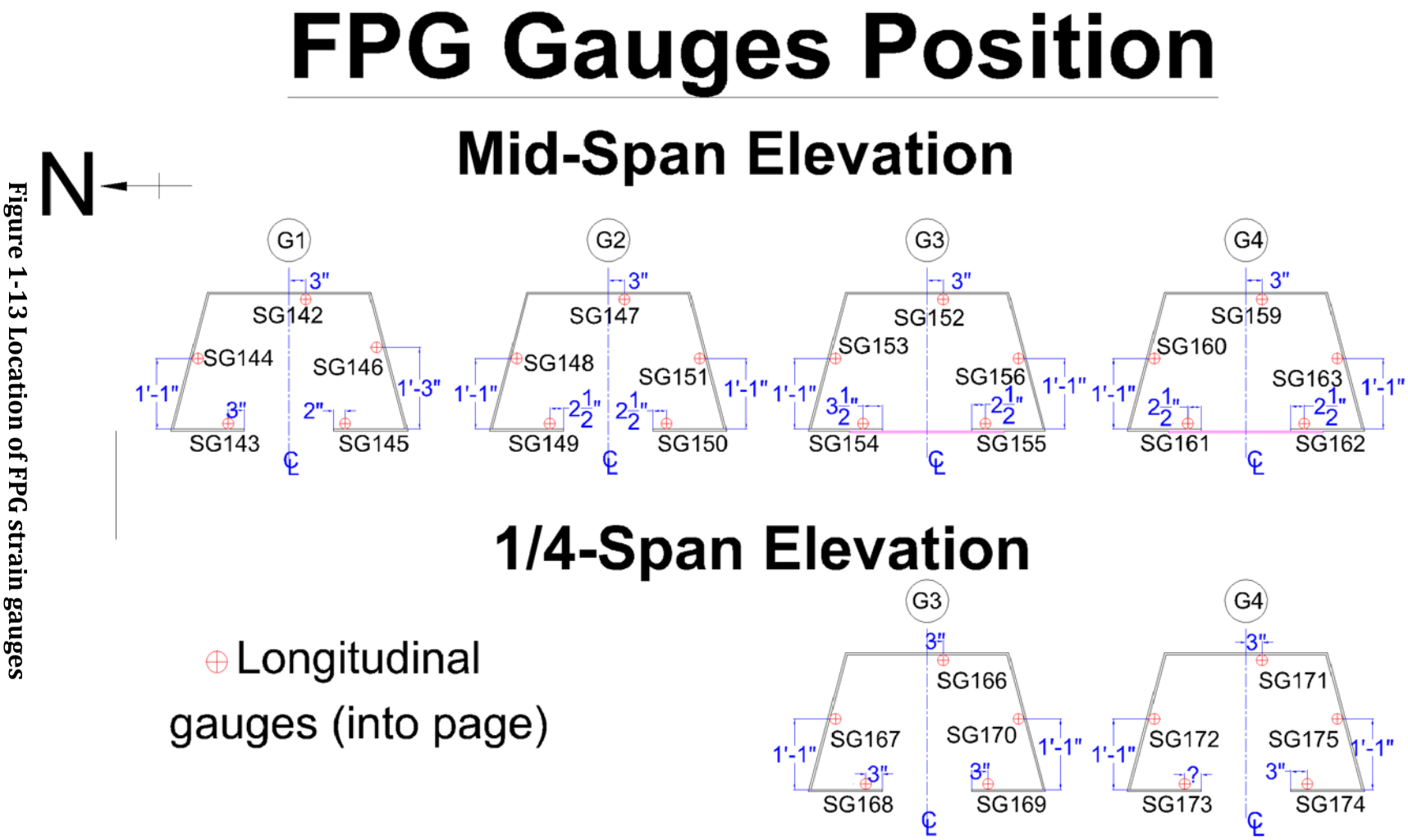

Figure 1-13 Location of FPG strain gauges

CHAPTER 2
FINITE ELEMENT MODELING

2.1 SAP2000 model

A three-dimensional nonlinear FEM was developed to analyze the bridge using SAP2000. The model consists of the full geometry of the bridge: Concrete decks, FPG, integral abutments, piles, and backfill soils pressure. Concrete decks and abutments were modeled using 4-node shell elements with 6 Degree of Freedom (DOF) (3 translational and 3 rotational) at each node, FPG and piles were modeled using 2-node three dimensional frame elements with 6 DOF at each node. Concrete deck shell elements were modeled at the mid-plane of the slab, and the thickness of the shell elements were then offset to the correct location using the joint offset command. To simulate the composite behavior of the bridge superstructures, the FPG frame elements have shared nodes with the concrete deck shell element, and the insert points of the frame elements were set to be top center and were offset to the actual location to the bottom of the concrete deck, see Figure 2-1. It was assumed that there was no slip at the slab to girder interface under the service loads analyzed as part of this research. The abutment shell elements were also connected to the concrete deck shell elements and the FPG frame elements using shared nodes at the intersections of the mid-plane of the decks and the mid-plane of the abutments, see Figure 2-3. Also, rigid links were applied on the abutment and the deck shell elements to model the clear-span support condition by the abutments. The HP12x24 pile frame elements were modeled under the abutments and were assumed to have a pinned support at their base, see Figure 2-2.

The summary of the model is presented in Table 2-2**.** Joint numbers corresponding to deck gauges position is shown in Table 2-3. Insert point conditions of FPGs are shown in Figure 2-1**.** Isometric views of the model are shown in Figure 2-2. Meshing of deck and abutments are shown in Figure 2-3. The material properties of the model are same as mentioned in Section 1.4.1, and values are shown in Table 2-1.

Table 2-1 Material properties of the SAP2000 model

Material	Modulus of Elasticity [ksi (MPa)]	Unit weight [Pcf (kN/m^3)]	Yield Strength [ksi (MPa)]	Tangent modulus [ksi (MPa)]
Steel	29000 (200x10^3)	490 (77.0)	50 (344.7)	210.3 (1450)
Concrete	3800 (26.2x10^3)	150 (23.6)	none	none

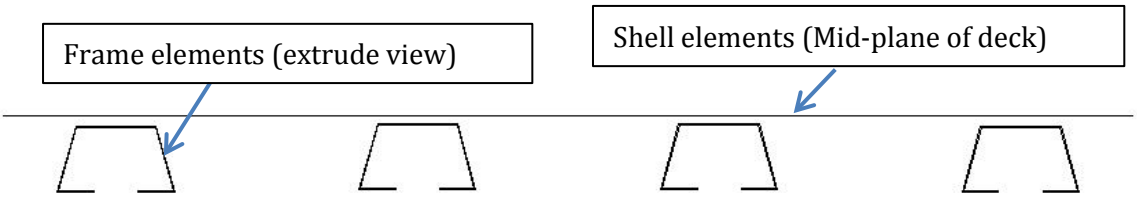

Figure 2-1 Insert point of FPG girders in SAP2000 in extrude view

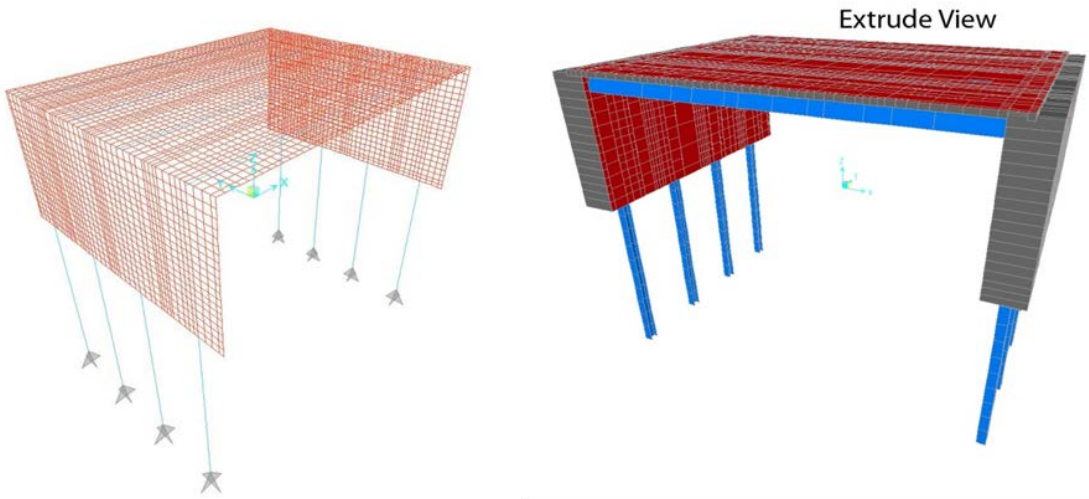

Figure 2-2 Isometric views of bridge model in SAP2000

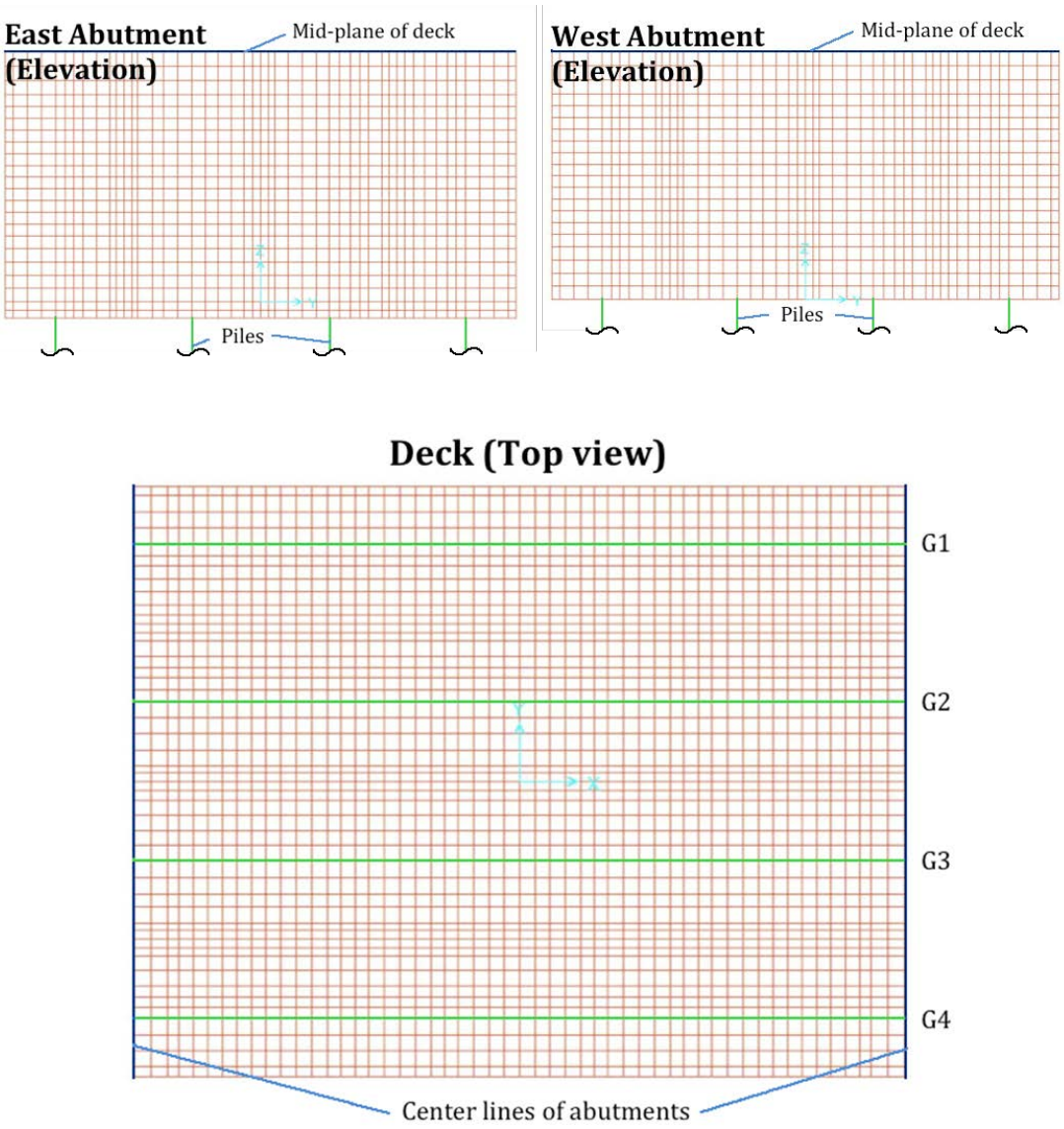

Figure 2-3 Meshing of East, West abutment, and deck after auto-meshing in SAP2000

Table 2-2 Summary of SAP2000 FEM

ELEMENT	FPG		Continuous frame element with specified FPG properties, A992 Gr50 steel
	Deck	Exterior	8 inch [20.3 cm] thick shell-thin element.
		Interior	6.5 inch [16.5 cm] thick shell-thin element.
	Abutment		4 feet [122 cm] thick shell-thin element.
	Pile		Continuous frame element with HP12x84 section, A992 Gr50 steel.
GEOMETRY	FPG		4 girders evenly spaced at 113 inch [287 cm] from north to south with Insert point = top center, offset: Ext. = -4 inch [10.2 cm]; Int. = -3.25 inch [8.3 cm].
	Deck	Exterior	Between centerlines of abutments in E-W direction and 57 in wide from edge on both sides in N-S direction
		Interior	Between centerlines of abutments in E-W direction and between exterior deck in N-S direction
	Abutment	East	Centered at deck edges, 17.1 feet [521 cm] deep from mid-plane of deck.
		West	Centered at deck edges, 16 feet [488 cm] deep from mid-plane of deck.
	Pile	East	Orientated with flanges parallel to longitudinal direction of bridge, 22.5 feet [686 cm] deep from bottom of abutment
		West	Orientated with flanges parallel to longitudinal direction of bridge, 23.6 feet [719 cm] deep from bottom of abutment.
MESHING	FPG		Manually meshed with respected to truck wheel load position, mid-span and quarter-span, and auto-meshed with any intersections with other element.
	Deck		Manually meshed with respected to truck wheel load position, gauges locations, closure pours and FPG girders, and auto-meshed into maximum size of 1 ft^2 [929 cm^2]
	Abutment		Meshed with respected to deck mesh points, and auto-meshed into maximum size of 1 ft^2 [929 cm^2]
	Pile		Manually meshed into 1 foot [30.5 cm]long frame elements

Table 2-3 Joint number corresponding to deck gauges positions

Location	Mid-Span		Quarter-Span	
	Gauge number(Direction)	Joint number (coordinate)	Gauge number(Direction)	Joint number (coordinate)
G4	SG120(L)	705 (0,-204.5)	SG130(L)	721 (138,-204.5)
	SG119(L)	593 (0,-169.5)	SG129(L)	597 (138,-169.5)
	SG117(T),118(T)	896 (0,-146.5)	SG127(T),128(T)	984 (138,-146.5)
	SG116(L)	897 (0,-124.5)	SG126(L)	985 (138,-124.5)
CP	SG136(T),135(L),137(T)	899 (0,-113)	SG140(T),139(L),141(T)	987 (138,-113)
G3	SG115(L)	901 (0,-101.5)	SG125(L)	989 (138,-101.5)
	SG113(T),114(T)	903 (0,-80.5)	SG123(T),124(T)	991 (138,-80.5)
	SG122(L)	578 (0,-56.5)	SG112(L)	582 (138,-56.5)
	SG111(L)	904 (0,-13.5)	SG121(L)	992 (138,-13.5)
CP	SG134(L)	906 (0,0)	SG138(L)	994 (138,0)
G2	SG110(L)	908 (0,11.5)		
	SG109(L)	563 (0,56.5)		
	SG107(T),108(T)	911 (0,74.5)		
	SG106(L)	913 (0,100.5)		
CP	SG132(T),131(L),133(T)	915 (0,113)		
G1	SG105(L)	917 (0,126.5)		
	SG103(T),104(T)	640 (0,154.5)		
	SG102(L)	549 (0,169.5)		
	SG101(L)	642 (0,205)		

*Note: L=longitudinal direction, T=transverse direction.

2.1.1 **SAP2000 Model Testing**

The verification of the model was performed first by verifying the reactions at supports due to self-weight, and then verified again with an addition 100 kips [445kN] concentrated joint force applied in positive y direction at the lower right corner of top of the deck, the load is shown in Figure 2-4**.** Calculations of the bridge self-weight are provided in Table 2-4**.** SAP2000 results for the reactions at supports due to self-weight of bridge only and the reactions at supports due to self-weight and addition 100 kips [445 kN], are shown in Table 2-5.The results show that, in both cases, the reactions at support balanced loads in x, y, and z directions, therefore verifying that this is a working model.

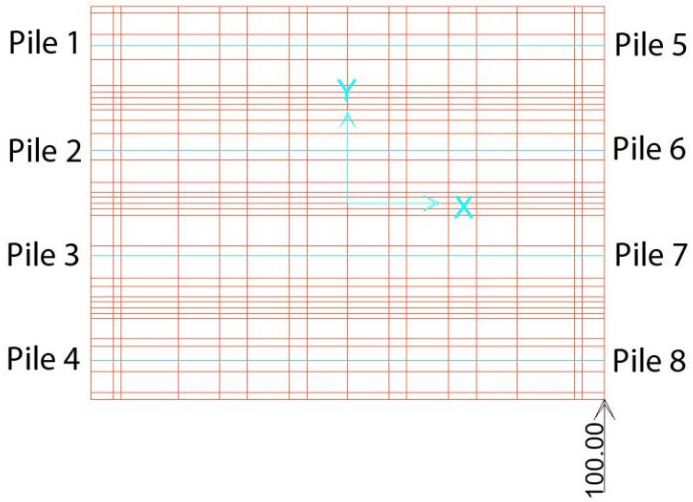

Figure 2-4 Plan view of 100k concentrate joint force applied at the lower right corner of top of the deck

Table 2-4 Hand calculations of self-weight of SAP2000 bridge model

Element	Dimension [in]	Volume [ft³]	Unit weight [Pcf]	Weight {kip]
2 Exterior decks	2(8x57x552)	291.33	150	43.70
Interior deck	6.5x309x552	641.60	150	96.24
West abutment	48x423x206.3	2424.3	150	363.64
East abutment	48x423x220.2	2587.8	150	388.18
4 FPGs	4(A=40.75,L=552)	52.07	490	25.51
4 West Piles	4(A=24.6,L=284.4)	16.195	490	7.94
4 East Piles	4(A=24.6,L=270.48)	15.40	490	7.55
→The self-weight of bridge = 932.76 kips				

Table 2-5 Reactions at supports due to self-weight only and self-weight plus 100k

Location	Reactions due to self-weight [kip]			Reactions due to self-weight and 100k [kip]		
	R_y	R_x	R_z	R_y	R_x	R_z
Pile1	-5.588e-3	0.52	113.39	-1.31	4.19	121.77
Pile2	-4.042e-4	0.52	113.73	-1.34	1.74	116.48
Pile3	2.191e-3	0.52	113.81	-1.43	-0.7	111.08
Pile4	3.693e-3	0.52	113.37	-1.34	-3.15	104.98
Pile5	5.486e-3	-0.52	119.38	-23.57	-4.79	-3.14
Pile6	1.154e-3	-0.52	119.88	-24.83	-1.94	80.60
Pile7	8.631e-4	-0.52	119.78	-23.40	0.9	159.50
Pile8	-7.395e-3	-0.52	119.42	-22.78	3.75	241.49
∑	-1e-7	0	932.76	-100	0	932.76

2.2 ANSYS APDL model 1 – shear lag model

A three-dimensional FEM was created using ANSYS APDL at the later phase of this thesis to capture the shear lag effect on the girders. As only stress concentration and shear lag effect within the girder sections is of interest, the model consists only of the superstructure of the bridge. The abutments were not modeled in this analysis and assumed to provide a fixed end condition at the ends of the superstructure, which matched field data results for these loads. Therefore fixed end boundary condition is modeled on the superstructure. The concrete deck was modeled using 8-node solid 185 element in ANSYS with 3 translational DOF at each

node, whereas the FPG steel girder and the bottom flange tie-plate were modeled using 4-node shell 181 element in ANSYS with six DOF (3 translational and 3 rotational) at each node. Composite action between the concrete deck solid elements and the FPG shell elements is provided by meshing them with coincident nodes at their interface, bottom flange tie-plate shell elements were also connected to the FPG shell elements using coincident joints. The isometric view of the model is shown in Figure 2-5 and the section view is shown in Figure 2-6 and Figure 2-7. Note that although the concrete deck was modeled using solid elements instead of shell elements and resulted in creating additional elements (by a factor of two), the analysis was within linear range of all material and required less than ten minutes to run, and therefore this model was used for further analysis as it generated more specific results.

The superstructure was modeled with girder length equal to the girder clear span (inside face dimensions of abutments) as initial assumptions of girder length defined by the center of the abutment resulted in higher girder stresses than reported in the field data. The full section of the bridge was modeled and is therefore the stress distribution within the section can be obtained during analysis. Live load test truck wheel loads are modeled as area load at each tire location instead of concentrated load in order to obtain more exact results. The area loads were applied on the faces of the nearest four elements which surrounding the nearest node where the truck wheel axle is located. The area of the faces is about one square foot with dimension of about 12 in [30.5 cm] by 11.4 in [29.0 cm]. Figure 2-8 shows the area loading in ANSYS for one of the test positions.

Material properties used in this ANSYS model are the same as mentioned in Section 1.4.1, except the units are different in the ANSYS models. The material properties of the bridge in ANSYS units are shown in Table 2-6.

Table 2-6 Material properties of the bridge used in the ANSYS model

Material	Modulus of Elasticity [psi (MPa)]	Mass Density [slinch/in^3 (kg/m^3)]	Poison's Ratio	Yield Strength [psi (MPa)]	Tangent modulus [psi (MPa)]
Steel	$29x10^6$ ($200x10^3$)	$0.735x10^{-3}$ ($7.85x10^3$)	0.3	$50x10^3$ (344.7)	$210.3x10^3$ (1450)
Concrete	$3.8x10^6$ ($26.2x10^3$)	$0.225x10^{-3}$ ($2.41x10^3$)	0.18	none	none

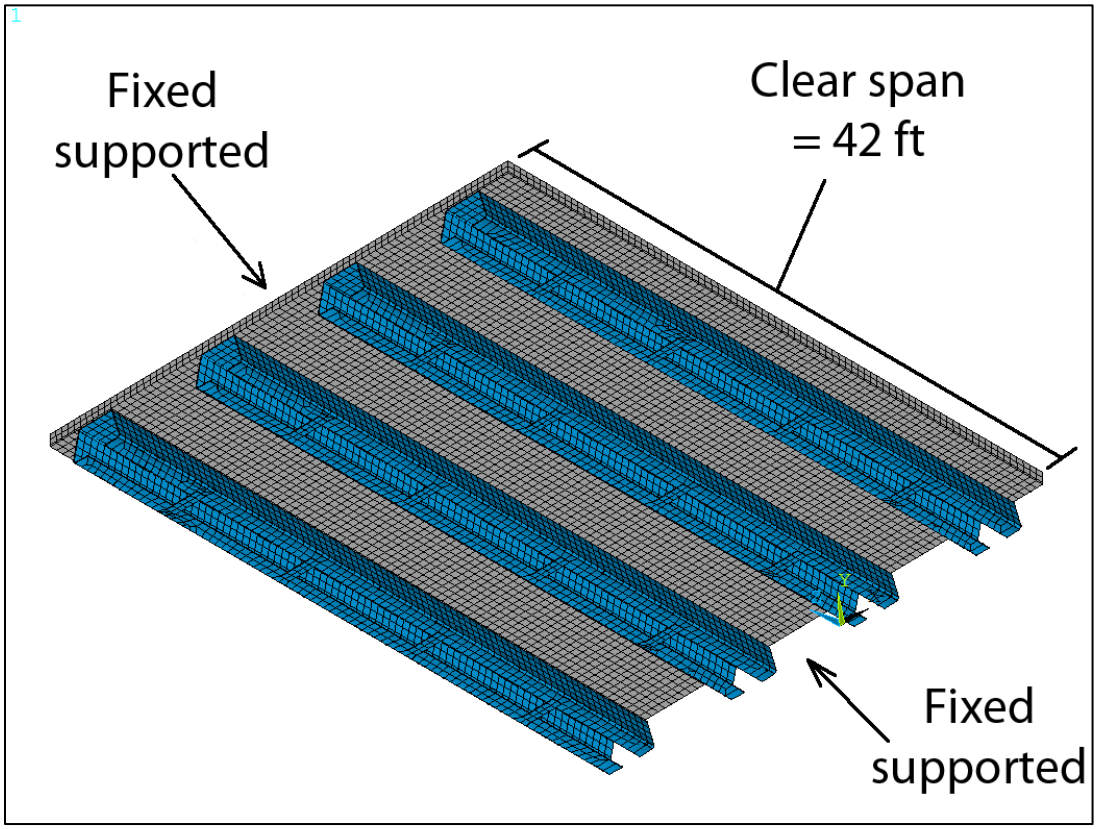

Figure 2-5 Isometric view of ANSYS model 1

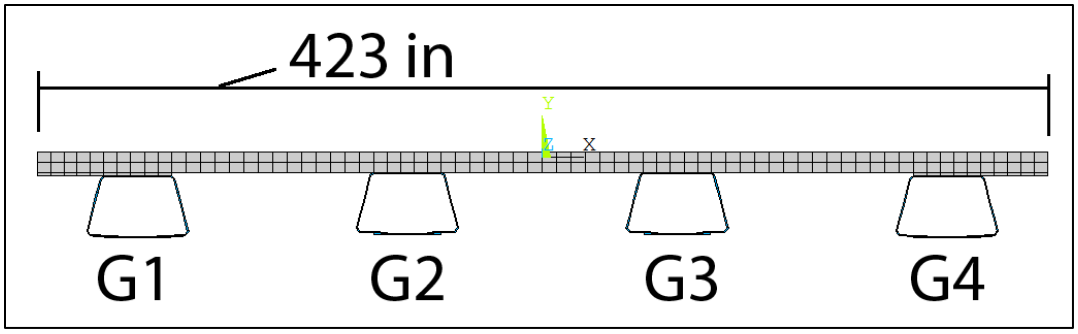

Figure 2-6 Section view of ANSYS model 1

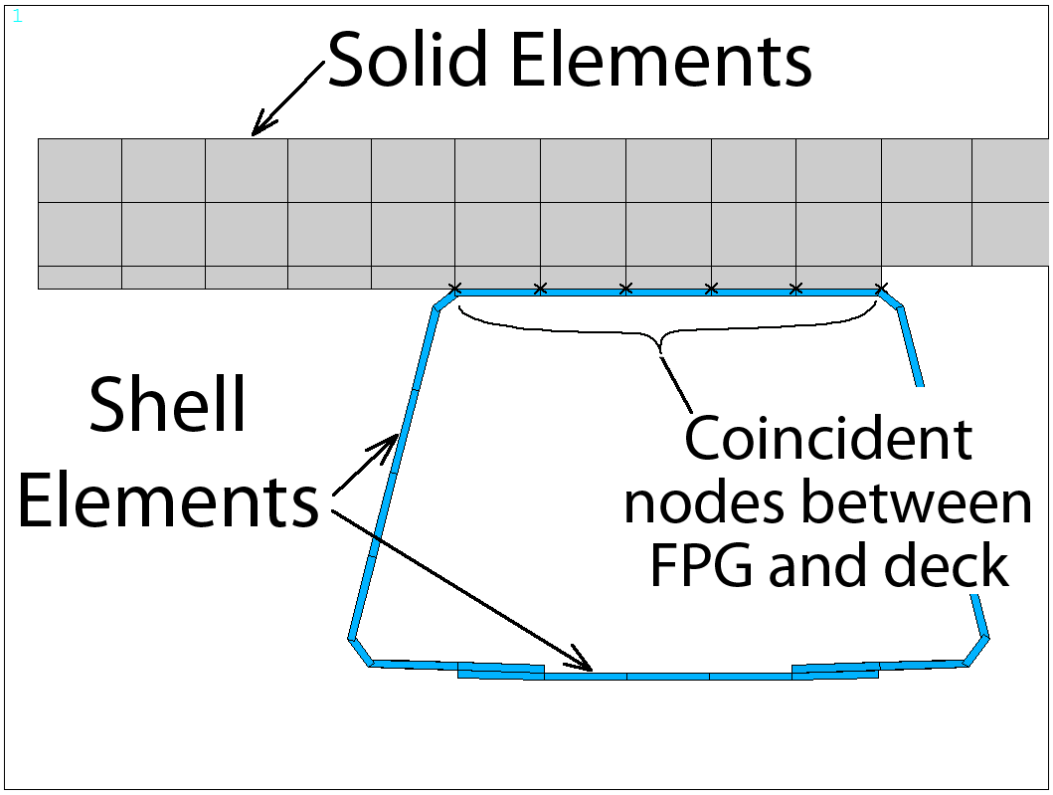

Figure 2-7 Close-up exterior section view of ANSYS model 1

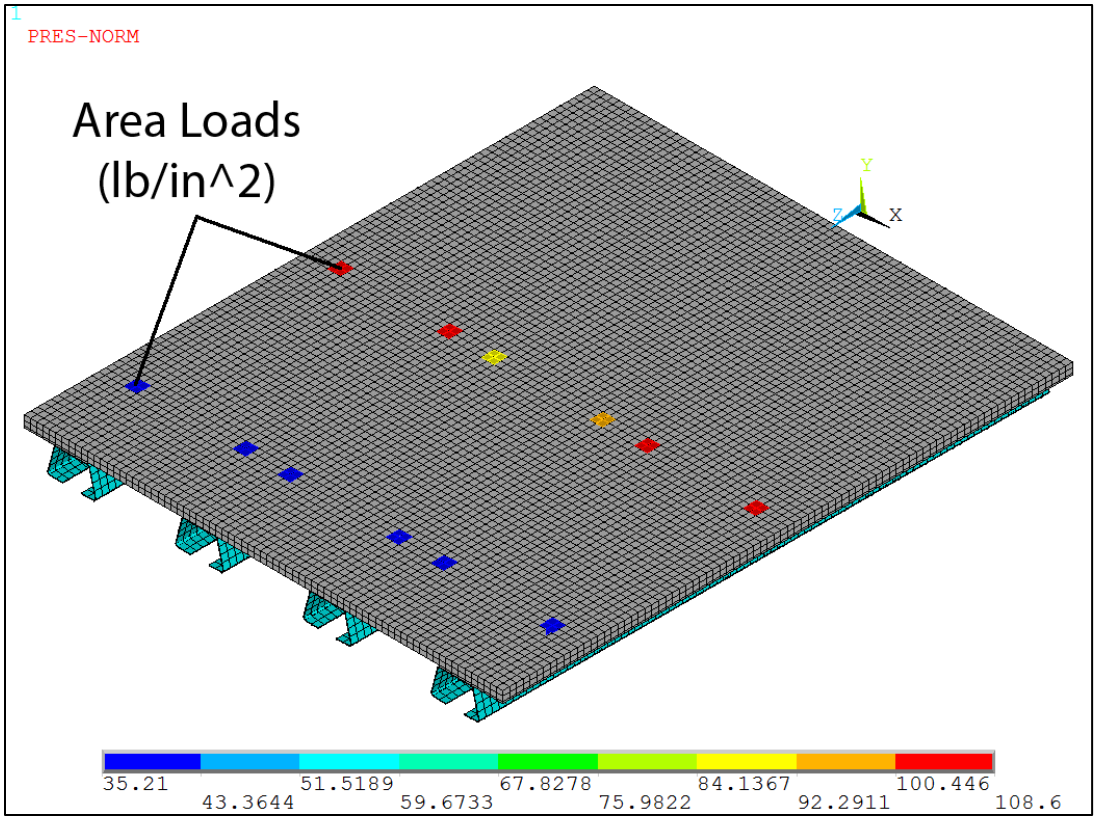

Figure 2-8 Loading condition of Position 4 in ANSYS model 1

2.3 ANSYS APDL model 2 – thermal behavior model

In order to study the behavior of the bridge under thermal loading, a FEM of the entire bridge geometry was created using ANSYS APDL. The model was created based on the shear lag model 1 that was used in the static live load test stage. In this model, however, the substructure was included: the integral abutments, the piles, and the soil pressure at the backfill and around the piles were considered. The superstructure portion of the model is same as the shear-lag model, with the deck modeled as solid elements and the FPG modeled as shell elements. The abutments were modeled using 4-node shell elements (3 translational and 3 rotational DOF at each node) with half-of the upper abutments that provide continuity to the

superstructure modeled using 8-node solid elements (3 translational DOF at each node), or the entire abutments were modeled using 8-node solid elements for runs where thermal gradient within the abutment was considered. The piles were modeled using 2-node beam elements (3 translational and 3 rotational DOF at each node). The soil springs were model using 2-node unidirectional nonlinear spring elements with force deformation curve defined for each spring; see Section 2.4 for the calculation of the spring force deformation curves. The continuity between different components were provided using coincident nodes with the exception of the backfill soil spring connected to the abutments using 2-node rigid beam elements (3 translation and 3 rotational DOF at each node). The pile support conditions were modeled to be fixed at location on the piles about 1 foot into the rock level. The geometry of the model with abutments modeled using shell elements is shown in Figure 2-9 and Figure 2-10, whereas the geometry of the model with abutments modeled using solid elements is shown in Figure 2-11. Figure 2-12 shows sample thermal gradient applied on the models.

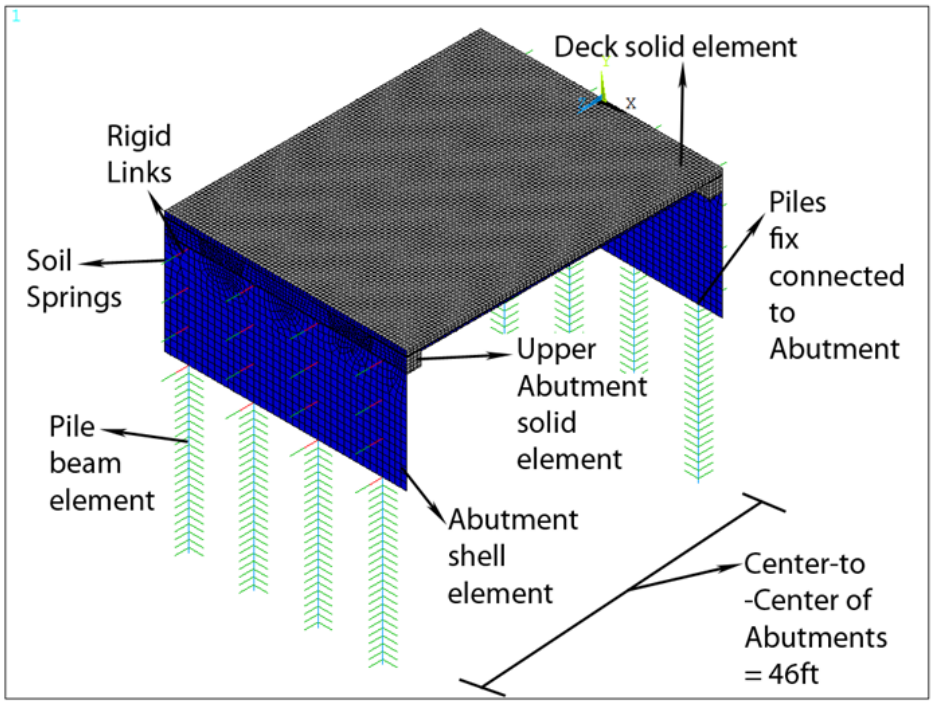

Figure 2-9 Isometric view of ANSYS model 2 with lower abutments modeled with shell elements

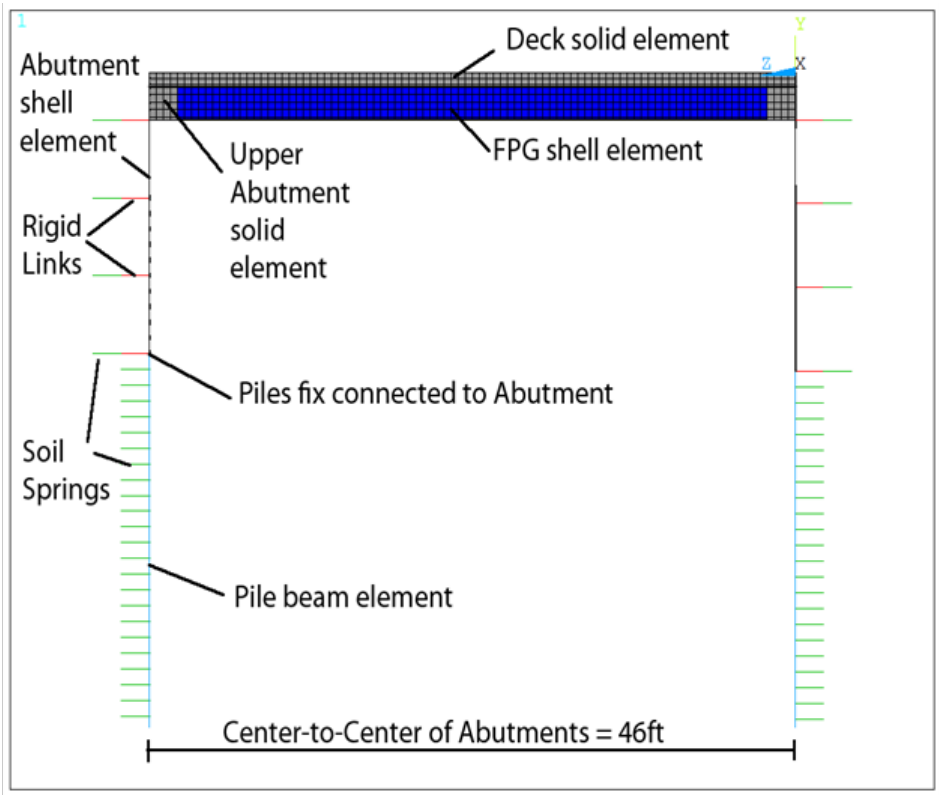

Figure 2-10 Side view of ANSYS model 2 with lower abutments modeled with shell elements

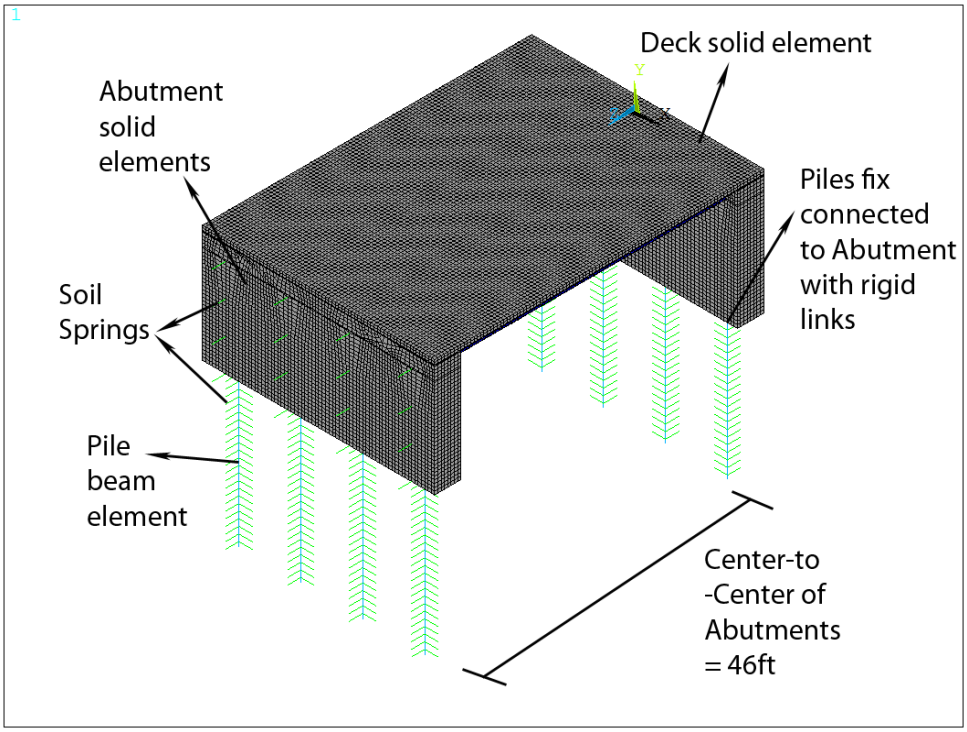

Figure 2-11 Isometric view of ANSYS model 2 with abutments modeled with solid elements

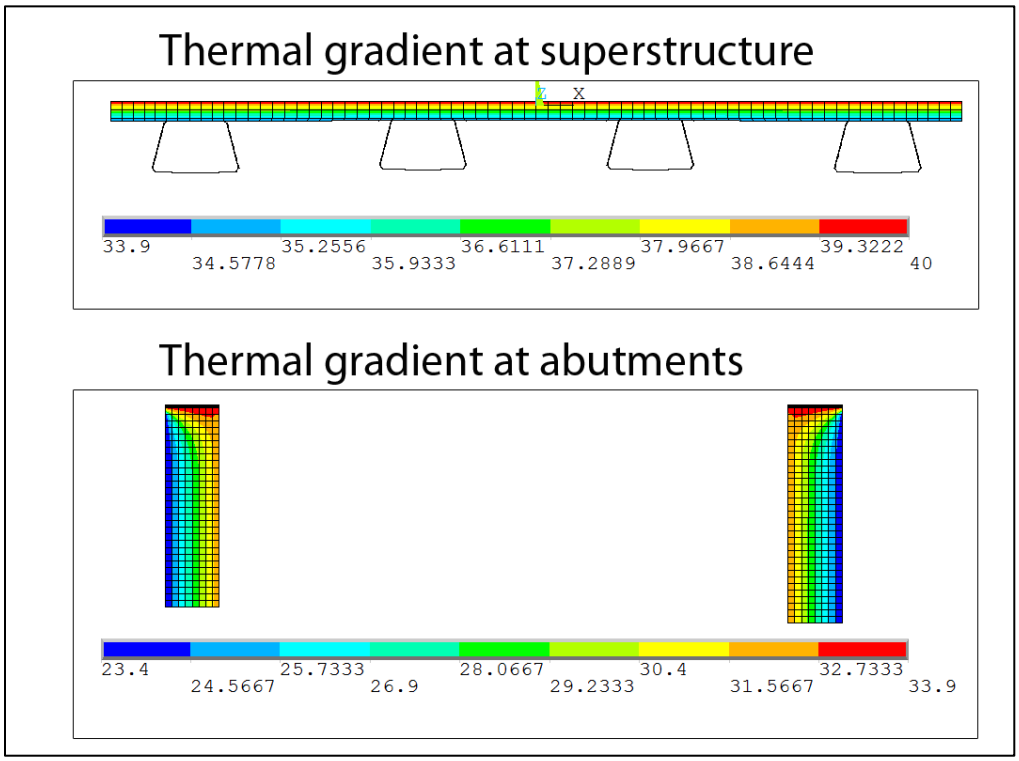

Figure 2-12 Sample thermal gradient at the superstructure and the abutments

2.4 Soil properties and modeling

The methodology used in determining soil properties and modeling the soil behavior for IABs was based on techniques used in Kalayci (2010). Discrete nonlinear Winkler springs were used to model the soil behind the abutments and along the length of the piles.

Backfill soil and *in situ* soil around the abutments and piles were modeled with nonlinear springs defined by a force-deformation curve for each defined soil layer on the abutment and every foot down the piles. The approach for modeling the soil nonlinearity was identical to studies by other researchers[9,10,11]. Springs representing backfill soil pressure on the abutments were defined by calculating effective horizontal earth pressures acting over the corresponding tributary areas using Eq-1. Coefficients of lateral earth pressure were calculated according to Barker et al[12].

$$F = K \times \sigma'_V \times w \times h \qquad \text{(Eq-1)}$$

Where F = effective lateral soil resistance on the defined object with dimensions of w by h, K = lateral earth pressure coefficient[12], σ'_V = effective vertical earth pressure, and w = width and h = height of tributary area.

Springs represent the *in situ* soil resistances acting around the piles are modeled using nonlinear Winkler springs attached every foot on along the depth of the piles in both orthogonal directions. Force-deformation curves for these springs were defined using the hyperbolic tangent method described by API[13], Eq-2. The ultimate lateral soil resistance was calculated according to Bogard and Matlock[14].

Medium dense sand soil properties were chosen to be used based on field geotechnical report and experiences in monitoring of IABs. The values of these properties are chosen based on Kalayci 2010[9] and Civjan, Bonczar, Brena, DeJong, and Crovo 2007[10], values are listed in Table 2-7.

$$F = A \times p_u \times \tanh\left(\frac{k_1 z y}{A p_u}\right) \times L \quad \text{(Eq-2)}$$

Where A = an empirical correction factor (A = 3-0.8(z/D) ≥ 0.9), D = the pile diameter, p_u = the estimated ultimate lateral soil resistance (p_{us} or p_{ud}), k_1 = soil strength modulus, z = the soil depth from the top of the soil layer to the specified node, y = the deflection along horizontal axis, and L = the length of pile section.

Table 2-7 Soil Properties used in FEM

Location	Soil Type	Location of Ground Water Table	Soil weight [Pcf (kN/m^3)]	Lateral Subgrade Constant [Pci (kN/m^3)]	Internal Friction Angle (degrees)
Abutment	Mid-Dense Sand	Below	120 (18.9)	60 (16.3x10^3)	35
Pile	Mid-Dense Sand	Above	57.6 (9.0)	60 (16.3x10^3)	35

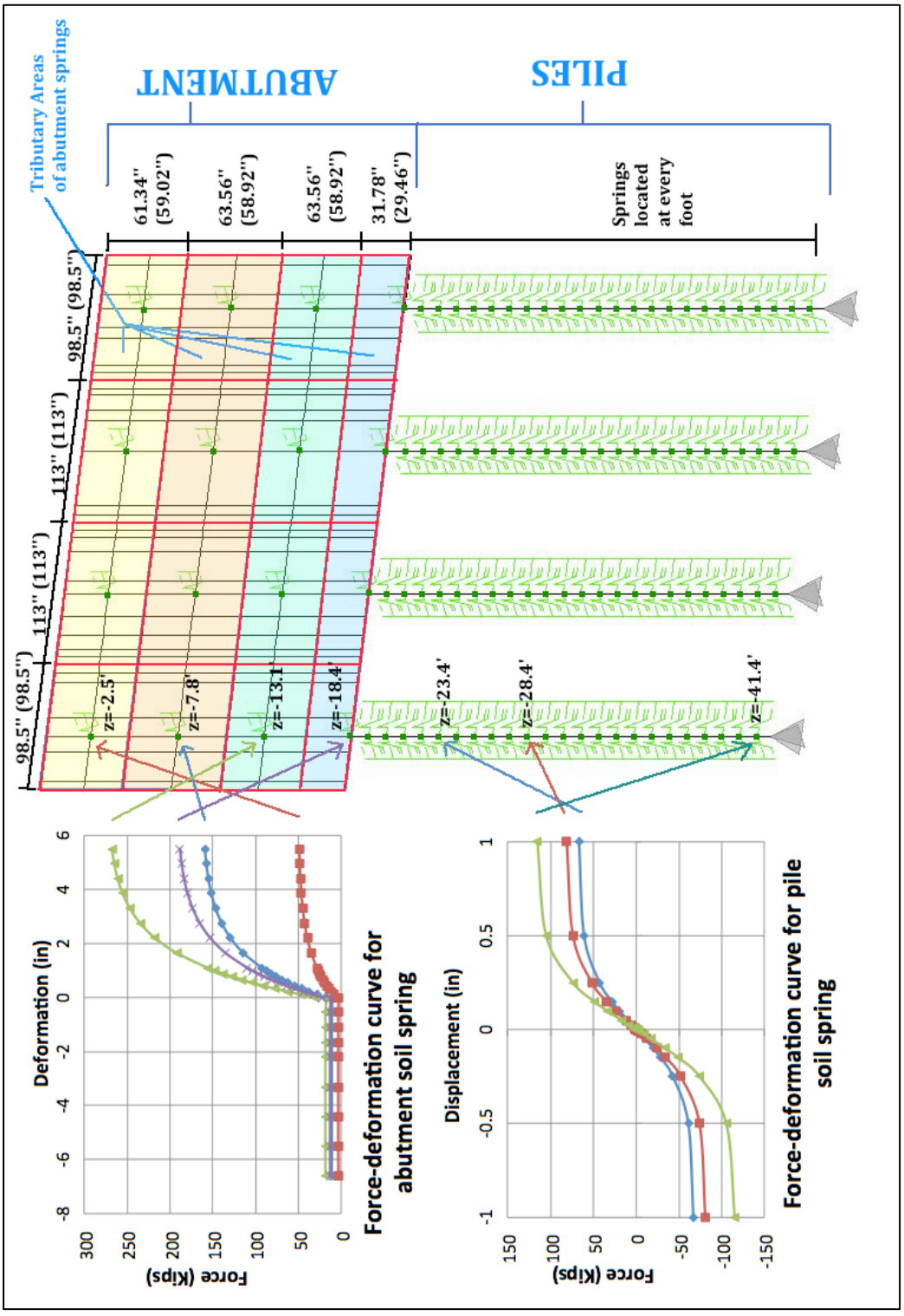

Figure 2-13 East (West) abutment and pile soil springs elevation

CHAPTER 3
CONSTRUCTION AND SELF-WEIGHT EFFECT

This section describes the deformations on the bridge during the construction phase. Maximum readings which recorded during fabrication and construction are shown, and hand calculation on the induced strain in the girder due to self-weight is performed.

3.1 Construction data

Readings were taken from the instruments installed on the bridge during various construction stages. Not all instruments were installed at these stages. Readings were taken by both UMass and GeoTek employees at different times. The stages of construction that were documented for this steel FPG integral abutment bridge are curing of the precast concrete slabs at the precast yard, and the concrete closure and end diaphragm pours in the field. Reading times and corresponding construction activities are shown in Table 3-1.

3.2 Maximum effects during bridge construction

The maximum effects during the bridge construction are listed in Table 3-2. All values are referenced to the time that the gauge was installed during construction. It is important to note that the precast concrete deck strain gauges were installed at the prefabricator's plant, while the steel strain gauges were installed after setting of the girders and therefore only include a small portion of dead load on the structure (closure pours, railings, etc.) and displacement

transducers were installed near the end of construction. Therefore steel girder results should only be used to verify calculations for similar load conditions, while concrete strains are complete.

Table 3-1 Construction Reading Descriptions

UMASS READING DESCRIPTIONS			
Reading	Date	Time	Description
0a	8/10/2011	11:30	Girder 1 Gauge zero readings.
1a	8/10/2011	13:50	Girder 1 Gauge readings with wet concrete in forms.
2	9/11/2011	17:00	All girders with supports blocks at bearing stiffeners in precast yard.
3a	10/7/2011	10:00	All girders on delivery trucks on site. Support blocks at bearing stiffeners.
4	10/7/2011	13:15	All girders placed on abutments, pin-pin support condition.
5	10/17/2011	10:35	All girders placed on abutments with catwalks installed underneath girders, pin-pin support condition.
7	10/25/2011	8:30	Readings prior to concrete closure and end diaphragm
8	10/25/2011	Afternoon	Readings after to concrete closure and end diaphragm
GEOTEK READING DESCRIPTIONS			
Reading	Date	Time	Description
0	8/10/2011	-	Reading Installed - Girder 1
	8/12/2011	-	Reading Installed - Girder 2
	8/23/2011	-	Reading Installed - Girder 3 and Girder 4
1	8/12/2011	-	Reading after precast concrete pour - Girder 1
	8/23/2011	-	Reading after precast concrete pour - Girder 2
	8/23/2011	-	Reading after precast concrete pour - Girder 4 (2 hours after
3	10/7/2011	-	Reading upon girder delivery
6	10/24/2011	-	Reading before end diaphragm and deck pour
9	11/3/2011	-	Reading after end diaphragm and deck pour

Table 3-2 Construction Maximum Effects

Gauge Type	Tension	Compression
Deck Embedded Concrete Strain [με] (longitudinal)	29.4 (SG105)	-178.0 (SG111)
Deck Embedded Concrete Strain [με] (transverse)	27.7 (SG103)	-209.6 (SG104)
Closure Pour Embedded Concrete Strain [με] (longitudinal)	105.7 (SG139)	-144.3 (SG138)
Closure Pour Embedded Concrete Strain [με] (transverse)	107.3 (SG136)	-184.0 (SG132)
Bottom flange of Steel FPG Strain Gauge [με] **Note: Self-weight effect not captured	69.7 (SG155)	-139.0 (SG168)
Disp. Transducer [in] (between girder bottom flanges)	5.01E-02 (DT101)	-4.38E-03 (DT101)
Disp. Transducer [in] (vert. between slab and FPG)	3.10E-03 (DT104)	-1.55E-03 (DT105)

3.3 Induced strain in deck due to girder self-weight

Since there is no detailed information about the support conditions of the precast composite girder when they are placed in the precast yard and during transportation to the construction site, it is not possible to obtain the effect due to self-weight from the field data. However, the theoretical induced strain due to the effect of self-weight was calculated for this stage to show a reference value. During construction, the girders were placed on bearing plates on top of abutments with a pin-pin supported condition without concrete closure pour and diaphragm pour, and the length of the precast concrete deck is 40.67 foot while the length of FPG steel girder between supports is 46 foot. The theoretical induced strain was calculated based on the above condition and section properties without the presence of closure pour from Table 1-3 are used. Self-weight of girder is calculated by using unit weight of 150 pcf [23.6 kN/m^3] for concrete and 490 pcf [77.0 kN/m^3] for steel. Moment values at mid-span and quarter-span were first calculated and were then transformed into strain values using equation: $= \frac{My}{EI}$, where M = moment, y = vertical distance from centroid, I = Ix =Area moment of inertia of transformed section, and E = modulus of elasticity of steel= 29x10^3 ksi [200x10^3 MPa], the load condition and moment diagram is shown in Figure 3-1. Calculation results for extreme top and bottom longitudinal fiber strain in exterior and interior section at mid-span are shown in Table 3-3.

The result in Table 3-3 shows that the concrete deck top fiber strain is less than the maximum construction effect shown in Table 3-2 as expected, and

therefore based on the values in Table 3-2 it is likely that no cracking was formed in the concrete deck before load test. On the other hand, since the self-weight effect was not captured in the steel FPG gauges, when considering the maximum effect at the bottom of FPG in later stage in this thesis, the sum of the values in Table 3-2 and Table 3-3 should be used.

Table 3-3 Theoretical longitudinal strain induced at mid-span due to self-weight

Exterior section (G1 and G4)		Interior section (G2 and G3)	
Weight of concrete [kip/ft]	0.712	Weight of concrete [kip/ft]	0.677
Weight of steel [kip/ft]	0.184	Weight of steel [kip/ft]	0.184
Moment@mid-span [k-ft]	234.4288	Moment@mid-span [k-ft]	225.297
Strain at top of deck [με]	-69.81	Strain at top of deck [με]	-61.51
Strain at bottom of FPG [με]	163.97	Strain at bottom of FPG [με]	149.82

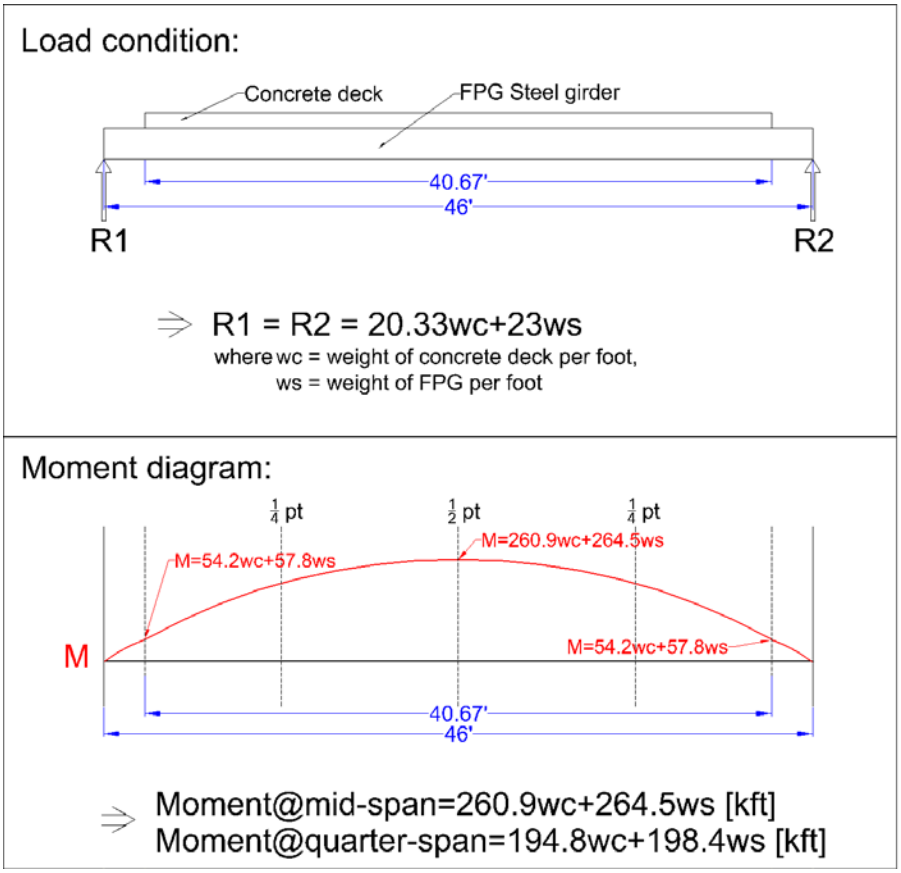

Figure 3-1 Load condition and moment diagram under self-weight of girder

CHAPTER 4
LIVE LOAD TESTING

After completion of construction, a live load test was performed on 11/21/2011 using loaded dump trucks of known weight in various positions on the bridge. The maximum recorded readings of the live load test are summarized in Table 4-1. Note that it was found in Section 5.1 that the readings of the FPG gauges do not represent the maximum effect in the FPG due to their locations. The loading condition for each live position (LL Pos #) is shown in Figure 4-2 and Figure 4-3. All readings of the live load test are referenced to the bridge condition at the start of load testing where no trucks were situated on the bridge and all gauge's readings were corrected for thermal offsets through a linear regression from readings obtained immediately post and prior to testing.

Table 4-1 Live Load Test Maximum Effects

Gauge Type	Gauge	LL Pos #	Max. reading
Embedded Concrete Strain (longitudinal)	SG-111	10	-10.4 με
	SG-106	12	12.4 με
Embedded Concrete Strain (transverse)	SG-104	11	-12.8 με
	SG-114	13	13.7 με
Closure Pour Embedded Concrete Strain (longitudinal)	SG-138	11	-14.3 με
Closure Pour Embedded Concrete Strain (transverse)	SG-133	6	16.0 με
Steel Strain Gauge (mid-height web of girder)	SG-144	5	51.6 με
Disp. Transducer (between girder bottom flanges)	DT-103	4	6.69E-03 in.
Disp. Transducer (vert. between slab and FPG)	DT-105	11	-3.62E-03 in.
Tiltmeter (abutments)	TM-001	2	3.56E-03degree

- Steel Girder Modulus of Elasticity = 29 x 10^3 ksi

4.1 Load test theoretical 2D moment calculation:

Theoretical gross moments induced in mid-span and quarter-span during the truck live load tests are calculated by assuming the bridge acts as a single two

dimensional beam and the abutments provide fixed end condition at clear span (42ft) for the bridge. Pinned end conditions were also considered, but preliminary calculations verified that the integral abutments provide a condition near fixity. In each live load test position, the total effect of multiple truck axle loads was obtained by superposition of individual truckload and the effects of individual truck axle load were calculated as following:

As in Figure 4-1, individual truck axle load is represented as P, far end reaction is represented as R, and the distances of the load from two ends of the bridge are represented as a and b where a is less than b, then moment at distance x from far end (M_x) is calculated as follow, and calculation and results are shown in Table 4-2 and Table 4-3.

For x < b: $M_x = R \cdot x - \frac{Pba^2}{l^2}$,

For x > b: $M_x = \frac{Pb^2}{l^3} \cdot (3a + b) \cdot (l - x) - \frac{Pab^2}{l^2}$,

where $R = \frac{Pa^2}{l^3} \cdot (a + 3b);\ l = a + b, (a < b)$.

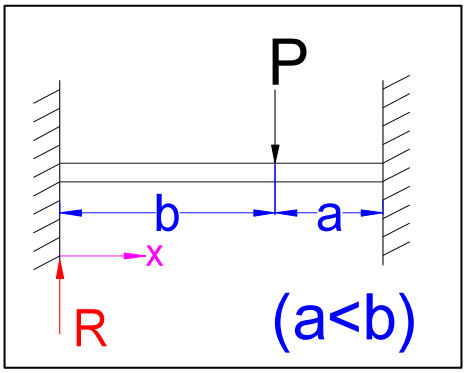

Figure 4-1 Single load acting on fixed end beam

In Table 4-2 and Table 4-3, each load test has multiple truck axle loads P and therefore has multiple P positions. For instance, P1 represents the first truck axle load, a1 and b1 represent the location of the load P1, R1 represents the far end reaction induced by P1, and M_{P1} represents the moment induced at distance x from

far end by P1, where x is 21ft for moment at mid-span but varies for that of quarter-span. Final the total moments (Mt) induced in each load test were obtain by superimposing the moments induced by individual truck axle load. The values of far end reaction and moment are shaded in green.

Table 4-2 Concentrated load P position and far end reaction R

Load test	a1 [ft]	b1 [ft]	P1 [k]	R1 [k]	a2 [ft]	b2 [ft]	P2 [k]	R2 [k]	a3 [ft]	b3 [ft]	P3 [k]	R3 [k]
1	5.8	36.2	31.8	1.7	21.0	21.0	83.1	41.5	0.0	0.0	0	0.0
2	17.3	24.7	31.8	11.8	10.5	31.5	83.1	13.0	0.0	0.0	0	0.0
3	10.5	31.5	83.1	13.0	17.3	24.7	31.8	11.8	0.0	0.0	0	0.0
4	21.0	21.0	83.1	41.5	5.8	36.2	31.8	1.7	0.0	0.0	0	0.0
5	5.8	36.2	10.9	0.6	21.0	21.0	25.2	12.6	12.0	30.0	10.9	2.2
6	5.8	36.2	10.9	0.6	21.0	21.0	25.2	12.6	12.0	30.0	10.9	2.2
7	5.8	36.2	10.9	0.6	21.0	21.0	25.2	12.6	12.0	30.0	10.9	2.2
8	5.8	36.2	10.9	0.6	21.0	21.0	25.2	12.6	12.0	30.0	10.9	2.2
9	0.6	41.4	10.9	0.0	15.8	26.3	25.2	8.0	15.8	26.3	10.9	3.4
10	17.3	24.7	21.8	8.1	10.5	31.5	54.2	8.5	0.0	0.0	0	0.0
11	5.8	36.2	21.8	1.1	21.0	21.0	54.2	27.1	0.0	0.0	0	0.0
12	5.8	36.2	10.9	0.6	21.0	21.0	29.1	14.5	0.0	0.0	0	0.0
13	5.8	36.2	10.9	0.6	21.0	21.0	25.2	12.6	0.0	0.0	0	0.0

Table 4-3 Calculated moment in mid-span and ¼-span

Load test Position	**Mid-Span** (x=21ft)				**Quarter-span Span**						
	M_{P1} [kin]	M_{P2} [kin]	M_{P3} [kin]	**Mt [kin]**	x1 [ft]	x2 [ft]	x3 [ft]	M_{P1} [kin]	M_{P2} [kin]	M_{P3} [kin]	**Mt [kin]**
1	154	5232	0	5386	31.5	10.5	0	364	0	0	364
2	1363	1308	0	2671	31.5	10.5	0	241	-327	0	-86
3	1308	1363	0	2671	31.5	10.5	0	2943	-119	0	2824
4	5232	154	0	5386	31.5	10.5	0	0	-56	0	-56
5	53	1584	224	1862	31.5	10.5	10.5	125	0	-48	77
6	53	1584	224	1862	31.5	10.5	10.5	125	0	-48	77
7	53	1584	224	1862	31.5	10.5	10.5	125	0	-48	77
8	53	1584	224	1862	31.5	10.5	10.5	125	0	-48	77
9	1	891	386	1279	31.5	31.5	10.5	1	309	-48	262
10	936	854	0	1789	31.5	10.5	0	165	-213	0	-48
11	106	3415	0	3521	31.5	10.5	0	250	0	0	250
12	53	1830	0	1883	31.5	10.5	0	125	0	0	125
13	53	1584	0	1637	31.5	10.5	0	125	0	0	125

*Note: Red color indicate that x > b.

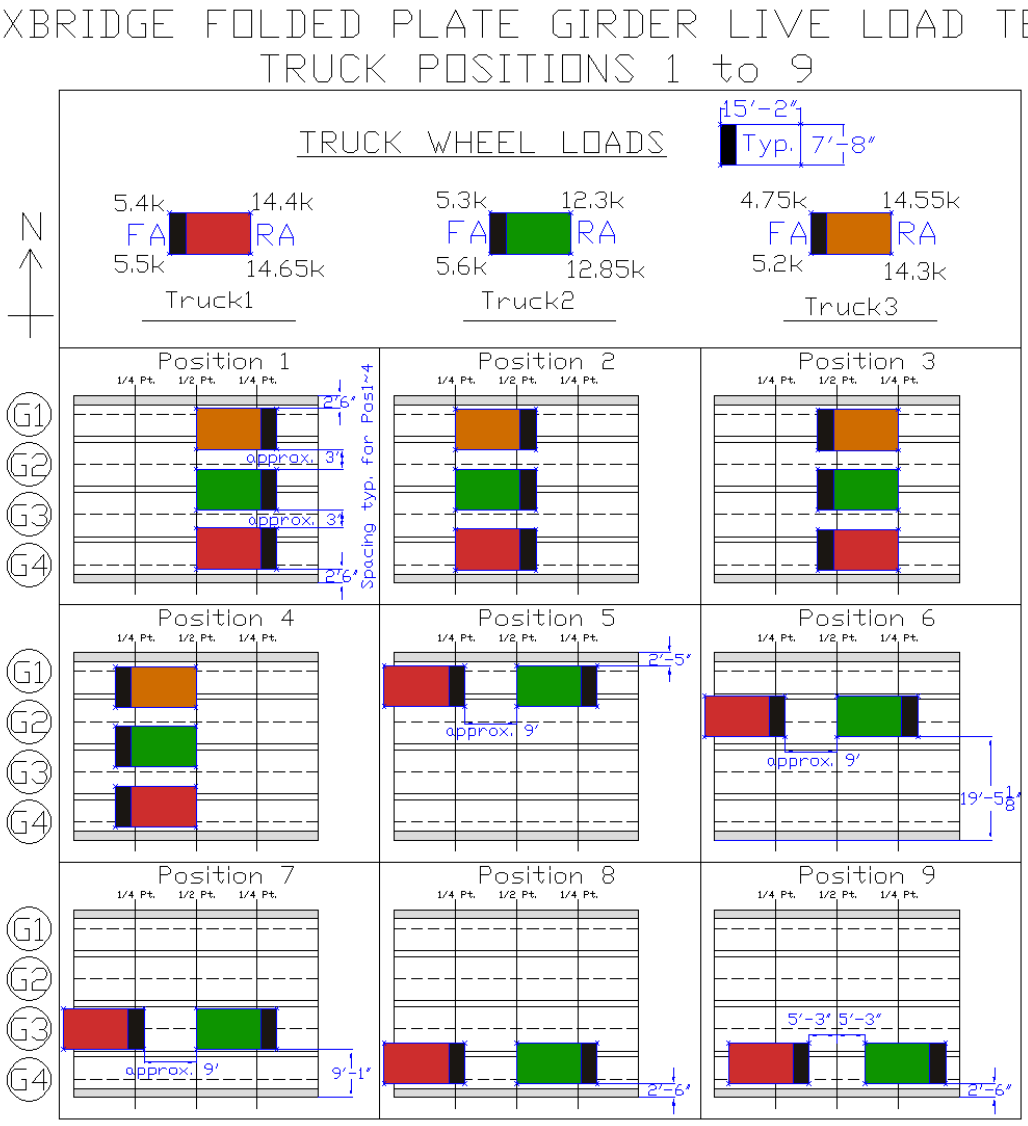

Figure 4-2 Live load test Positions 1 to 9

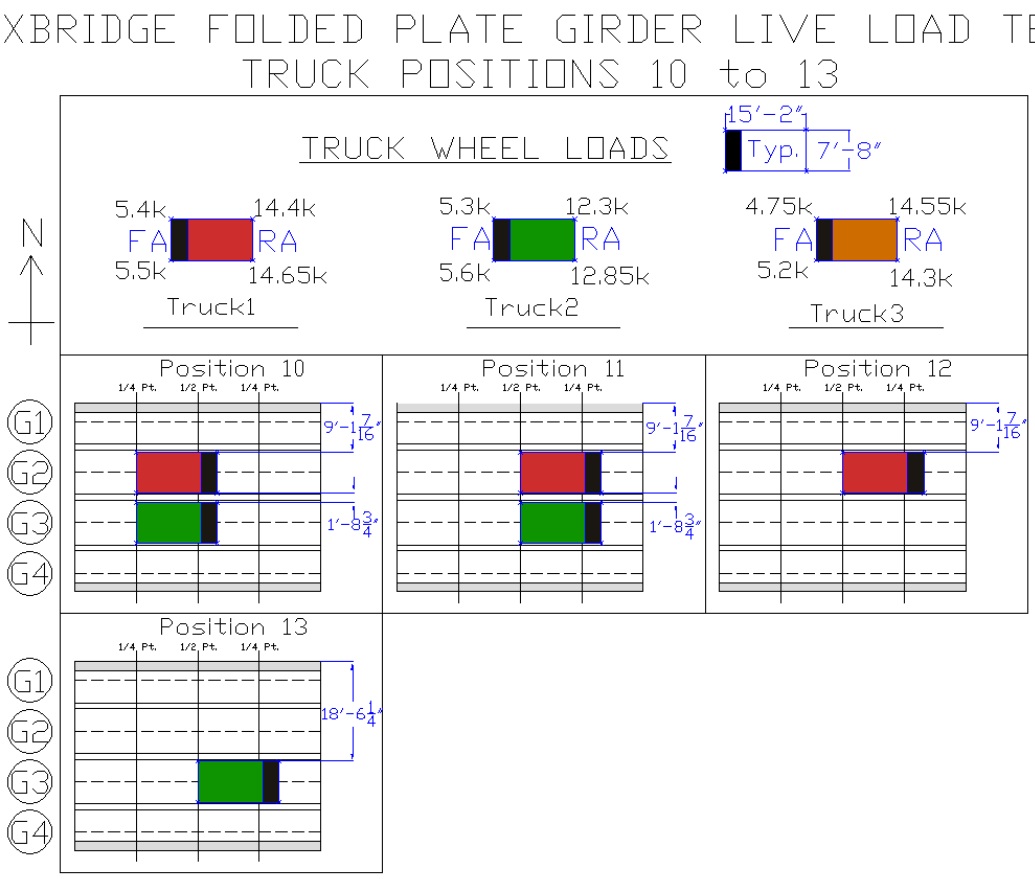

Figure 4-3 Live load test Positions 10 to 13

4.2 Effect of change in temperature during load test

During load test, ambient temperature on site increased due to solar radiation and resulted in expansion of the bridge. This global response affected gauge readings individually. Therefore, temperature correction of gauge reading is required. Based on the difference of gauge readings before and after load test, where there is no truck placed on the bridge, and by assuming the temperature fluctuation is linear within the testing period, the thermal induced strain is calculated for each gauge in every load test position. Each gauge reading is corrected by subtracting the thermal induced strain for each different load test position.

4.3 Theoretical induced strain in deck and FPG due to load test:

Theoretical induced strains in the deck and FPG due to live load testing were calculated in this section based on the theoretical moment values obtained in Section 4.1, see Table 4-3 for moment values. The calculations are similar to the procedure in Section 3.3 where moment values are transformed into strain values using equation: $\boldsymbol{\varepsilon} = \frac{\boldsymbol{My}}{\boldsymbol{EI_g}}$, and M = moment, y = vertical distance from centroid and the location of centroid is 9.33 in [23.7 cm] from the top of concrete deck (which is the average theoretical centroid location of exterior and interior sections), I_g = transformed gross area moment of inertia of the bridge section = 57521 in^4 [2394x10^3 cm^4], and E = modulus of elasticity of steel = 29x10^3 ksi [200x10^3 MPa]. In order to compare the actual gauge readings with the calculated theoretical values, longitudinal strain gauges are divided into groups based on the depth of gauges from the top of concrete deck, as shown in Table 1-5. Concrete deck longitudinal gauges locations are shown in Figure 1-12, whereas FPG gauges locations are shown in Figure 1-13. For each group, the average gauge readings were used to represent the group when compared to the calculated 2D strain. Table 4-4 and Table 4-5 show the results of calculation and comparison between theoretical 2D hand-calculated values and the actual gauges readings in mid-span and quarter-span respectively.

Table 4-4 Induced strain in deck and FPG due to Load test at mid-span

Note:	ε_T = Theoretical 2D induced strain with respect to depth [με] ε_G = Average longitudinal gauge reading with respect to depth [με]										
Mid-Span		Deck strain						Top flange of FPG strain			
Depth from top of deck [in]		3		4		5		6.875		8.375	
Load test	Mt [kin]	εT [με]	εG [με]	εT [με]	εG [με]	εT [με]	εG [με]	εT [με]	εG [με]	εT [με]	εG [με]
Pos 1	5386	-20.4	-1.3	-17.2	-1.1	-14.0	-4.7	-7.9	18.2	-3.1	20.2
Pos 2	2671	-9.2	-4.7	-7.8	-5.0	-6.3	-2.8	-3.6	2.3	-1.4	3.0
Pos 3	2671	-9.2	-4.1	-7.8	-3.0	-6.3	-2.3	-3.6	1.9	-1.4	2.5
Pos 4	5386	-20.4	-0.7	-17.2	0.3	-14.0	-3.7	-7.9	17.7	-3.1	20.1
Pos 5	1862	-7.1	0.2	-5.9	1.2	-4.8	-3.4	-2.7	4.9	-1.1	11.1
Pos 6	1862	-7.1	0.4	-5.9	4.0	-4.8	-2.1	-2.7	8.5	-1.1	3.9
Pos 7	1862	-7.1	-0.4	-5.9	0.6	-4.8	-0.5	-2.7	8.8	-1.1	3.3
Pos 8	1862	-7.1	0.2	-5.9	-1.4	-4.8	-0.3	-2.7	4.5	-1.1	8.6
Pos 9	1279	-4.9	-2.4	-4.1	-1.6	-3.3	-0.1	-1.9	0.8	-0.7	2.0
Pos 10	1789	-6.2	-3.2	-5.2	-3.9	-4.2	-0.9	-2.4	1.1	-0.9	1.6
Pos 11	3521	-13.4	1.9	-11.2	4.3	-9.1	-1.7	-5.2	16.4	-2.0	4.6
Pos 12	1883	-7.1	1.0	-6.0	4.8	-4.9	-2.1	-2.8	7.9	-1.1	2.2
Pos 13	1637	-6.2	0.9	-5.2	-0.2	-4.3	0.2	-2.4	7.1	-0.9	1.2
Pos 14	0	0.0	0.0	0.0	0.0	0.0	0.0	0.0	0.0	0.0	0.0

Mid-Span		Mid-height web of FPG strain				Bottom flange of FPG strain			
Depth from top of deck [in]		19.0625		20.5625		31.6875		33.1875	
Load test	Mt [kin]	εT [με]	εG [με]	εT [με]	εG [με]	εT [με]	εG [με]	εT [με]	εG [με]
Pos 1	5386	31.4	36.6	36.3	35.1	72.2	48.4	77.0	29.1
Pos 2	2671	14.2	19.6	16.4	22.8	32.6	38.0	34.8	22.1
Pos 3	2671	14.2	19.1	16.4	23.6	32.6	37.6	34.8	21.8
Pos 4	5386	31.4	35.9	36.3	38.8	72.2	47.7	77.0	31.4
Pos 5	1862	10.9	10.9	12.5	23.9	25.0	15.3	26.6	17.8
Pos 6	1862	10.9	17.1	12.5	11.9	25.0	23.0	26.6	9.5
Pos 7	1862	10.9	18.1	12.5	8.4	25.0	24.6	26.6	8.9
Pos 8	1862	10.9	10.2	12.5	14.4	25.0	14.4	26.6	15.7
Pos 9	1279	7.5	8.2	8.6	9.7	17.1	15.2	18.3	14.7
Pos 10	1789	9.5	16.3	11.0	7.2	21.9	33.4	23.4	9.1
Pos 11	3521	20.5	33.7	23.7	11.6	47.2	42.1	50.4	10.1
Pos 12	1883	11.0	17.5	12.7	6.3	25.2	21.3	26.9	4.6
Pos 13	1637	9.6	15.4	11.0	3.9	21.9	19.4	23.4	4.3
Pos 14	0	0.0	0.0	0.0	0.0	0.0	0.0	0.0	0.0

Table 4-5 Induced strain in deck and FPG due to Load test at ¼ span

Note:		ε_T = Theoretical 2D induced strain with respect to depth [με] ε_G = Average longitudinal gauge reading with respect to depth [με]							
Quarter-Span		Deck strain				Top flange of FPG strain			
Depth from top of deck [in]		3		4		6.875		8.375	
Load test	Mt[kin]	εT [με]	εG [με]	εT [με]	εG [με]	εT [με]	εG [με]	εT [με]	εG [με]
Pos 1	364	-1.4	-3.8	-1.2	-2.0	-0.5	-2.3	-0.2	1.1
Pos 2	-86	0.3	-2.3	0.3	-0.8	0.1	-1.7	0.0	0.7
Pos 3	2824	-10.7	-0.7	-9.0	-4.3	-4.2	8.8	-1.6	7.2
Pos 4	-56	0.2	-3.2	0.2	-1.8	0.1	-2.4	0.0	0.7
Pos 5	77	-0.3	-1.2	-0.2	-0.8	-0.1	-0.6	0.0	2.1
Pos 6	77	-0.3	-1.7	-0.2	-0.5	-0.1	-0.8	0.0	-0.4
Pos 7	77	-0.3	-2.5	-0.2	-1.6	-0.1	-2.1	0.0	-0.5
Pos 8	77	-0.3	-2.4	-0.2	-2.1	-0.1	-0.7	0.0	-1.3
Pos 9	262	-1.0	-3.0	-0.8	-1.5	-0.4	0.3	-0.1	0.0
Pos 10	-48	0.2	-2.3	0.2	0.6	0.1	-2.9	0.0	0.5
Pos 11	250	-0.9	-3.0	-0.8	0.6	-0.4	-2.9	-0.1	0.7
Pos 12	125	-0.5	-0.8	-0.4	1.2	-0.2	-1.0	-0.1	1.1
Pos 13	125	-0.5	-1.7	-0.4	0.0	-0.2	-1.8	-0.1	0.1
Pos 14	0	0.0	0.0	0.0	0.0	0.0	0.0	0.0	0.0
Quarter-Span		Mid-height web of FPG strain				Bottom flange of FPG strain			
Depth from top of deck [in]		19.0625		20.5625		31.6875		33.1875	
Load test	Mt[kin]	εT [με]	εG [με]	εT [με]	εG [με]	εT [με]	εG [με]	εT [με]	εG [με]
Pos 1	364	2.1	9.8	2.5	6.9	4.9	19.1	5.2	14.4
Pos 2	-86	-0.5	3.5	-0.6	1.6	-1.2	3.7	-1.2	1.9
Pos 3	2824	16.5	23.6	19.0	21.2	37.9	24.5	40.4	20.8
Pos 4	-56	-0.3	4.5	-0.4	4.1	-0.7	10.9	-0.8	8.1
Pos 5	77	0.4	2.1	0.5	5.7	1.0	3.0	1.1	3.4
Pos 6	77	0.4	4.1	0.5	2.4	1.0	4.9	1.1	3.0
Pos 7	77	0.4	5.8	0.5	4.0	1.0	11.2	1.1	6.6
Pos 8	77	0.4	5.2	0.5	4.5	1.0	8.3	1.1	11.3
Pos 9	262	1.5	8.0	1.8	5.6	3.5	9.4	3.7	13.1
Pos 10	-48	-0.3	3.3	-0.3	-2.4	-0.6	2.9	-0.7	1.7
Pos 11	250	1.5	8.0	1.7	-0.1	3.4	16.4	3.6	6.7
Pos 12	125	0.7	2.8	0.8	-2.0	1.7	4.5	1.8	1.3
Pos 13	125	0.7	5.0	0.8	0.3	1.7	11.7	1.8	5.1
Pos 14	0	0.0	0.0	0.0	0.0	0.0	0.0	0.0	0.0

4.4 Composite girder strain profile (at mid and ¼ Span)

In this section, the strain profiles on each girder were produced in order to verify the actual location of the neutral axes and to determine if strain distributions are linear with depth or not. Theoretical induced strains were calculated similarly to Section 4.3 and assuming even load distribution in the transverse direction. This assumption is not true in actual and is just used to show an approximate reference values. Plots of strain (both actual readings and calculated values) vs. vertical position of longitudinal strain gauges along the cross section were made separately for each girder at mid- span and ¼ - span, shown in Figure 4-5, Figure 4-6 and Figure 4-7 with blue dots represent field gauge readings and green lines represent calculated theoretical induced strains.

Result at mid-span: From the strain profile plots, it was observed the actual locations of neutral axes of each girder are higher (closer to the top of deck) than the calculated ones and non-linear strain distribution of actual gauge readings near the deck are captured in test Positions 1, 4, 5-8, 11-13. Besides, in these test positions, most of bottom flange gauges readings are smaller than theoretical one, see Table 4-4 for values of the readings. Since the bottom flange gauges are located near the edge, the possible reason for this could be strain distribution is not constant at the bottom flange. Moreover, in load test Position 1-4, where trucks were loaded on both exterior (G1 and G4) and interior girders (G2 and G3), Girder 1 tends to show larger differences in mid-height FPG strains compared to Girder 4 and it was found that the gauge SG144, which is located at the mid-height of the web (North side) of girder 1, constantly record larger readings than other gauges at similar location.

Nonetheless, in position 5 to 13, where trucks are loaded on a single girder or on interior girders only, the actual strain reading follows the sequence of the location of truckload in the load tests, i.e. maximum readings always appear at girders where the trucks are positioned. (Compare truck positions in Figure 4-2 and Figure 4-3 and strain profile plots in Figure 4-5 and Figure 4-6)

The cause of the non-linear strain distribution near the deck in test positions 1, 4, 5-8, 11-13 (e.g. the concrete deck strain and the FPG top flange strain on Girder 2 in Position 1 form a curve distribution) could be explained by the Saint-Venant's principle[1], which shows that, for a concentrated load, the transverse stress distribution can be highly non-linear at a location near the load, as shown in Case 1 of Figure 4-4. For the deck and top flange gauges located near the truck loads (less than 10 in [25.4 cm]), which are distributed transversely in the deck (see Figure 1-12), the actual strain profiles should be expected to be non-linear due to stress concentration when truck load is directly over the mid-span gauges. Accordingly, in the field data for test positions where truck axle loads are positioned at mid-span in test positions non-linear strain distribution was observed (Position: 1, 4, 5-8, 11-13), whereas when no truck axle load is positioned at mid-span the strain distributions were more linear (Position 2, 3, 9 and 10).

[1] *Saint-Venant's principle: The difference between the effects of two different but statically equivalent loads becomes very small at sufficiently large distances from load.*

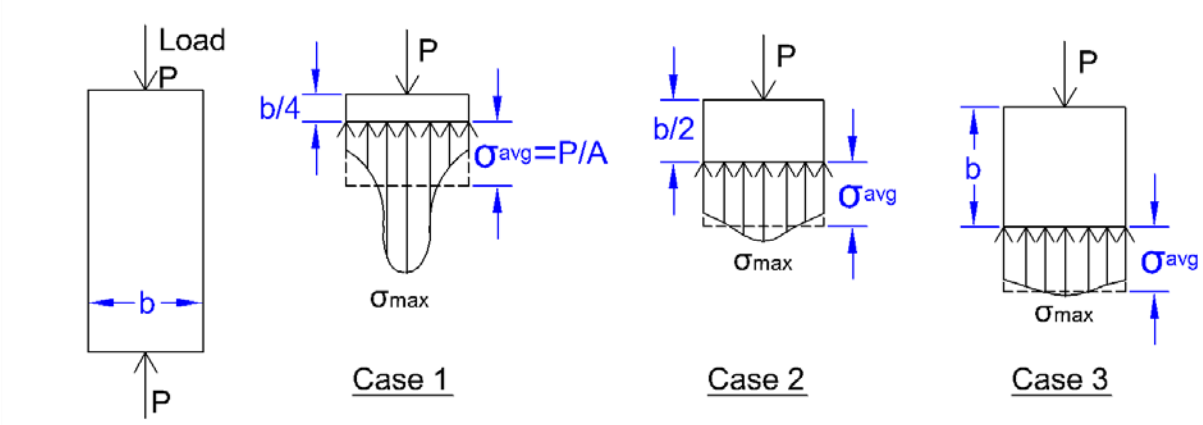

Figure 4-4 Stress distributions on a section due to concentrated load based on the distance to location of load[15]

Result at quarter-span: As only girders G3 and G4 are instrumented at quarter-span, the following results are assumed to be applicable to G1 and G2 but were not verified.

In the strain profile plots, non-linear strain distribution in gauge readings near deck is also captured in position 3, on which there are truck axle load directly on the instrumented quarter-span. On the other hand, theses plots clearly show that in positions other than position 3, the actual gauges readings are contrasting with the calculated theoretical values with most of the readings larger than the calculated values.

4.4.1 Summary

First, according to the Saint-Venant's principle, stress concentration is likely the reasons for the non-linear strain distribution captured in the actual gauge readings near the concrete deck. Second, the fact that the bottom flange gauges record smaller strain near the edge of bottom flange compared to the theoretical

values suggests that strain is likely not constant across the bottom flanges. This is likely due to shear lag effect happened at bottom flange and is confirmed later in Section 5.1. In other words, in test Position1, 4, 5-8, 11-13 at mid-span and in test Position 3 at quarter-span, stress concentration and shear lag effect are the reasons that cause the difference between actual strain readings and theoretical values. Last, the fact that maximum gauges readings in mid-span were recorded at where the trucks were loaded make sense and assure the validity of the field data to some what degree.

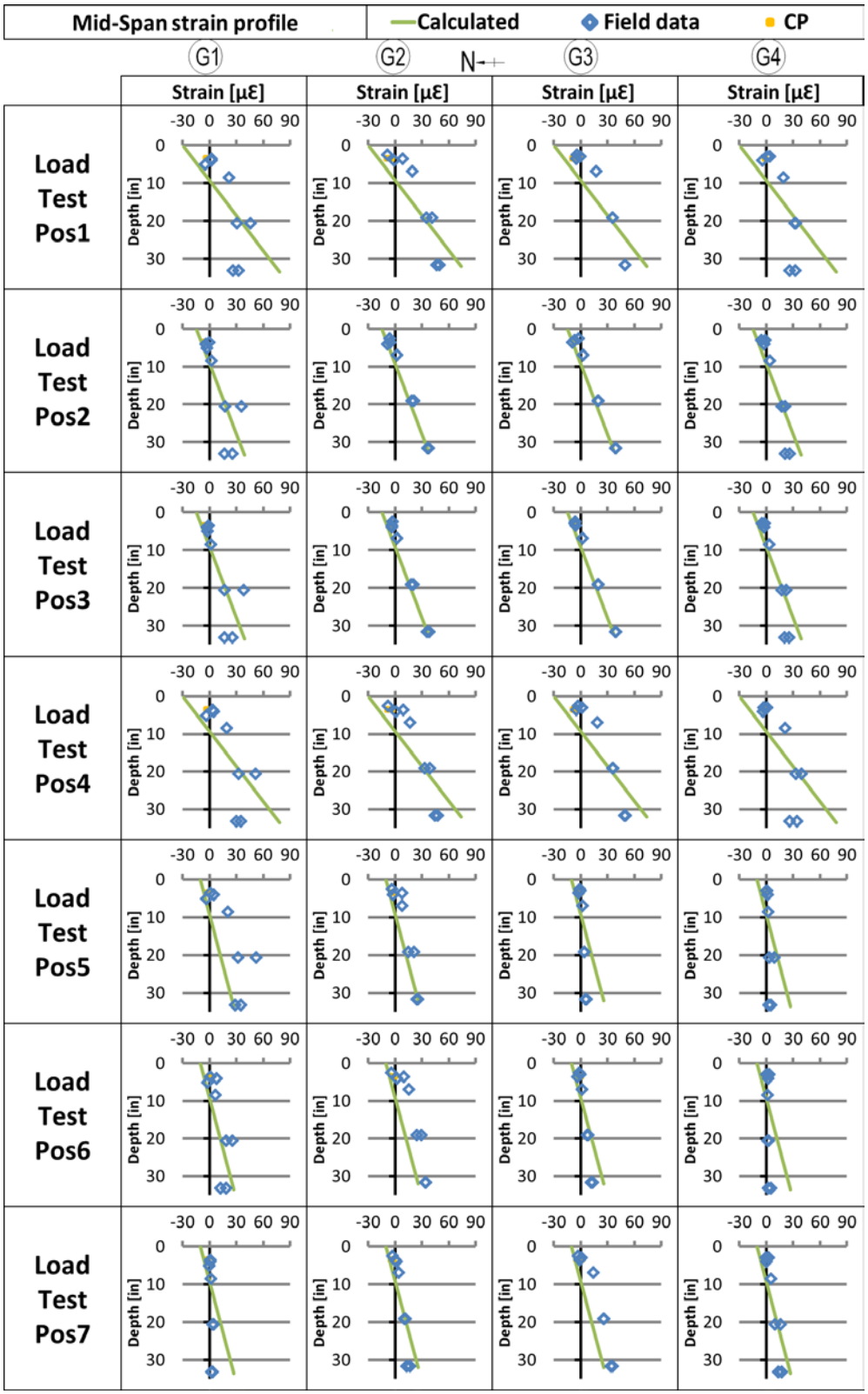

Figure 4-5 Strain profile along the depth of each girder at mid-span in Positions 1~7

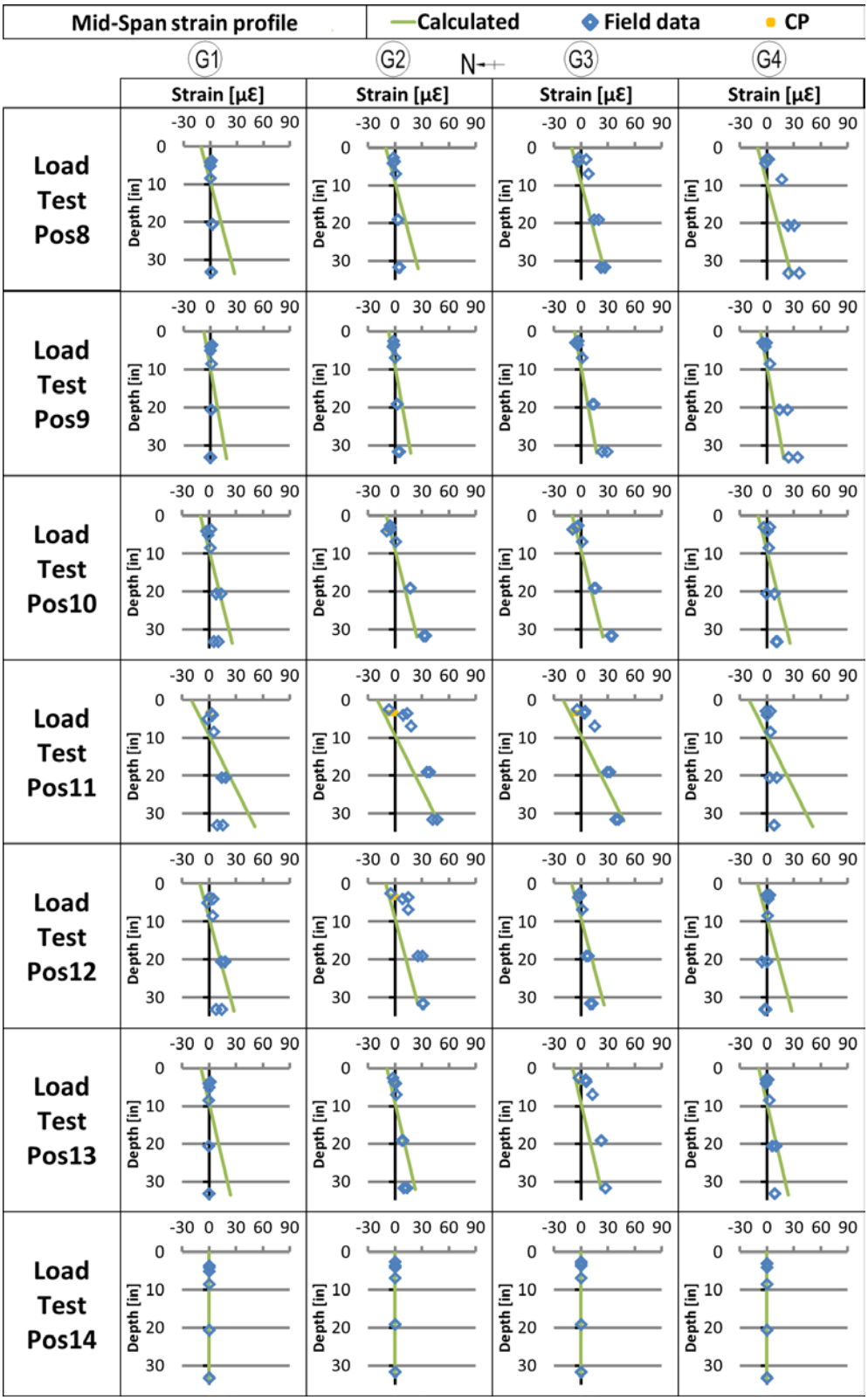

Figure 4-6 Strain profile along the depth of each girder at mid-span in Positions 8~14

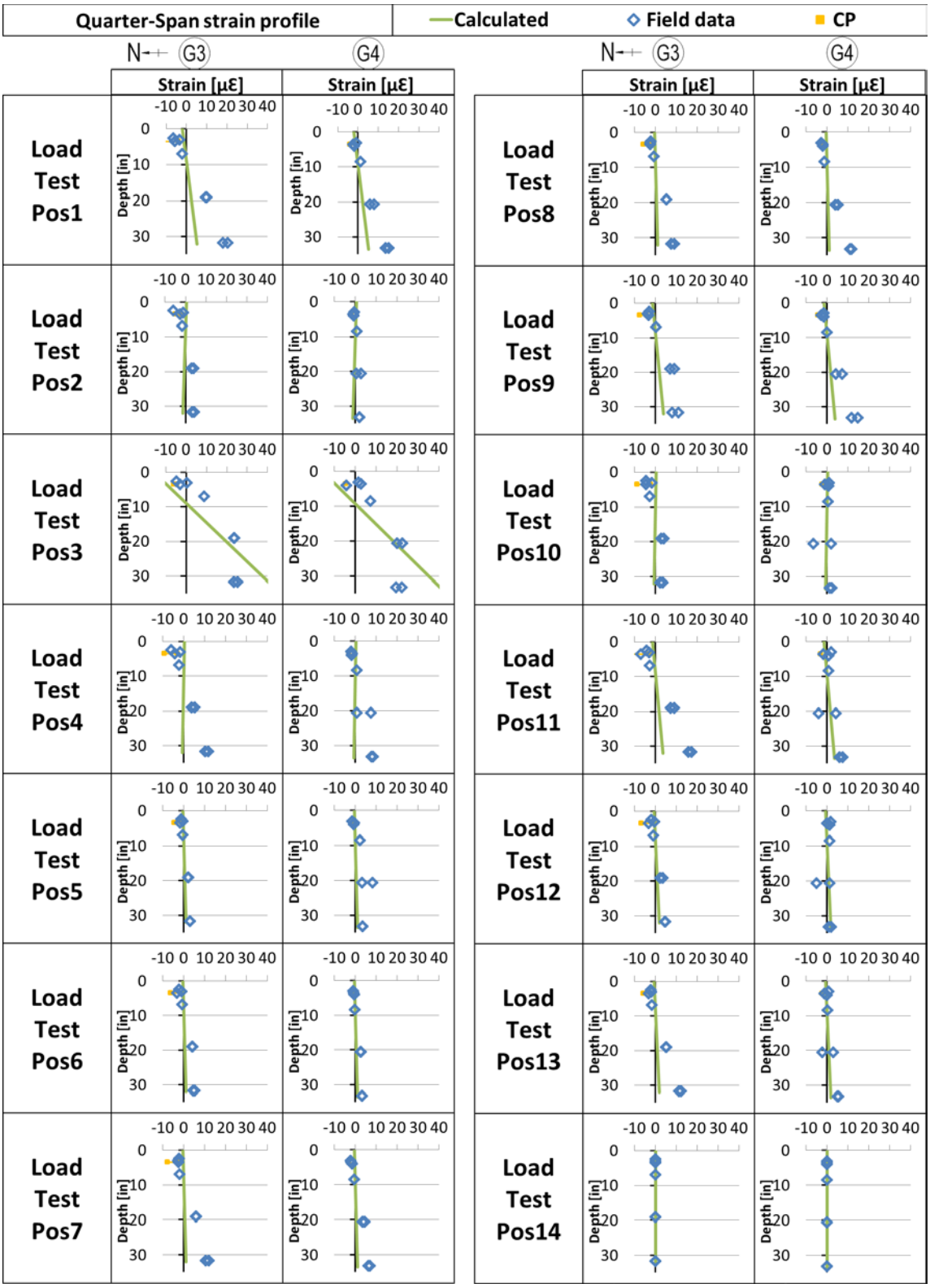

Figure 4-7 Strain profile along the depth of each girder at quarter-span

4.5 Moment distribution along the cross section (at mid and ¼ Span)

After comparing the actual strain readings and the calculated strain values, the load distributions in transverse direction (across the bridge) were of interest. Therefore, plots showing the transverse distributions of both actual along the cross section in each load test positions were created, and theoretical longitudinal moment and SAP2000 finite element analysis (FEA) result were also included in the plots to show comparison.

The actual moments in the bridge on each girder in each load test position were developed based on the actual strain gauge readings and the strain profile plots in Section 4.4. The strain profiles of each girder were first divided into small increment regions corresponding to a constant cross sectional area, with an assumption that the strain distributions between successive data points are linear, increment region for each girder are provided in Table 4-7. The actual strain readings in each region were next transformed into equivalent stress and then equivalent force by multiplying the elastic modulus of steel and then the corresponding portion of transformed cross section area, respectively. The calculation of force profile form strain profile is illustrated in Figure 4-8. The location of the forces inside each region is calculated based on the shape of the stress distribution in the region using Eq3. The actual neutral axes of each girder are calculated in each test position by using the strain profile and the average value of all positions is used for each girder, shown in Table 4-6, some values are omitted and marked in red whenever they are too large or too small compared to the average values. Finally, the actual moments were obtained by multiplying the forces

in each region the corresponding moment arm from the actual composite neutral axis.

$$Force\ location\ within\ region\ y' = \frac{top\ reading\ + 2 \times bottom\ reading}{3(top\ reading + base\ reading)} \times h \qquad \text{(Eq-3)}$$

Where h = Δy = the change in depth from top to bottom of the region, top and bottom = reading at the top and bottom of the region respectively. However, it must be noted that this calculation did not consider any stress concentration and shear-lag effect.

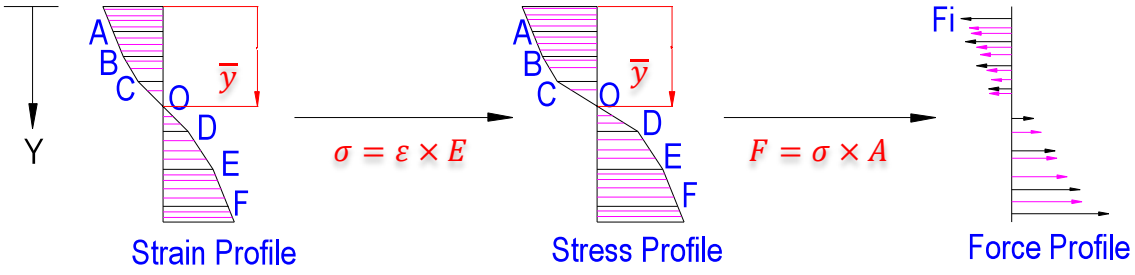

Figure 4-8 Illustration of calculation force profile from strain profile

Table 4-6 Elastic neutral axis of each girder based on strain gauge readings

ENA location from top of deck [in]	G1 mid-span	G2 mid-span	G3 mid-span	G4 mid-span	G3 1/4-span	G4 1/4-span
Load test 1	5.6	4.1	4.2	4.8	9.2	6.8
Load test 2	6.9	6.3	6.1	5.7	11.4	6.3
Load test 3	7.0	5.9	5.9	5.8	4.3	5.7
Load test 4	5.5	3.9	4.2	4.7	11.6	7.2
Load test 5	5.5	4.6	5.4	-0.9	9.7	5.2
Load test 6	5.8	3.5	5.9	13.6	8.9	10.3
Load test 7	5.8	2.7	3.8	3.8	10.0	9.9
Load test 8	6.6	6.4	4.4	4.5	8.4	11.2
Load test 9	5.2	6.6	6.0	5.8	6.5	8.4
Load test 10	6.5	6.7	6.5	2.7	13.3	10.6
Load test 11	5.8	2.8	2.4	3.7	10.4	19.9
Load test 12	6.2	2.7	5.8	10.4	10.8	12.7
Load test 13	6.0	3.8	2.7	5.0	10.2	4.9
Load test 14	0.0	0.0	0.0	0.0	0.0	0.0
AVG	6.0	4.6	4.9	4.6	10.0	8.3

Table 4-7 Increment region on each girder

	G1 mid-span	G2 mid-span	G3 mid-span	G4 mid-span	G3 1/4-span	G4 1/4-span
Increment region boundary depth from top of concrete deck [in]	0.00	0.00	0.00	0.00	0.00	0.00
	1.50	1.50	1.50	1.50	1.50	1.50
	3.50	2.50	2.50	3.00	2.50	3.00
	4.00	3.50	3.00	4.00	3.00	3.50
	5.00	4.00	3.50	4.64	3.50	4.00
	6.04	4.63	4.86	6.50	6.50	6.50
	6.50	6.50	6.50	8.00	7.00	8.00
	8.00	7.00	7.00	8.50	10.02	8.27
	8.50	11.00	11.00	12.50	11.00	8.50
	12.50	15.00	15.00	16.50	15.00	12.50
	16.50	19.00	19.00	20.56	19.00	16.50
	20.56	23.00	23.00	24.56	23.00	20.50
	24.56	27.00	27.00	28.56	27.00	24.50
	28.56	31.56	31.56	33.06	31.56	28.50
	33.06	32.06	32.06	33.56	32.06	33.06
	33.56					33.56

The theoretical moment on each girder was calculated from the theoretical gross moment in mid-span and quarter-span obtained before in Section 4.1, in which the bridge was assumed to act as a single two dimensional beam with fixed end condition. Even transverse distribution was used when calculating the theoretical moment on each girder to show as a reference in the plots, i.e. moment on each girder = gross moment / 4 (girders).

The FEM moment responses in each test position of the SAP2000 FEM were obtained by using section-cuts defined on mid-span and quarter-span on each girder, in which the summation of forces were obtained at the hand-calculated centroid of each girder.

The results are plotted in Figure 4-9, Figure 4-10, and **Error! Reference source not found.**. Also, the values of the plots were shown in Table 4-8 and Table

4-9, note that in Table 4-8 the hand calculated 2D moments represent the total moments at mid-span whereas in Table 4-9 they represent half of the total moment in quarter-span.

Table 4-8 Actual moments at mid-span compared with FEM results and hand calculation.

Mid-Span	Field data Moments [kip-in]					FEM Moment [kip-in]					Hand Calc. [kip-in]
	G1	G2	G3	G4	Sum	G1	G2	G3	G4	Sum	
Pos1	809	1003	1001	799	3612	1030	1606	1604	1081	5322	5386
Pos2	526	849	792	536	2703	543	765	787	585	2680	2671
Pos3	516	732	739	531	2519	525	759	786	584	2654	2671
Pos4	842	1043	1010	835	3729	1038	1576	1619	1096	5330	5386
Pos5	827	539	139	110	1614	992	723	64	14	1793	1862
Pos6	416	797	266	75	1553	446	1123	334	16	1920	1862
Pos7	76	309	686	349	1420	12	406	1166	371	1955	1862
Pos8	32	134	501	733	1400	11	64	752	1003	1829	1862
Pos9	10	136	505	617	1268	12	63	517	756	1349	1279
Pos10	196	782	701	204	1883	196	738	733	203	1869	1789
Pos11	321	1033	900	195	2449	337	1497	1439	332	3606	3521
Pos12	307	755	243	-40	1266	329	1154	413	16	1913	1883
Pos13	-11	228	651	213	1081	8	343	1026	316	1693	1637
Pos14	0	0	0	0	0	0	0	0	0	0	0

Table 4-9 Actual moments at ¼ -span compare with FEM results and hand calc.

Quarter-Span	Field Moment [kip-in]			FEM Moment [kip-in]			Hand Calc. [kip-in]
	G3	G4	Sum	G3	G4	Sum	
Pos1	359	261	620	170	222	392	364
Pos2	134	46	180	-230	-225	-455	-86
Pos3	735	455	1190	883	869	1752	2824
Pos4	251	158	409	-148	-108	-257	-56
Pos5	68	86	154	24	24	48	77
Pos6	105	60	165	24	31	55	77
Pos7	243	134	377	10	48	59	77
Pos8	146	208	354	20	44	64	77
Pos9	263	229	492	51	98	150	262
Pos10	176	283	460	-175	-105	-280	-48
Pos11	352	455	807	130	142	272	250
Pos12	106	573	679	55	55	110	125
Pos13	236	113	349	75	87	162	125
Pos14	0	0	0	0	0	0	0

Result: First, at mid-span, the SAP2000 FEM result shows similar sum values to the theoretical values (shaded values) which assume fixed end conditions, the

maximum differences between them are about 10% with most of the FEM results larger than the theoretical one (see Table 4-8), this implies that the support condition in the SAP2000 model (provided by the integral abutments) is close to but slightly less than fully fixed. On the other hand, in quarter-span, the FEM result shows quite different values to the theoretical one, this might because the point of inflection of longitudinal moment in the SAP2000 model is different from the theoretical one due to the above mentioned slightly different support condition in the model, and therefore will result in quite different values in quarter-span since the point of inflection of longitudinal moment is located near quarter span, this also applied between the SAP2000 model and the actual bridge.

Second, the actual moment show smaller values (ranging from 10% to 60% smaller) in test Position 1, 4, 5-8, 11-13 at mid-span and in test Position 3 at quarter-span at girders located near the truck load compare to the SAP2000 FEM moment, while the actual moment show close values in other test position at mid-span (see Table 4-8 and Table 4-9). This strengthened the summary conclusion about stress concentration and shear lag effect in session 4.4. Since stress concentration decreases the compression strain above centroid and shear-lag will cause smaller tensile strain at the edge of bottom flange (where the gauges are located), and results in smaller strain readings at these locations and therefore a smaller moment values as calculation did not consider the non-constant strain distribution at bottom flange due to shear-lag.

Last, from the moment distribution plots in Figure 4-9, Figure 4-10 and **Error! Reference source not found.**, the FEM was able to capture the transverse

moment distribution between girders as it show similar shape compared to the actual values. In position 1 to 4, interior girders appear to be carrying more moment than exterior girders observed at mid-span. However, in these positions the truck axle loads are actually closer to the interior girders than the exterior girders. (For each interior girder, there are 2 truck axle loads that are close to it, whereas there are only 1 truck axle load that is close to each exterior girder. See Figure 4-2 for truck live load test Position 1 to 4). Therefore, it is likely that the exterior and interior girders take up load approximately evenly. On the other hand, in position 5 to 8 at mid-span where trucks are loaded longitudinally, the plots show that loads mostly affect adjacent girders and have very little effect on girders that are farther than adjacent girders.

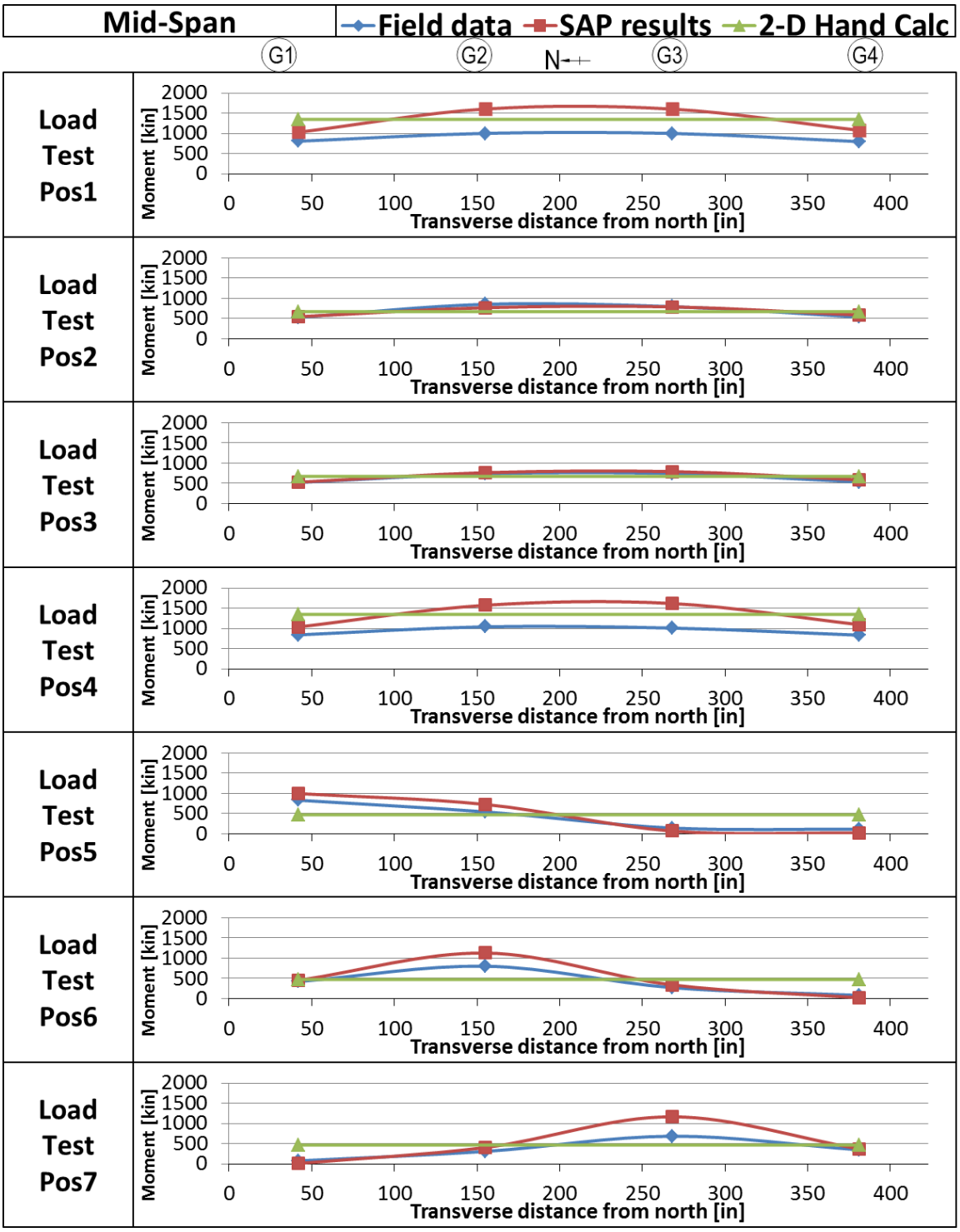

Figure 4-9 Transverse distribution of longitudinal moment at mid-span in Pos1~7

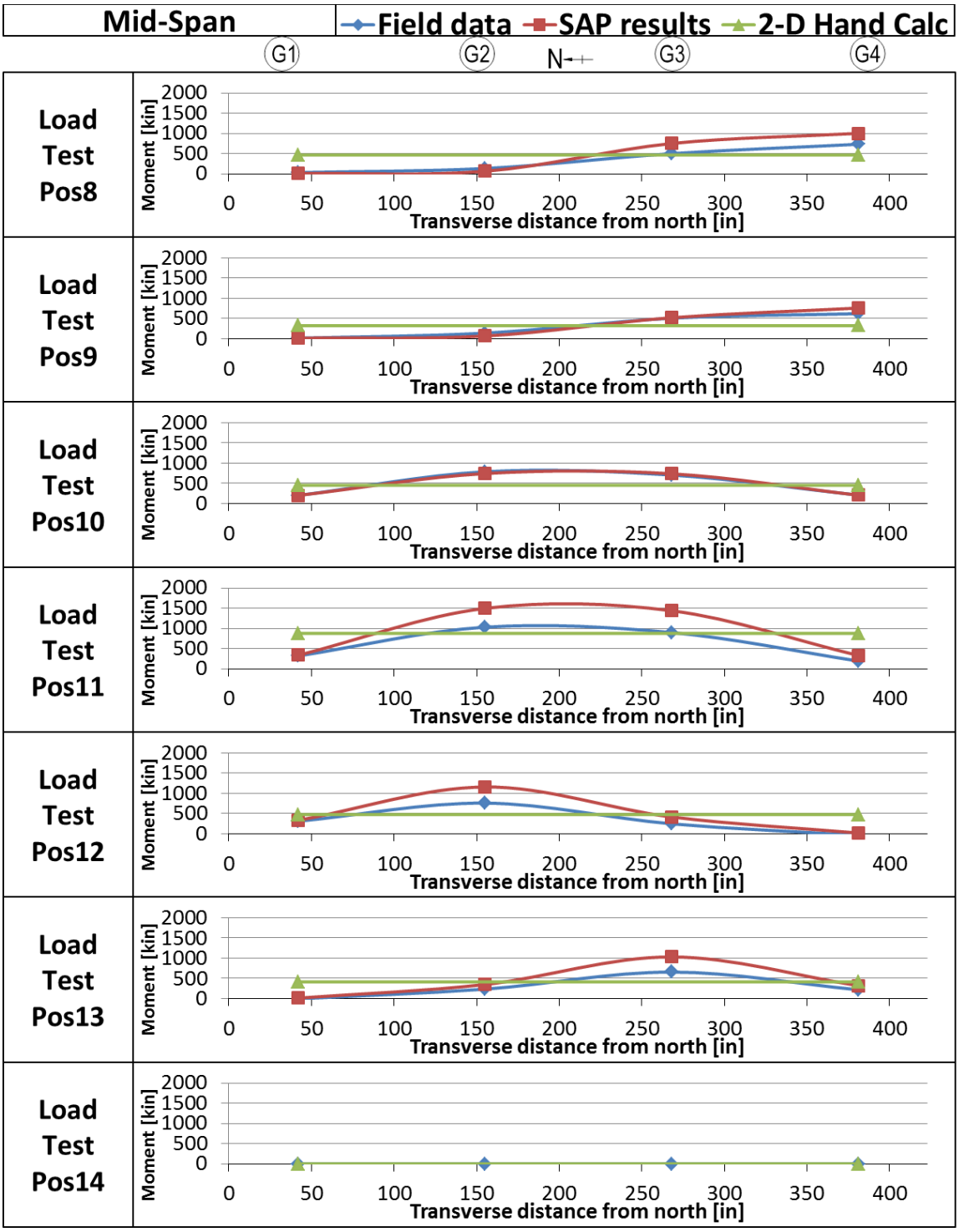

Figure 4-10 Transverse distribution of longitudinal moment at mid-span in Pos8~14

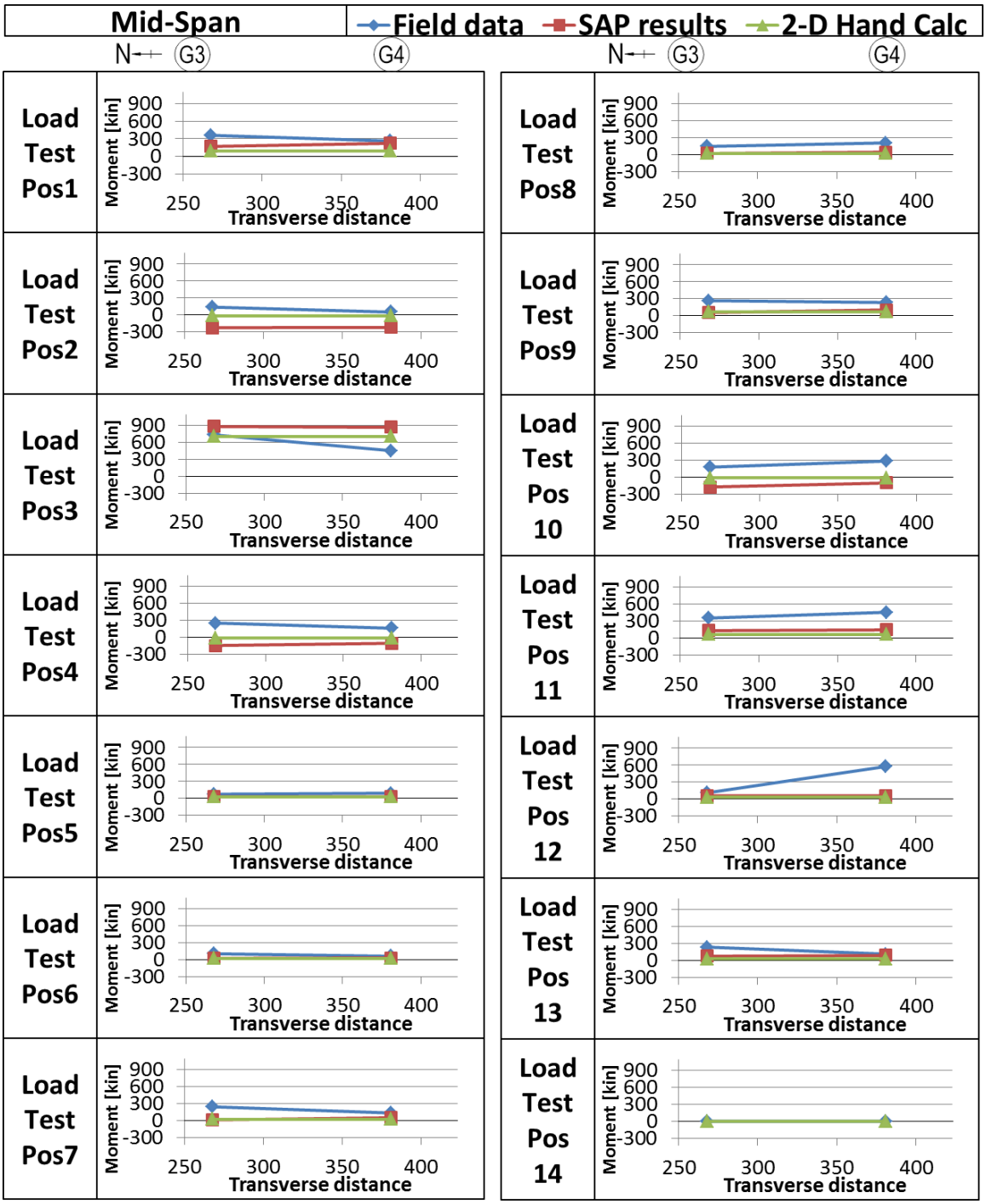

Figure 4-11 Transverse distribution of longitudinal moment at quarter-span

CHAPTER 5
SHEAR LAG EFFECT AT FPG

In order to further investigate the effect of stress concentration at the deck and the shear lag at bottom flange of FPG captured in the live load field data in Section 4.4, a more specific FEM was created in ANSYS mechanical APDL. This ANSYS model consists of the superstructure of the bridge and is able to capture the stress distribution throughout the bridge section. For detail of the model, see Section 2.2. Furthermore, the shear effect under self-weight effect and thermal loading were also evaluated.

5.1 Live load testing (in selected live load positions)

Since the purpose of this section is to verify the stress concentration and shear lag effect, not all the load test positions were modeled. Instead, live load test Position 3, 4 and 7 were chosen to be modeled for the following reasons: these positions showed significant non-linearity in the strain profile; Position 4 is the most significant position to mid-span gauge readings as heavy axles of live load truck are placed at mid-span; Position 3 does not have loads being placed at mid-span and heavy axles of live load truck were placed at the instrumented quarter-span and therefore have significant effect on quarter-span gauges; Position 7 has all truck loads placed on a single girder which will be indicative when comparing the load distribution across the section of the bridge. The analysis results of the three conditions were obtained and compared.

The ANSYS results were obtained using path operation in ANSYS in which the path is defined on girders cross section and strain result along the path were then retrieved from the analysis results, the path used on each girder is shown in Figure 5-1. As in the figure, points A and B represent the strain at top and bottom of concrete deck, points C, D, E and F represent the strain at top and bottom of the web of FPG, and points F and G represent the strain at web to bottom flange location and the edge of bottom flange. Also, only the web and flange with larger strain is reported while the strain results at where the actual gauges are installed are retrieved on both sides.

Strain profile plots consist of ANSYS results and actual field data were created. The legend of the strain profile plots is shown in Figure 5-1, while mid-span plots are shown in Figure 5-4 and quarter-span plots are shown in Figure 5-5. In these strain profile plots, blue dots represent field data, green lines represent the theoretical 2D hand calculated values (average value for all girders neglecting load distribution across the bridge), and red symbols represent the strain results from ANSYS. The strains at the north side web and flange are indicated with a plus symbol“+”, whereas strains at the south side are indicated with a diamond symbol “◇”. The inner edge bottom flange gauge field reading and the point G reading in ANSYS are filled with black color for the ease of comparison.

In mid-span plots, the ANSYS results show a better correlation to the field data; non-linear strain distribution and the shear lag effect that found in field data (see Section 4.4) were also captured in the ANSYS result. Same as in the field data, non-linear strain profile were captured only in test positions with trucks directly

loaded at mid-span (Position 4 and Position 7) in the ANSYS result, while in other test position (Position 3) the strain profile is linear. This verified that stress concentration is likely the reason causing non-linearity in the strain profile of the field data. Second, the shear lag effect at the bottom flange of FPG was captured at all girders in Position 4 and at Girder 3 in Position 7 in the ANSYS result. The longitudinal strain distribution of the bridge cross-section at mid-span in Position 4 is shown in Figure 5-2 and is compared to gauges locations in Figure 5-3, it clearly shows that the strain distribution at the bottom flange of FPG is not constant, but decreasing from web-to-flange intersection to the inner edge of the flange, and is known as positive shear-lag. In Figure 5-4, the ANSYS model bottom flange strain shows a close result to the field data (compare filled dots). All of these verified that shear lag effect occurs in the bottom flange and is the cause of the smaller readings (compare to theoretical) at bottom flange gauges recorded in field data observed in Section 4.4. Third, the mid-height web ANSYS results were also close to the field data readings except the gauge SG144 located at the north side of girder 1 (shown as M1 or blue "+" in Figure 5-4). This shows again the gauge recorded typically larger readings compared with other gauges during load testing. Lastly, there is no shear lag captured in the top flange of FPG in ANSYS result as expected, since the top flange is vertically braced by the concrete deck and large shear deformation is prevented.

In quarter-span plots, similar results were obtained in the ANSYS result. Both non-linear strain profiles and shear lag effect were captured in Position 3, in which

trucks were loaded at quarter-span. Whereas in Position 4 and Position 7, both the ANSYS result and the field data are close to zero reading.

Strain values at the web-to-bottom flange junction were predicted for Position 4 to show comparison with the ANSYS model results, the values were predicted based on the theoretical neutral axis location and the web gauge field reading, shown in Table 5-1. Note that the 2 in concrete overlay and closure pour were considered when calculating the theoretical neutral axis. Also, since the north-side web gauge in Girder 1 was found to give typically larger values, the south side gauge was used instead in Girder 1 predicted values (showed as G1'). Result show that the predicted values were close to the ANSYS result (shaded values).

The Longitudinal strains on FPG bottom flange of Girder 2 due to Live Load Position 4 are plotted in Figure 5-6, this figure shows the comparison between longitudinal strains at the web-to-flange junction and at the edge of bottom flange. The figure shows that positive shear lag happened at mid-span (where the truck axle loads are concentrated on), while negative shear lag effect happened near the two tie-plates which are located about 60in [1.5m] away from mid-span.

In conclusion, the ANSYS model is able to capture stress concentration and shear lag effect along the cross-section of the bridge and verified the non-linear strain distribution in the FPG under concentrated loads.

Table 5-1 Predicted strain values at web-to-flange junction for test Position 4

Position 4 strain (με)	G1'	G2	G3	G4
Centroid location from bottom of FPG	25.38	24.80	24.80	25.38
Web gauge location from bottom	13.00	13.00	13.00	13.00
Web gauges field reading	32	38.51	36.23	39.11
Predicted value at web-to-flange junction	60.08	73.59	69.23	73.07
ANSYS values	60.24	73.56	74.70	60.95

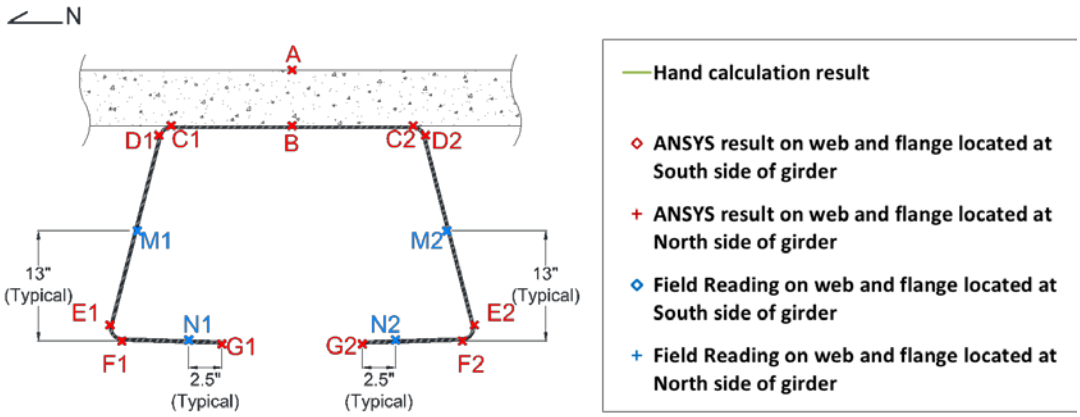

Figure 5-1 ANSYS result query path and legend of strain profile plots used in this Chapter

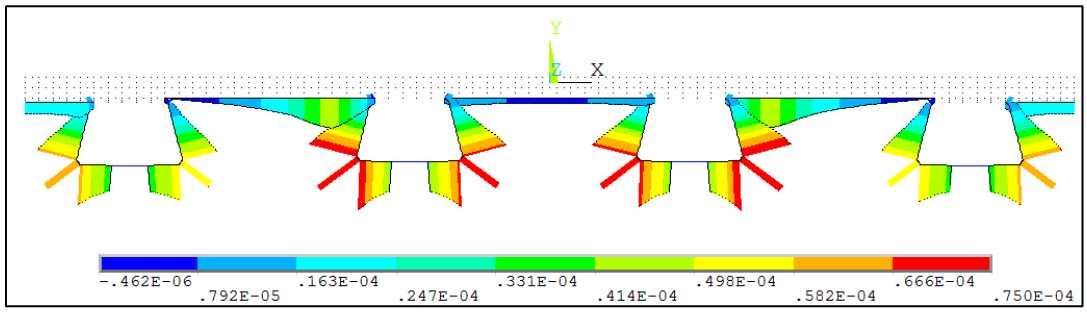

Figure 5-2 Mid-span longitudinal strain distribution in Position 4

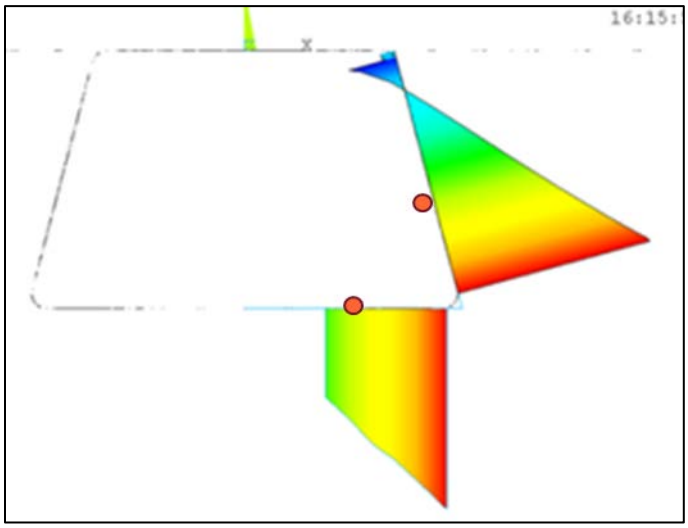

Figure 5-3 Strain distribution versus gauges locations

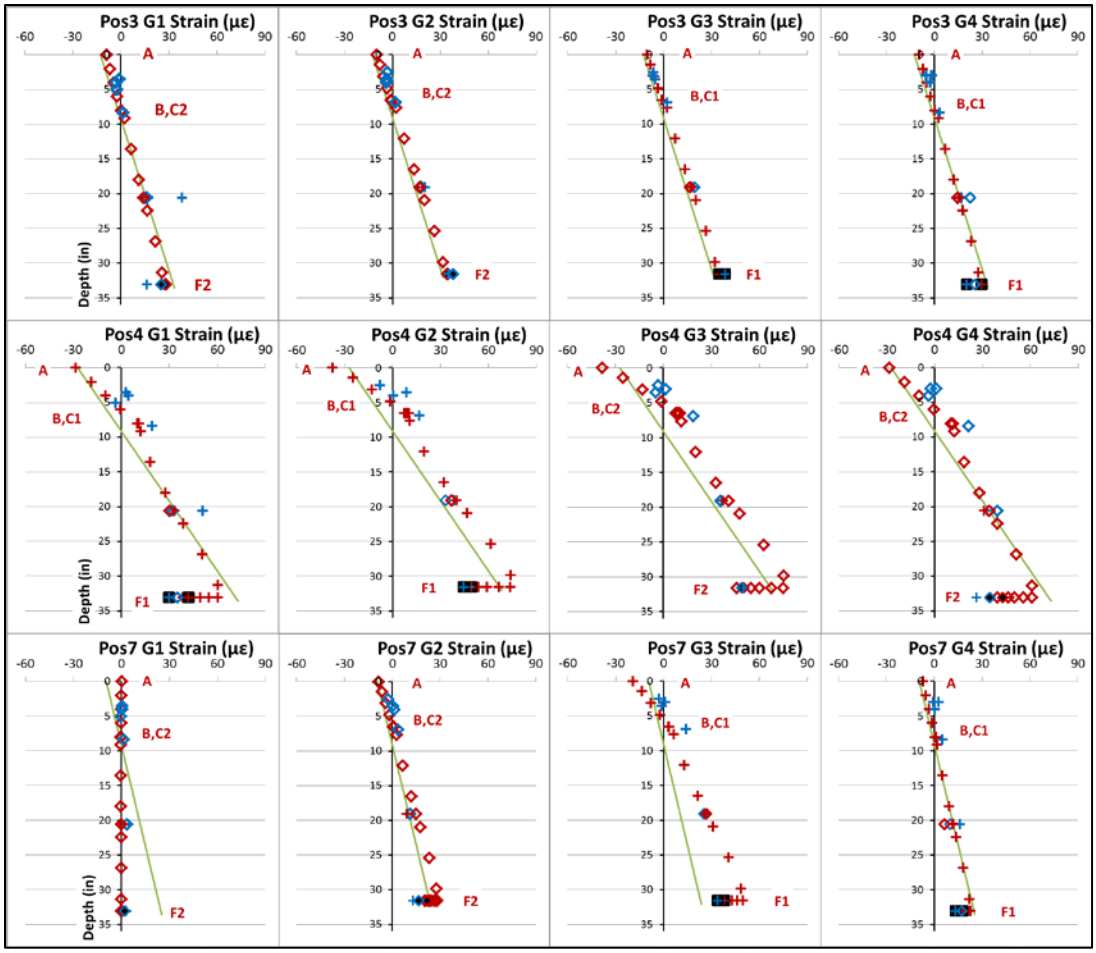

Figure 5-4 Mid-span strain profile plots of Pos3, Pos4 and Pos7

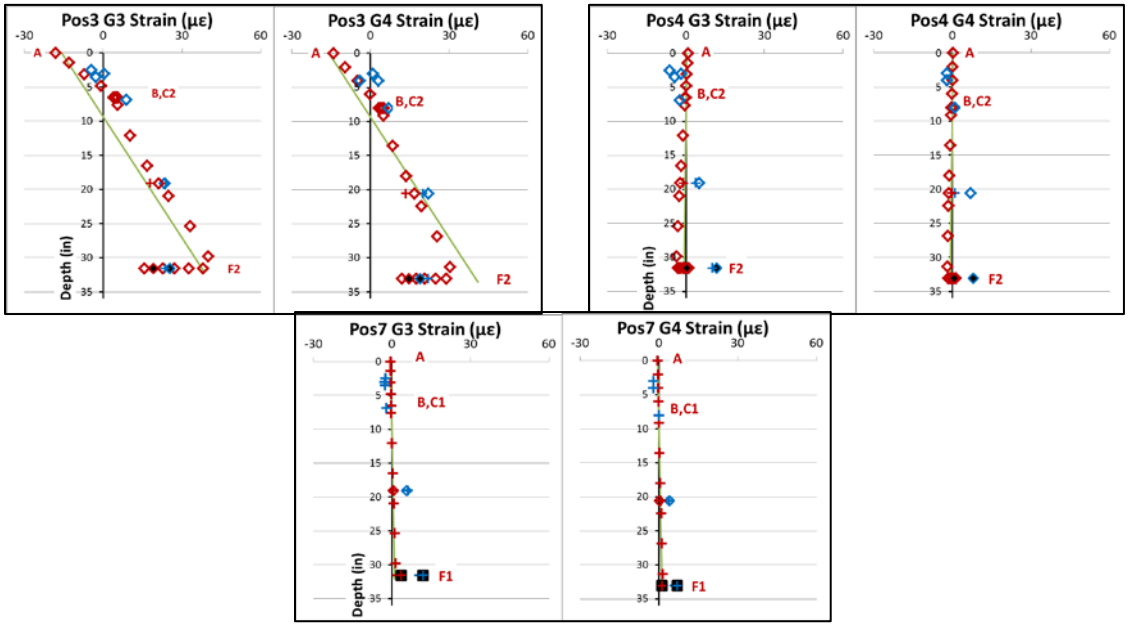

Figure 5-5 Quarter-span strain profile plots of Pos3, Pos4 and Pos7

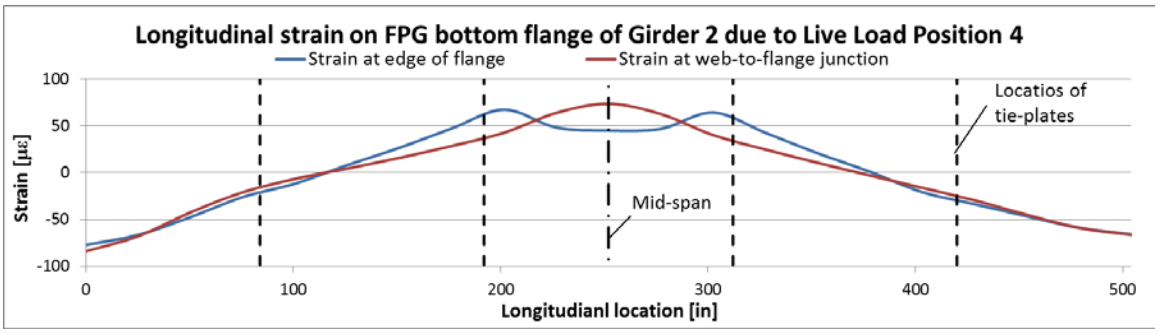

Figure 5-6 Longitudinal strain on FPG bottom flange of Girder 2 due to Live Load Position 4

5.2 Effect of bottom flange tie-plate

In this section, the effect of the bottom flange tie-plate on the shear lag effect is evaluated in ANSYS APDL. The ANSYS model was modified such that all the tie-plates were taken out. The result in test Position 4 of the modified model were obtained and compared with the original model in Figure 5-7 and Table 5-2.

Results show that the shear lag effect in a model without tie-plates is more significant, in which it results in larger strain values at FPG web-to-bottom flange junction and smaller values at the inner edge of bottom flange compare to the model that include tie-plates. This shows that the tie-plates have effect in restraining the bottom flange from shear deformation and subsequently reduced the stress concentration due to shear lag at the FPG web-to-bottom flange junctions. Note that the maximum strain value in the model without tie-plates is only about 88 με, which is equivalent to 2.6 ksi [17.9 MPa] in the steel FPG and is still a low value. However, the FPG section is more efficient in resisting concentrated loads when tie plates are provided.

Table 5-2 Comparison between model with and without bottom flange tie-plates

Position 4	Model with tie-plate				Model without tie-plate			
Strain values (με)	G1	G2	G3	G4	G1	G2	G3	G4
Bottom flange-to-web junction	60.2	73.8	75.0	60.9	71.5	86.4	87.8	72.4
inner edge of bottom flange	38.5	45.0	45.6	39.2	10.9	12.5	12.8	11.2

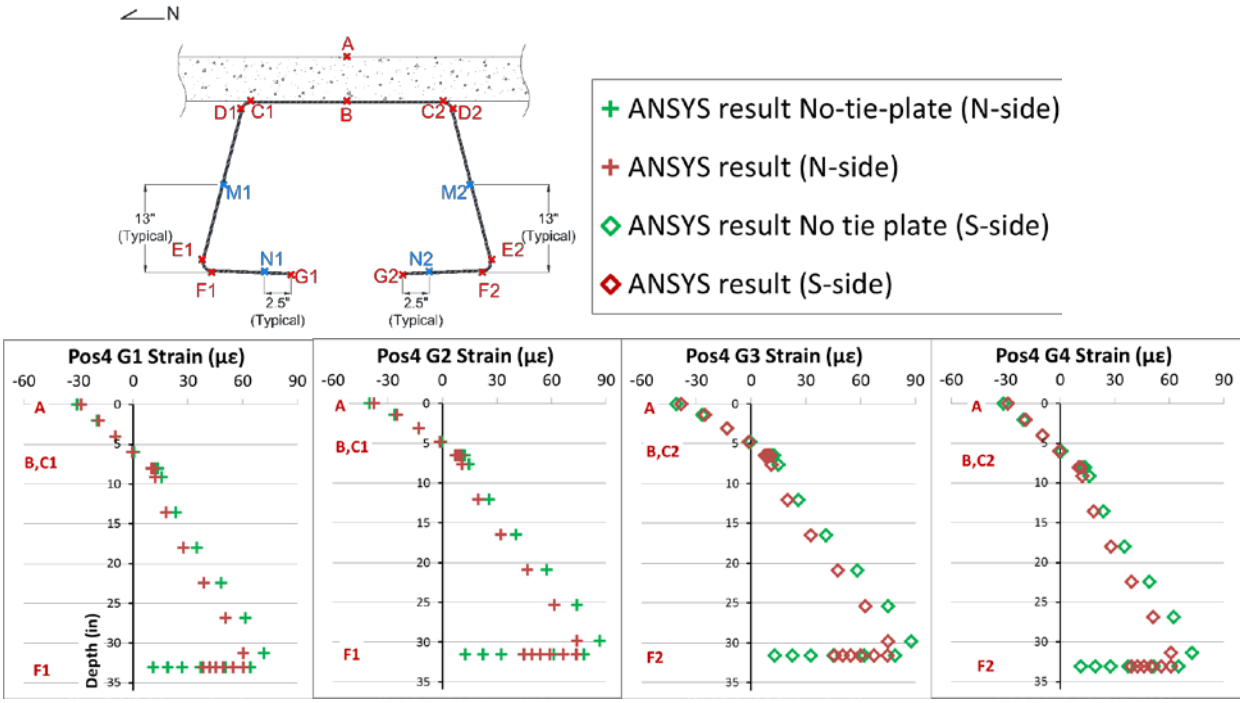

Figure 5-7 Comparison between model with and without bottom flange tie-plates

5.3 Comparison between wide flange steel girder

In this section, a FPG was compared to a wide flange steel girder to see if the same shear lag effect would happen on W-shape steel, which is very popular in typical girders. The ANSYS model was modified to have one of the FPG steel interior girders changed to a W-shape steel girder with an equivalent section modulus, and load conditions in test Position 4 was applied to the model to see the difference between the two girders. A W30x148 section was chosen, the section modulus is

436 in^3 [7145 cm^3] and that of the FPG is 439 in^3 [7194 cm^3]. The section view of the modified model is shown in Figure 5-8.

Strain results are shown in Figure 5-9 and Figure 5-10, in which Figure 5-9 shown the strain distributions on the two girders, and Figure 5-10 shown the comparison of the strain profiles between the two girders. Results show that the shear lag effect on the W-shape steel girder is minimal compare to that on the FPG. This result suggests that the shear lag effect on the w-shape steel can be neglected, while the shear lag effect on the FPG may be significant for concentrated loads.

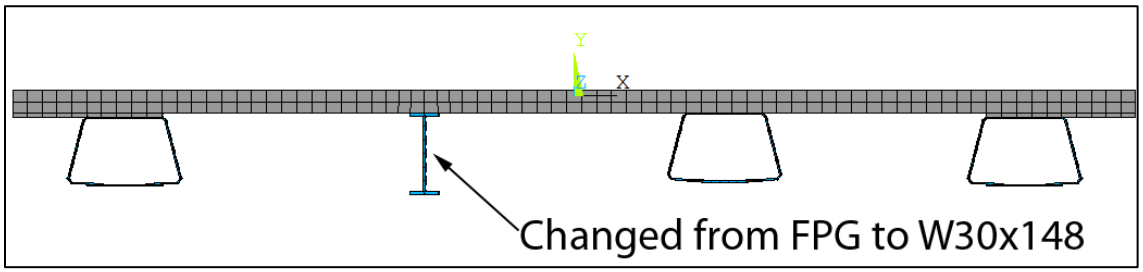

Figure 5-8 Section view of the modified ANSYS model

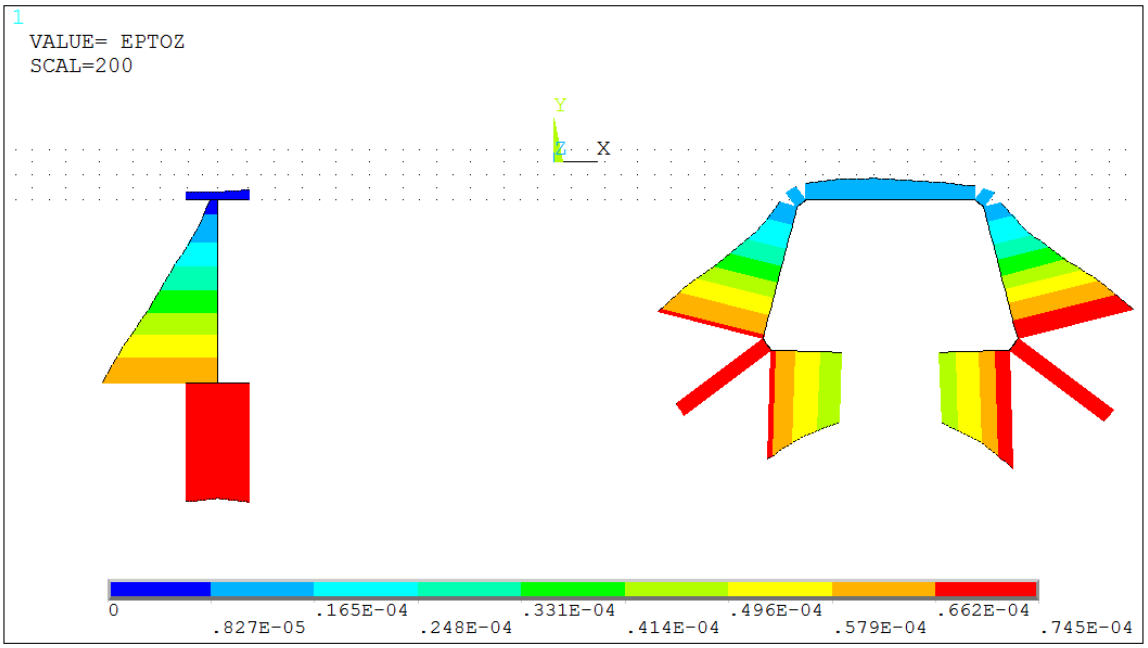

Figure 5-9 Strain distribution of FPG and w-shape steel under Position 4 load conditions

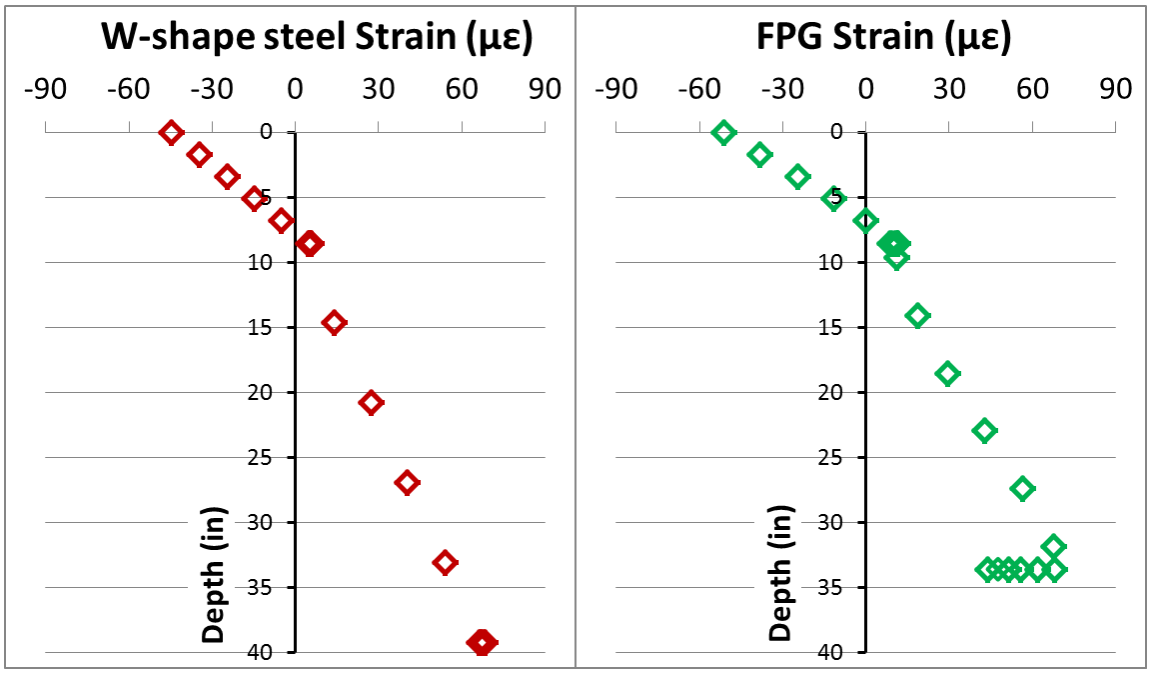

Figure 5-10 Strain profile of FPG and w-shape steel under Position 4 load conditions

5.4 Shear lag effect under self-weight of bridge

Since shear lag effects were captured in the load test field data and FEA result, an additional FE run was completed to verify if shear lag effects are negligible under self-weight distributed loading.

The model used in this section is similar the one used in Section 2.2, except center-to-center of abutment span (46 feet) and pin-pin support condition were used instead in this section. A gravity of 386.4 in/s^2 [9.81 m/s^2] was defined in the model and the analysis results were obtained. The longitudinal strain distribution of the bridge cross-section is shown in Figure 5-11. The strain profiles of interior (G2 and G3) and exterior section (G1 and G4) at mid-span were plotted in Figure 5-12.

The longitudinal strain on FPG bottom flange of Girder 2 due to self-weight effect is plotted in Figure 5-13.

Figure 5-12 shows that the ANSYS result at mid-span is close to the theoretical result obtained in Section 3.3 and that the strain at the inner edge (point G) of bottom flange is about the same as the strain at the web-to-flange intersection (Point F) in both interior and exterior section under self-weight effect of the bridge. Figure 5-13 shows that the strains at the web-to-flange junction and at the edge of the bottom flange are very close along the length of the girder except at the ends/supports, where strain values are relatively small. Therefore, based on this FEA result, shear lag effects are not relevant to self-weight loading.

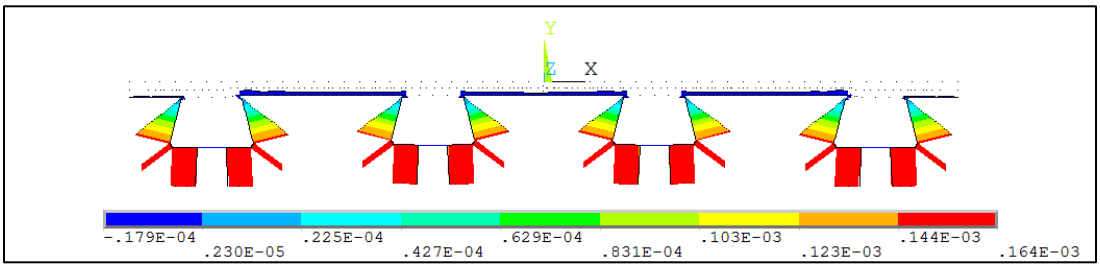

Figure 5-11 Longitudinal strain distribution of cross-section due to self-weight effect at mid-span

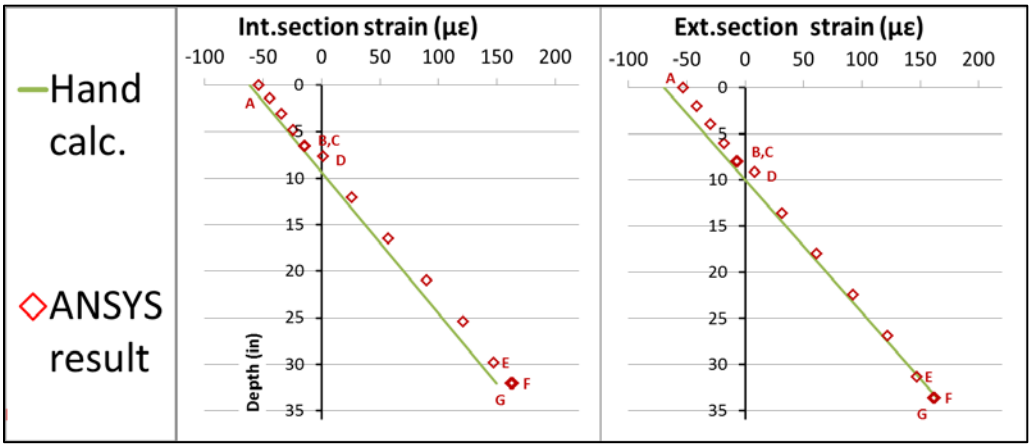

Figure 5-12 Strain profile of interior and exterior section at mid-span due to self-weight effect

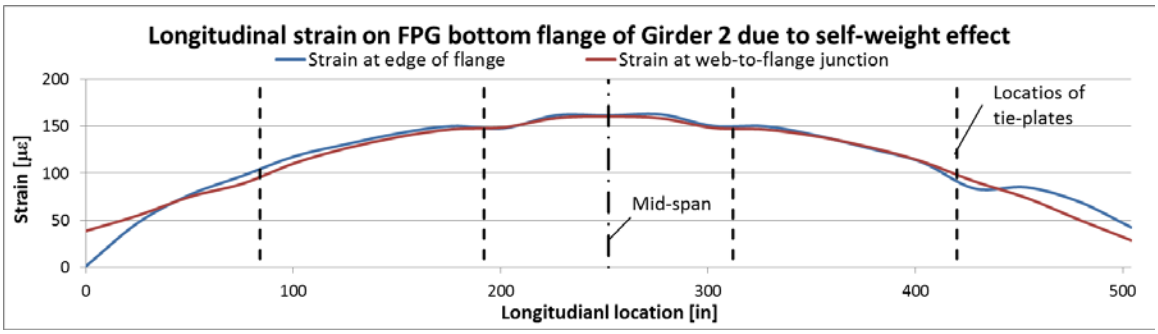

Figure 5-13 Longitudinal strain on FPG bottom flange of Girder 2 due to self-weight effect

5.5 Shear lag effect under thermal loading

Additional ANSYS APDL FEM was performed to verify that shear lag effects were negligible for thermal loads. The model used in this section was a model developed to analyze the seasonal behavior of bridge later in the paper. The model consists of both the superstructure and the substructure of the bridge; see Section 2.3 for more details of the model.

The effects of both constant temperature and gradient temperature were evaluated, and the ANSYS results at mid-span for models under the two different thermal loadings are shown in Figure 5-14. Also, longitudinal strains on FPG bottom flange of Girder 2 are shown in Figure 5-15. From Figure 5-14, no significant shear lag effect was found in the bottom flange under both constant temperature and gradient temperature at mid-span. Whereas Figure 5-15 shows that the strain values at the web-to-flange junction and at the edge of the bottom flange are very close under the two type of loading, except for strains under constant temperature change at location near the two tie-plates that are about 60in [1.5m] away from mid-span, there is about 10 με difference . Overall, shear lag effect is not significant

under the distributed temperature loading (especially at mid-span and quarter-span) and therefore all long-term data reported at bottom flanges of the FPG sections represent typical values for the extreme fiber of the cross section.

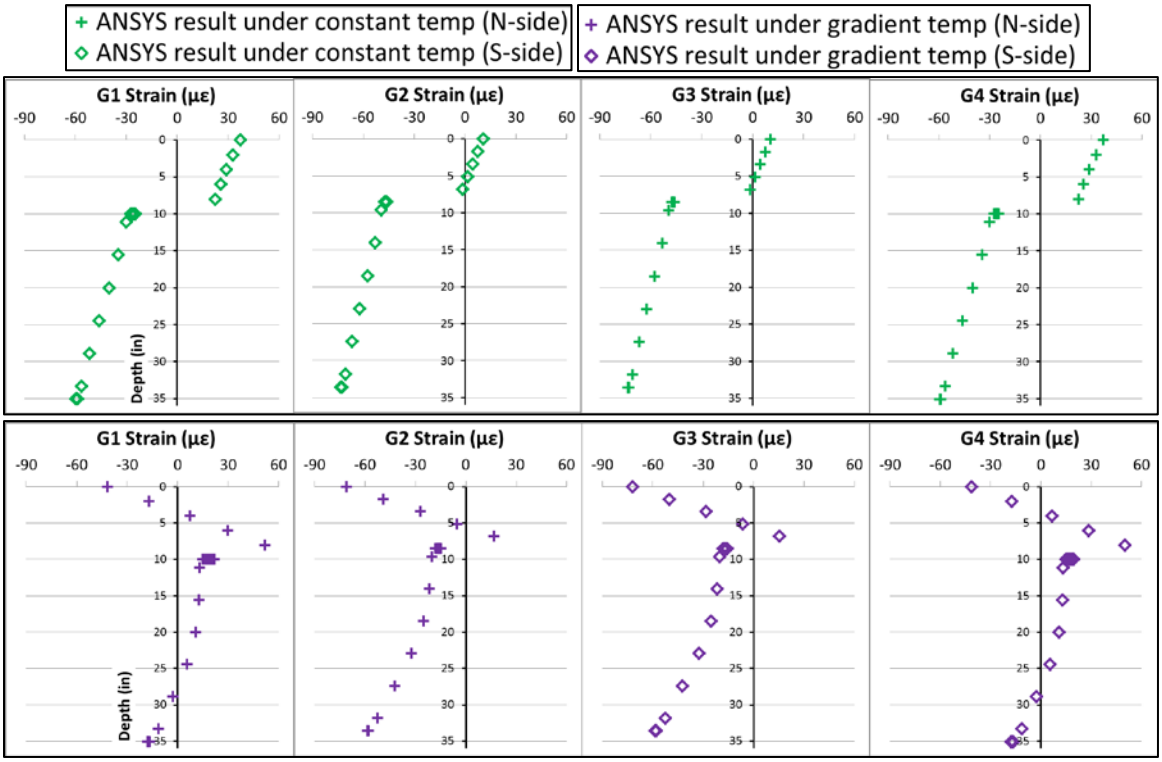

Figure 5-14 ANSYS strain profile results under different thermal loadings

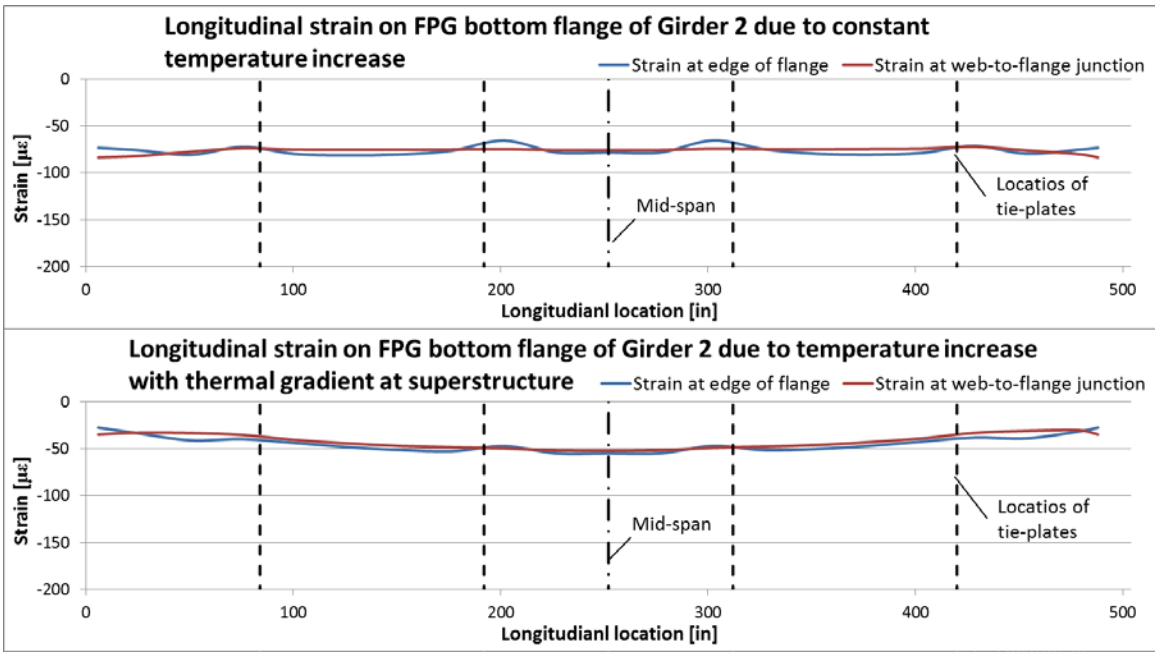

Figure 5-15 Longitudinal strain on FPG bottom flange of Girder 2 due to thermal loading

CHAPTER 6
LONG TERM MONITORING

Long term monitoring is also being performed on this steel FPG integral abutment bridge. Readings of gauges are obtained every two hours starting after the completion of the live load test, two years of data were obtained in total from 11/21/2011 to 12/03/2013. These data can be used to analyze seasonal behavior of the bridge. All data is referenced to the initialization of the data acquisition for long term modeling. Therefore these results do not include construction load effects.

6.1 Bridge temperature

Variation of ambient temperatures at the bridge site can be seen in Figure 6-1. The site temperature was estimated by taking the average temperature of gauges that were not expected to experience temperature fluctuations due to exposure to direct sunlight. The gauges used for ambient temperature estimation are listed in Table 6-1.

Table 6-1 Gauges Used for Temperature Calculation

Gauge ID	Gauge Location
TM101	Center of west abutment, top
TM102	Center of west abutment, bottom
TM103	Center of east abutment, top
TM104	Center of east abutment, bottom

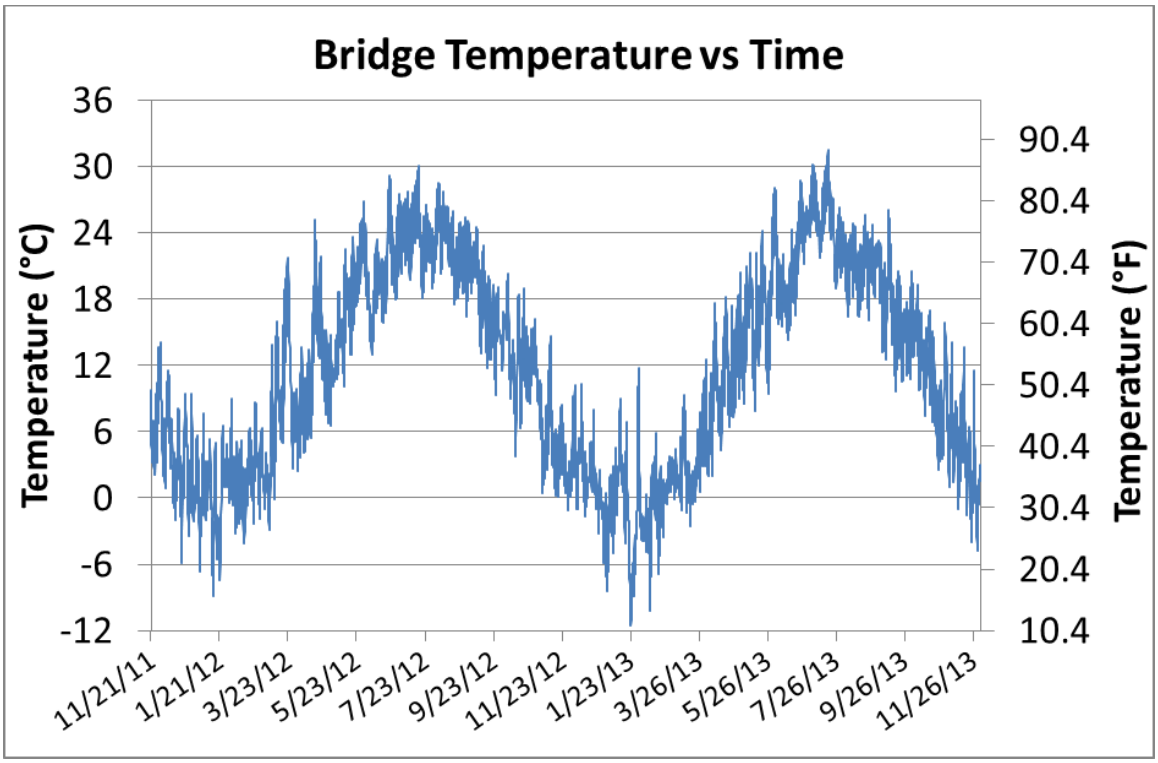

Figure 6-1 Bridge temperature

6.2 Concrete strains

6.2.1 Concrete longitudinal strains

Concrete longitudinal strains in the precast decks and closure pours at mid-span are shown in Figure 6-5 to Figure 6-8. Picture of precast deck embedded longitudinal strain gauge is shown in Figure 6-2 and picture of closure pour embedded longitudinal strain gauge is shown in Figure 6-4. The maximum and minimum longitudinal strains (with positive value indicates tension and negative value indicates compression or shrinkage) in the precast concrete slabs are 338.8 με and -147.2 με. The maximum and minimum longitudinal strains in the closure pour concrete are 25.5 με and -142.5 με. It was found that the south/interior edge gauges in girders 1 and 2 (SG105, SG110) have larger strain than other gauges in the same

girder and are not following the seasonal temperatures. Since these two gauges were located next to the cast in place closure pours, the abnormal readings indicate cracks have likely relieved shrinkage strains induced from the closure pour concrete. The divergence for these two gauges initiated in early Spring of 2012. Most other gauges show a drift towards contraction, which is likely due to concrete shrinkage. It is necessary to note that precast decks were finished on 8/12/2011 and 8/23/2011 whereas closure pours were finished about 2 months later on 10/25/2011, and long term data are recorded after construction and load test on 11/21/2011. Since data are only shown post-construction the reported shrinkage would be larger in the cast in place closure pours than in the precast decks. The strain readings of precast deck and closure pour before the record of long term data are listed in Table 6-2, note that these readings include thermal strain induced after the cast-in-place upper abutment were finished on 10/25/2011. Besides, the readings of Girder 3 are not available since the initial cast strain readings of the girder are missing. From Table 6-2 observed that most of the strain readings in the precast deck are smaller (more negative) than that of the closure pour, possibly confirms that the shrinkage in the precast deck is larger than that of the closure pour. On the other hand, the two gauges (SG120, SG101), which show response most directly related to seasonal temperatures, are at the exterior edges of the structure.

Table 6-2 Concrete strain readings of precast deck and closure pour before the record of long term data at mid-span

Precast Deck Strain [με]	G1			G2			G4		
	SG101	SG102	SG105	SG106	SG109	SG110	SG116	SG119	SG120
	-140.55	-93.40	-58.02	-11.68	-42.91	0.06	-121.06	-136.78	-190.55
Closure Pour Strain [με]	CP1			CP2			CP3		
	SG131			SG134			SG135		
	122.18			-36.05			-31.12		

Concrete longitudinal strains at quarter-span are shown in Figure 6-9 and Figure 6-10. The maximum and minimum longitudinal strains in the precast concrete slabs are 171.5 με and -107.6 με. The maximum and minimum longitudinal strains in the closure pour concrete are 430.8 με and -115.0με. The strain reading of gauge in closure pour 1 (SG121) shows consistent shrinkage strain similar to gauges in closure pour at mid-span. However, the strain reading of gauge in closure pour 2 (SG138) is much larger than all other concrete longitudinal gauges and the reason for this is likely due to cracks are formed near the gauge. The strain readings of precast deck and closure pour before the record of long term data are listed in Table 6-3. Similar to mid-span, strain readings in the precast deck are smaller (more negative) than that of the closure pour, confirms that the shrinkage in the precast deck is larger than that of the closure pour. Besides, the positive (or tensile) reading is found at the gauge SG138 on CP2, this indicates that the cracks near the gauge mentioned above is possibly formed before record of long term data (likely during live load test).

Table 6-3 Concrete strain readings of precast deck and closure pour before the record of long term data at quarter-span

Precast Deck Strain [με]			Closure Pour Strain [με]	
G4			CP2	CP3
SG116	SG119	SG120	SG138	SG139
-121.06	-136.78	-190.55	131.11	-12.86

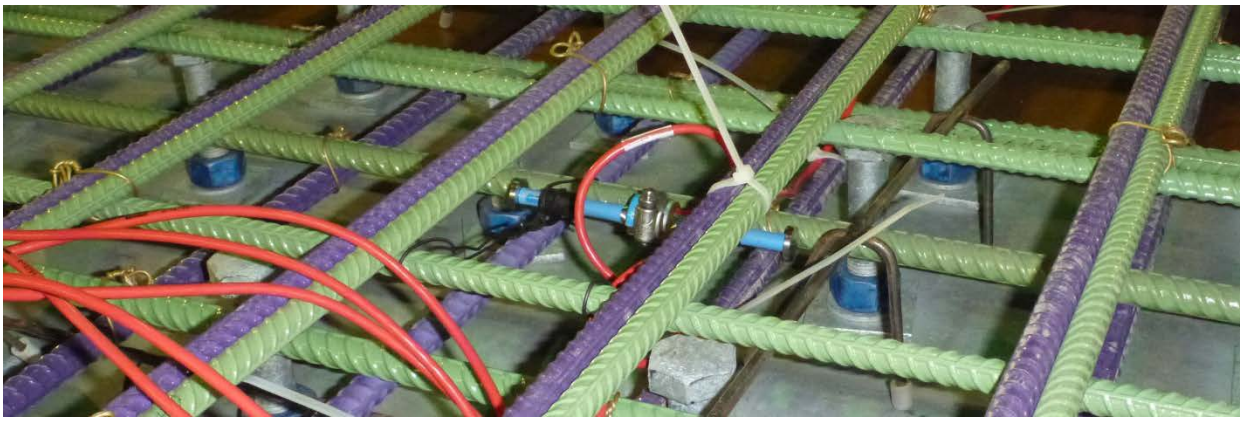

Figure 6-2 Precast deck embedded concrete longitudinal strain gauges

Figure 6-3 Precast deck embedded concrete transverse strain gauges

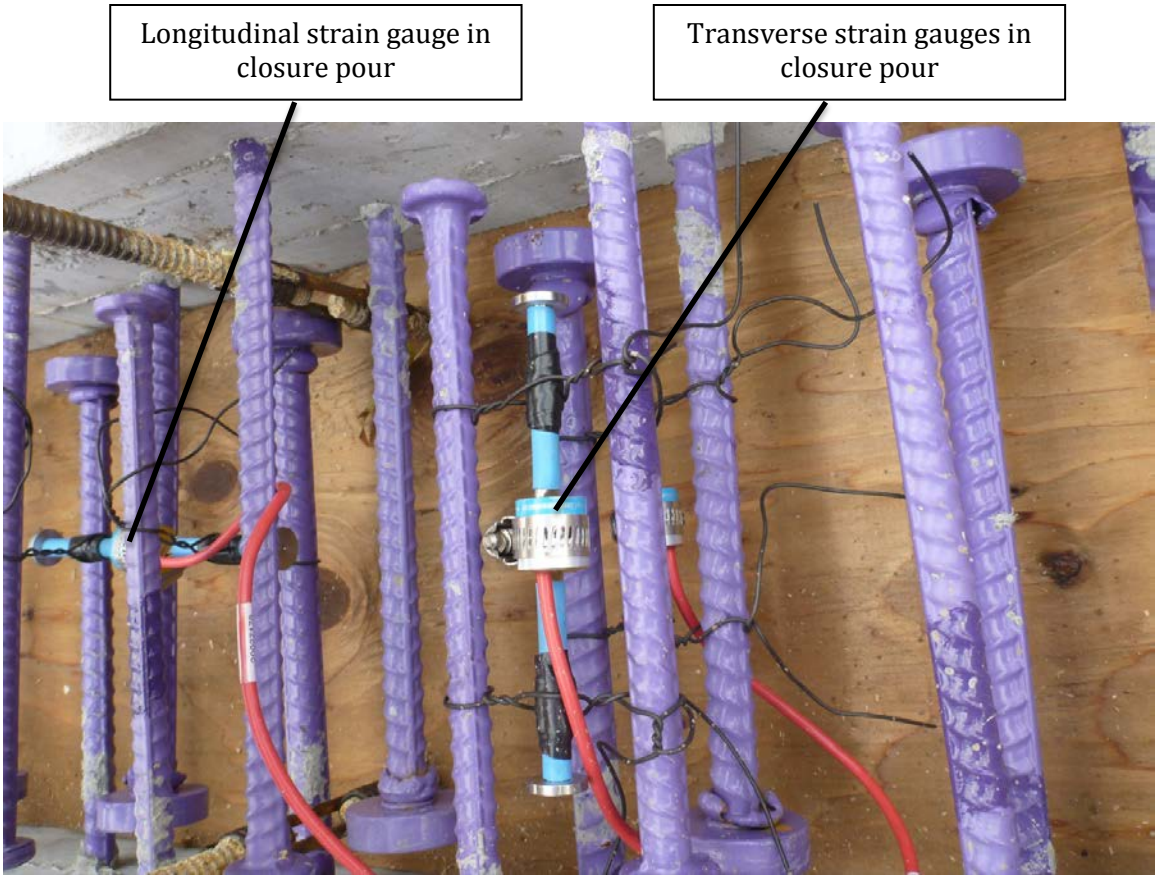

Figure 6-4 Closure pour embedded concrete longitudinal and transverse strain gauges

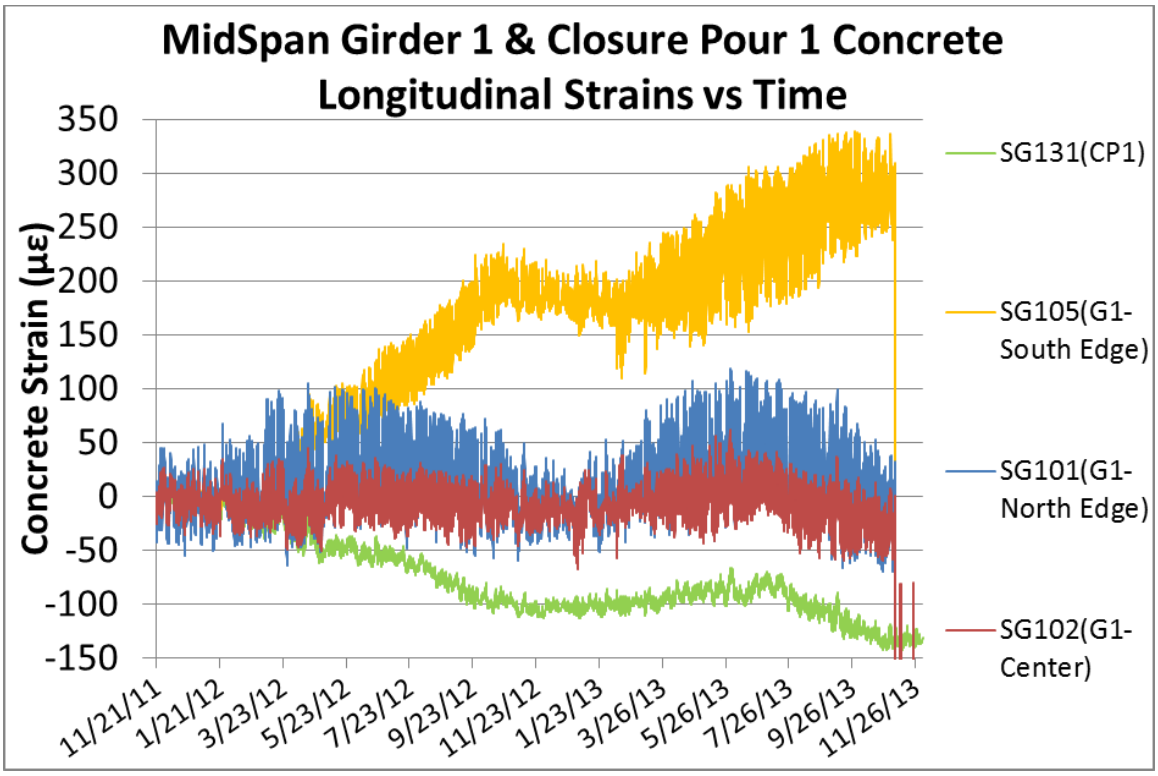

Figure 6-5 Girder Concrete Longitudinal Strains at Mid-span

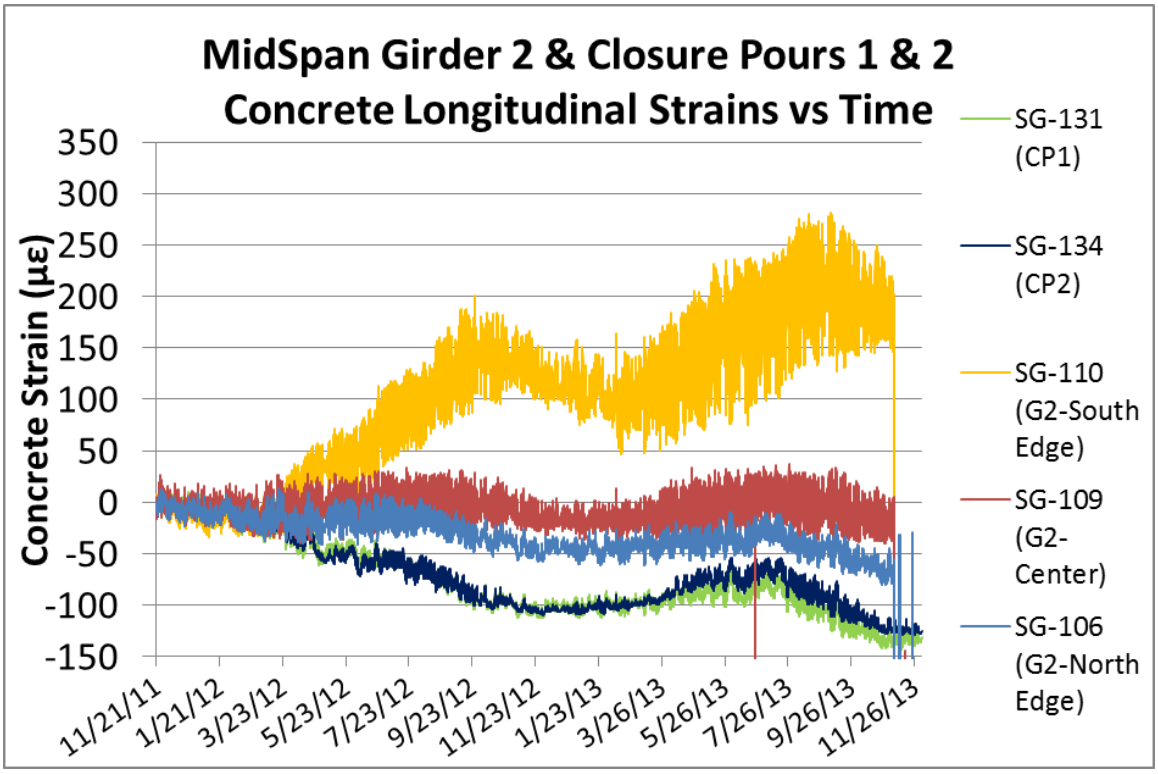

Figure 6-6 Girder 2 Concrete Longitudinal Strains at Mid-span

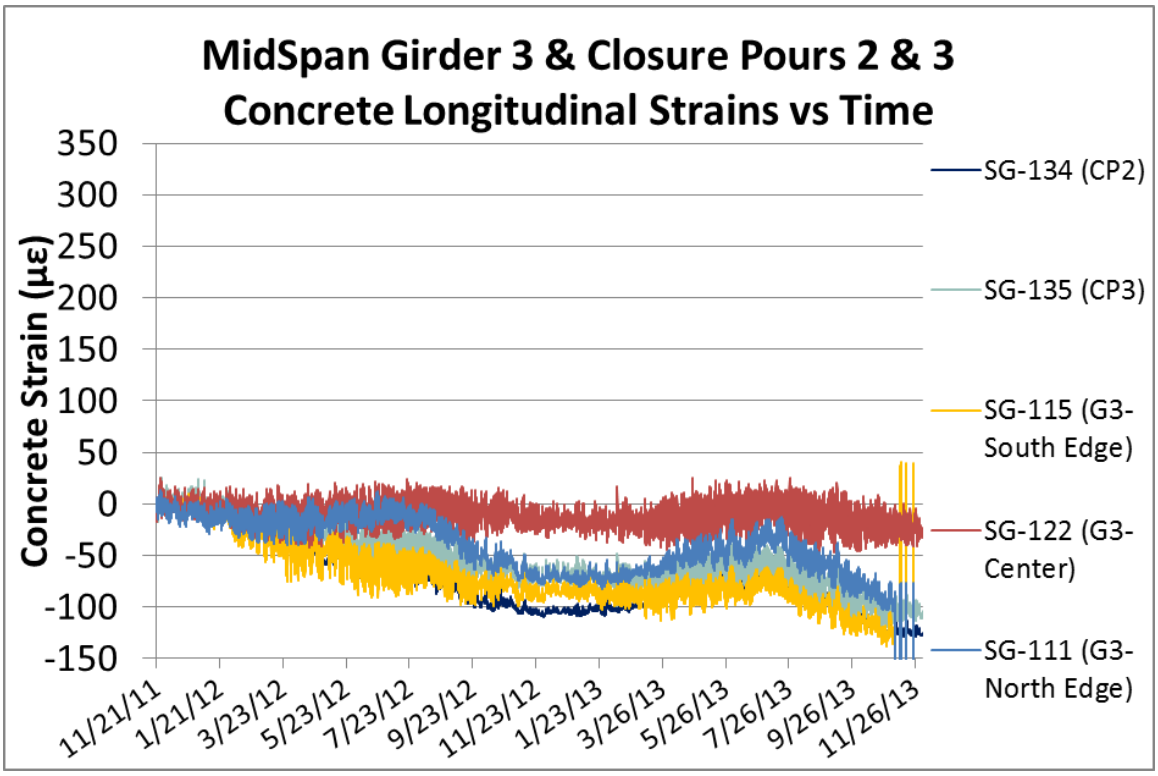

Figure 6-7 Girder 3 Concrete Longitudinal Strains at Mid-span

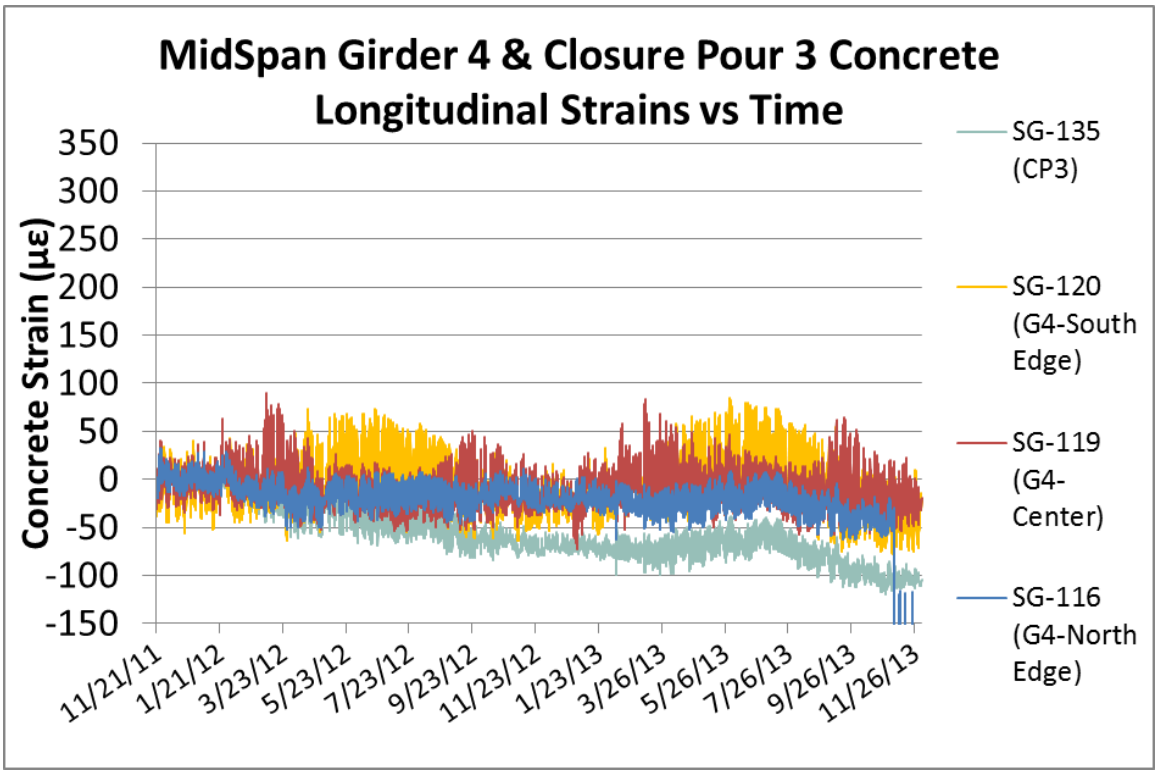

Figure 6-8 Girder 4 Concrete Longitudinal Strains at Mid-span

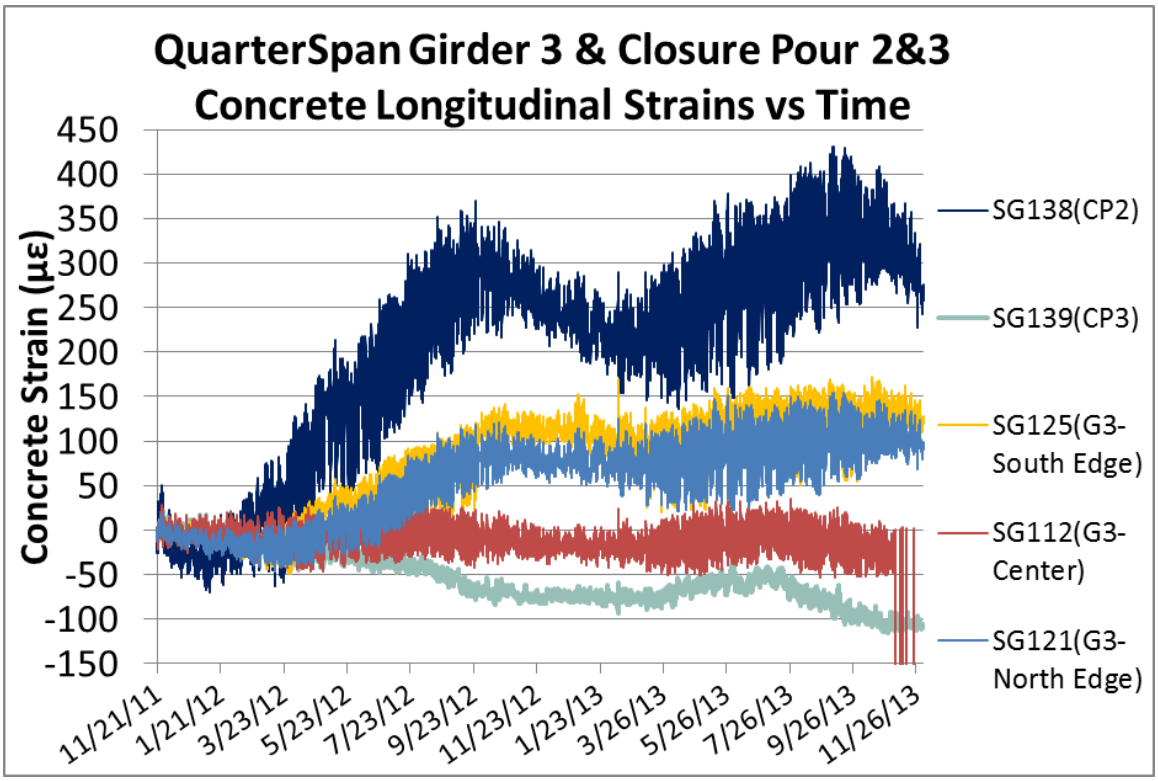

Figure 6-9 Girder 3 Concrete Longitudinal Strains at Quarter-Span

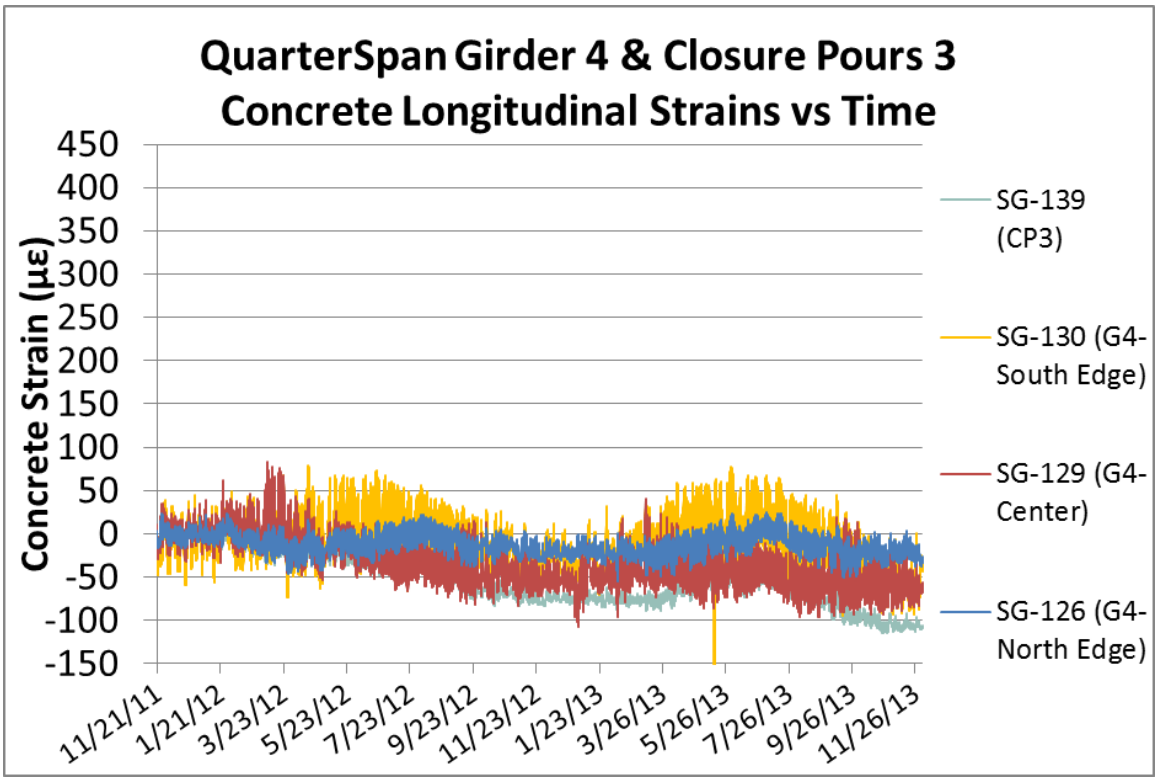

Figure 6-10 Girder 4 Concrete Longitudinal Strains at Quarter-Span

6.2.2 **Concrete transverse strains**

Concrete transverse strains at mid-span are shown in Figure 6-11 and Figure 6-12 for the precast slab and closure pours, respectively (with positive value indicating tension and negative value indicating compression or shrinkage). A picture of a transverse strain gauge embedded in the precast deck is shown in Figure 6-3 and a picture of a transverse strain gauge in the closure pour embedded is shown in Figure 6-4. The maximum and minimum transverse strains in the precast concrete slabs are 193.9 με and -134.4 με. The maximum and minimum transverse strains in the closure pour concrete are 29.2 με and -138.3 με. Concrete transverse strains at quarter-span are shown in Figure 6-13 and Figure 6-14 for the precast slab and closure pours, respectively. The maximum and minimum transverse strains in the precast concrete slabs are 48.3 με and -126.9 με. The maximum and minimum transverse strains in the closure pour concrete are 25.9 με and -139.0 με. Transverse strains appear to be influenced more from ambient temperature than do longitudinal strains, though have shown a drift towards compressive strains over time (likely due to a combination of shrinkage and bridge movements). Transverse strain values are similar at mid-span and quarter span locations and all indicate shrinkage with time.

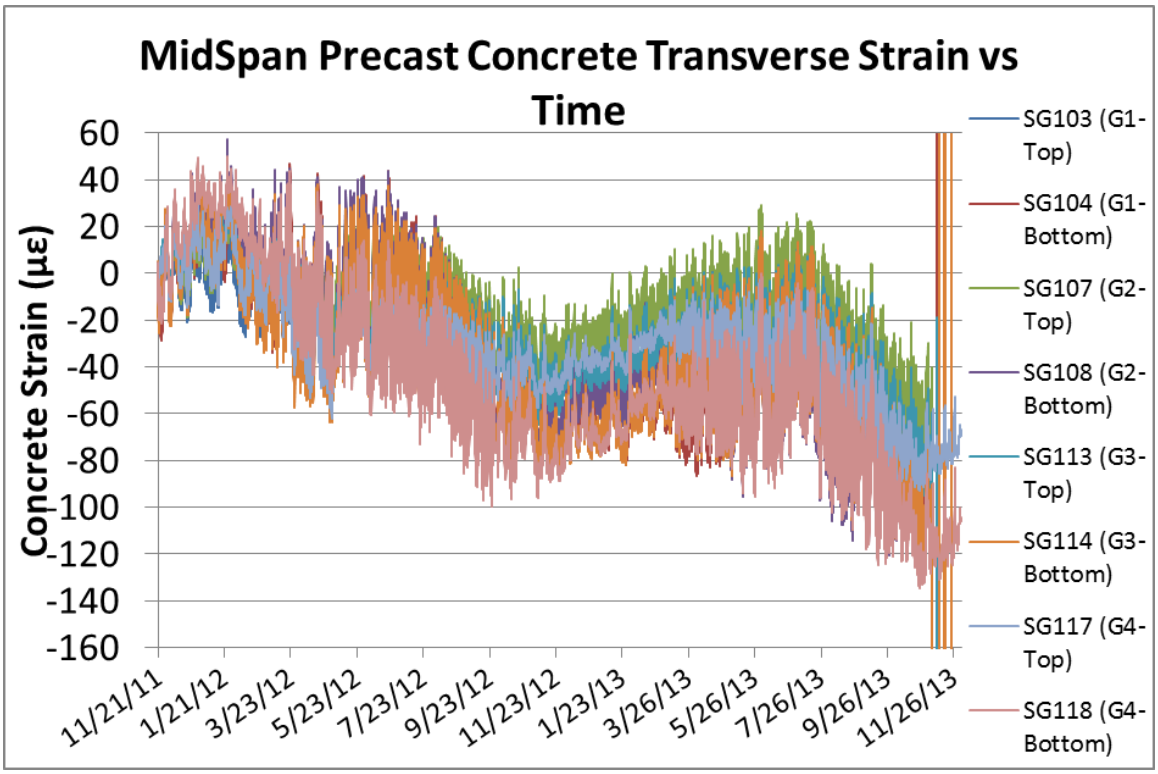

Figure 6-11 Precast Concrete Transverse Strains at Mid-span

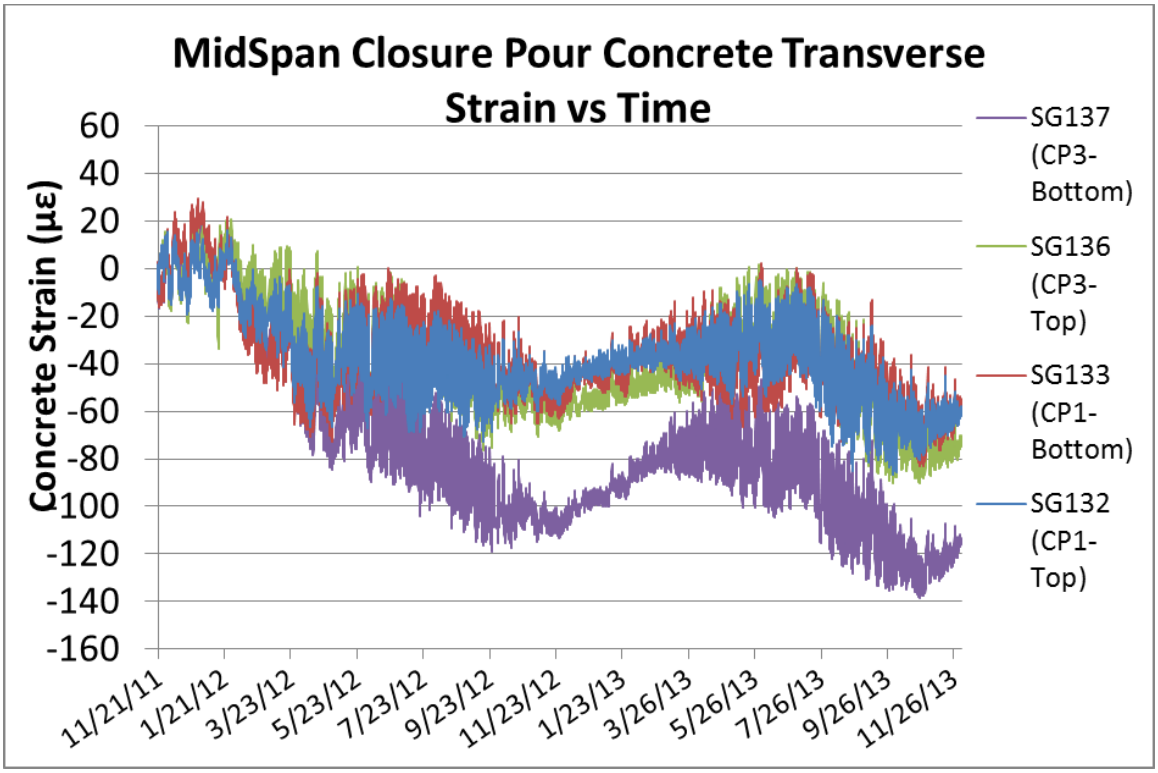

Figure 6-12 Closure Pour Concrete Transverse Strains at Mid-span

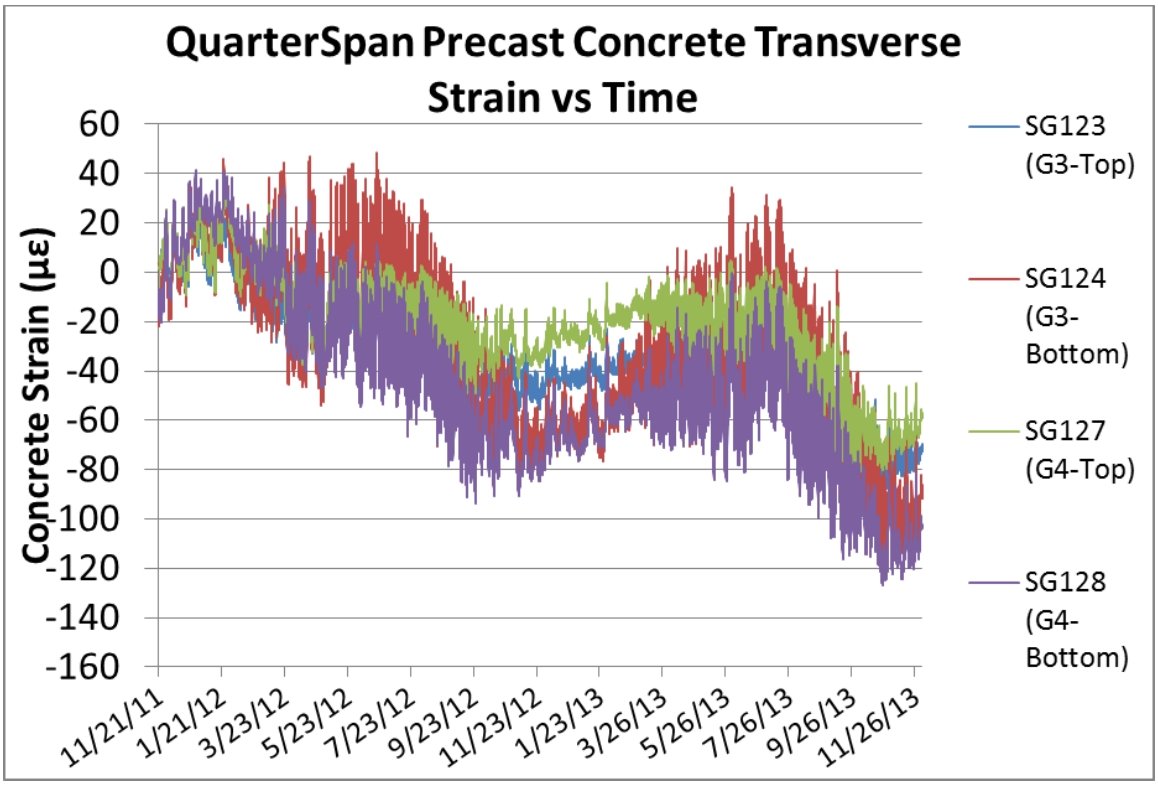

Figure 6-13 Precast Concrete Transverse Strains at Quarter-Span

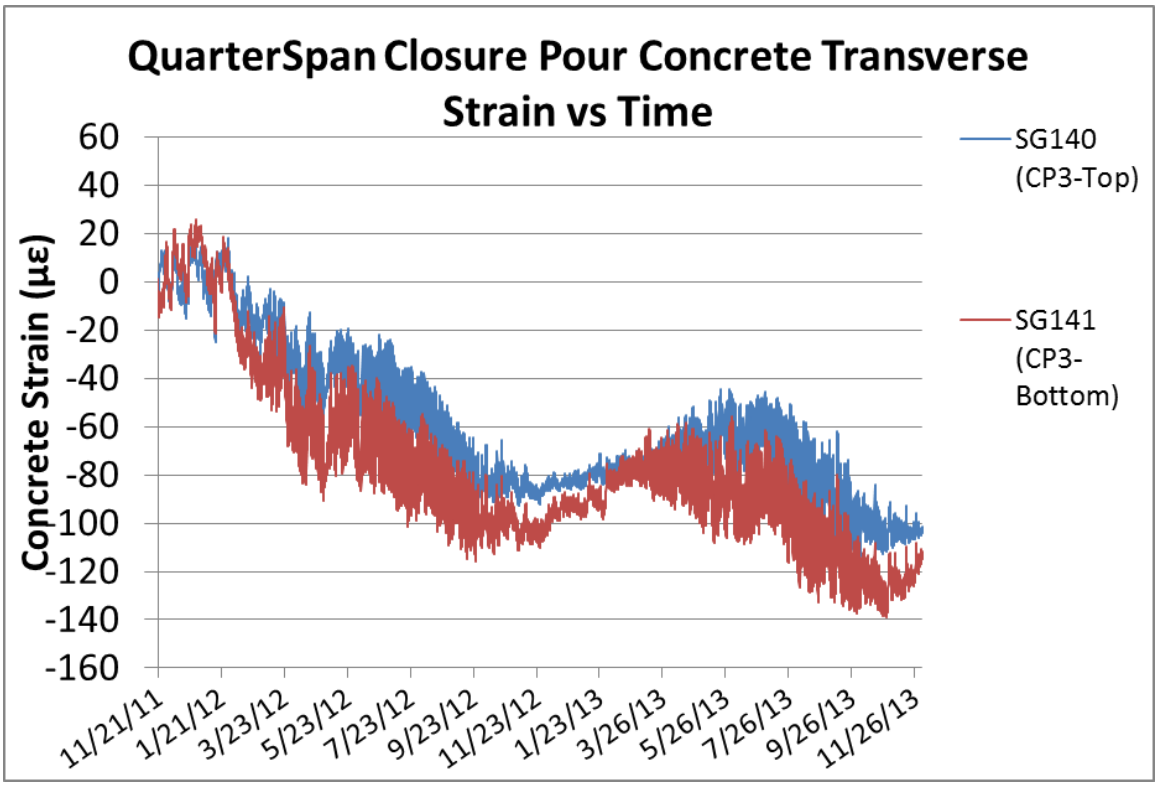

Figure 6-14 Closure Pour Concrete Transverse Strains at Quarter-Span

6.3 Folded Plate Girder steel strains

FPG bottom flange steel strains at mid-span are shown in Figure 6-18 to Figure 6-21 (with positive values indicating tension and negative values indicating compression). A picture of FPG longitudinal strain gauges is shown in Figure 6-15. The maximum and minimum longitudinal strains in the bottom flange of the FPG section are 104.3 με and -107.0 με. These correspond to a maximum tensile stress of 3.0 ksi [20.7 MPa] and a maximum compressive stress of 3.1 ksi [21.4 MPa]. FPG bottom flange steel strains at quarter-span are shown in Figure 6-22 and Figure 6-23. The maximum and minimum longitudinal strains in the bottom flange of the FPG section are 94.1 με and -114.1 με. These correspond to a maximum tensile stress of 2.7 ksi [18.6 MPa] and a maximum compressive stress of 3.3 ksi [22.8 MPa]. The difference in bottom flange strain readings (average readings between north and south side flange are used) between mid-span and quarter-span is plotted Figure 6-24, with positive reading indicates mid-span strain is larger than that in quarter-span. The difference in Girder 3 ranges from -14.6 με to 18.6 με while that in Girder 4 ranges from -8.3 με to 38.5 με. The difference in Girder 4 start to diverge from that of the Girder 3 during spring around April 2012, this correspond to a spike in temperature and the start of the bottom flange tie-plates restraining the bottom flange deformation which is discussed in the next paragraph. In general bottom flange stresses were similar between the quarter span and mid-span readings, indicating that thermal changes introduce a constant moment along the bridge span as would be expected in an integral abutment structure where thermal changes result in a moment constraint at the abutments. However, strains in the two

flanges differ somewhat at the quarter span location, and gauges (SG169 and SG173) which located nearer to closure pour 3 show smaller reading compare to gauges (SG168 and SG 174) which located farer away from closure pour 3. This indicates that the difference between the two flanges is perhaps due to torsion happened at closure pour 3.

Strains in the tie plates on girders 3 and 4 nearest mid-span (5 ft from mid-span) are shown in Figure 6-25, locations of tie-plates are shown in Figure 1-4 and Figure 6-17. Pictures of tie-plate transverse strain gauge and bottom flange transverse displacement transducer are shown in Figure 6-16. The maximum and minimum transverse strains in the tie plate of the FPG bottom flange are 138.0 $\mu\varepsilon$ and -41.2 $\mu\varepsilon$. These correspond to a maximum tensile stress of 4.0 ksi [27.6 MPa] and a maximum compressive stress of 1.2 ksi [8.3 MPa]. All four tie plates appear to have become engaged in restraining the flange deformation in Spring 2012. This corresponds to a spike in temperature and deformation of the bottom flanges in these girders away from each other as shown in Figure 6-26, the locations of bottom flange displacement transducers are shown in Figure 1-10 and Figure 6-17. The maximum and minimum transverse displacements in the bottom flange of the FPG section are 0.0126 in [0.032 cm] and -0.005 in [-0.013 cm] with positive values indicating widening at the bottom of the girder.

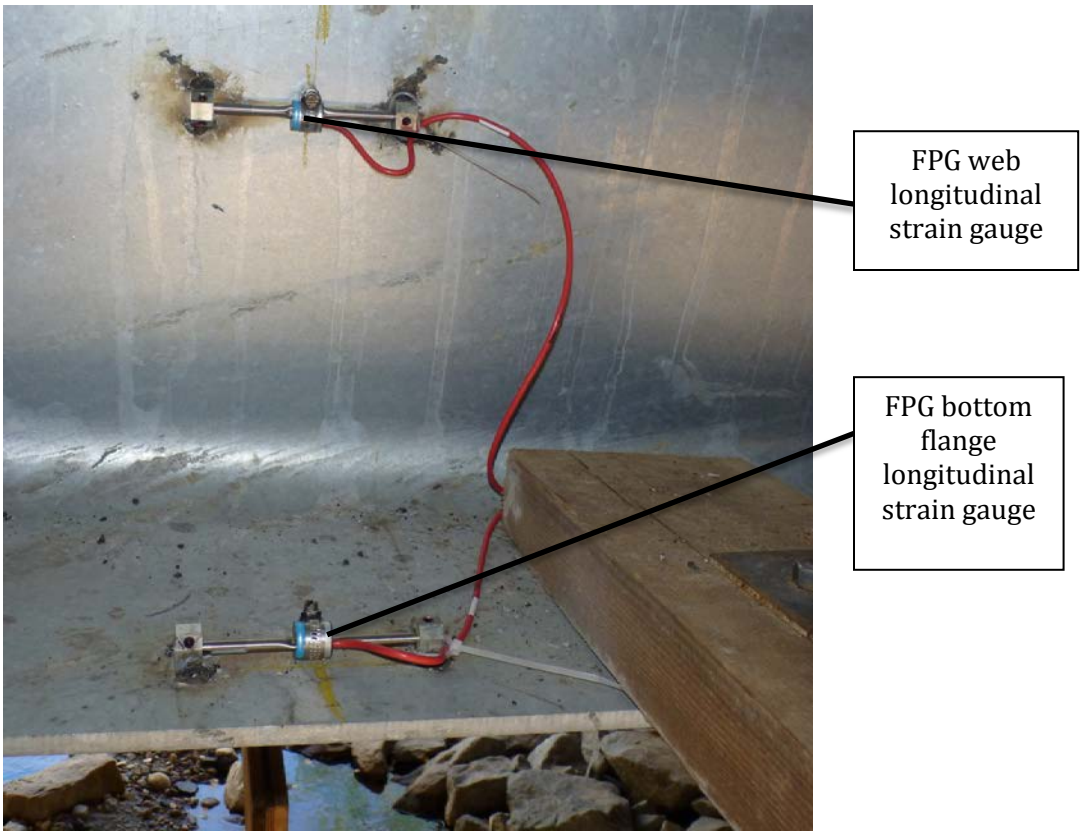

Figure 6-15 Steel FPG longitudinal strain gauges

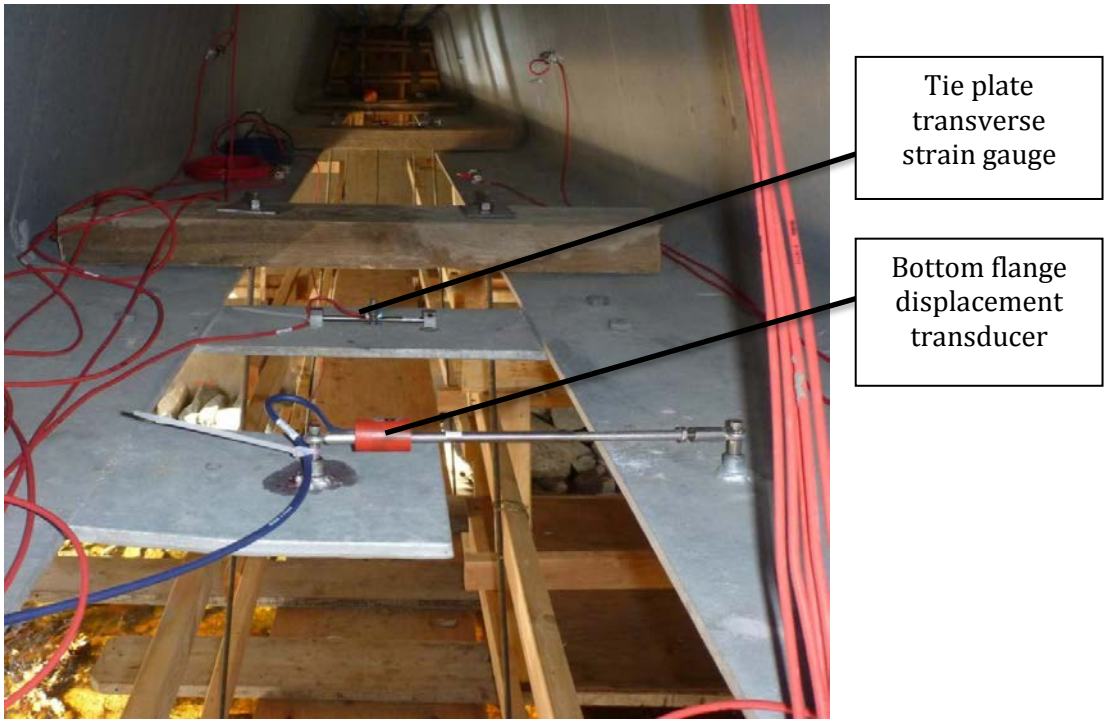

Figure 6-16 FPG bottom flange tie-plate transverse strain gauge and displacement transducer on Girder 3

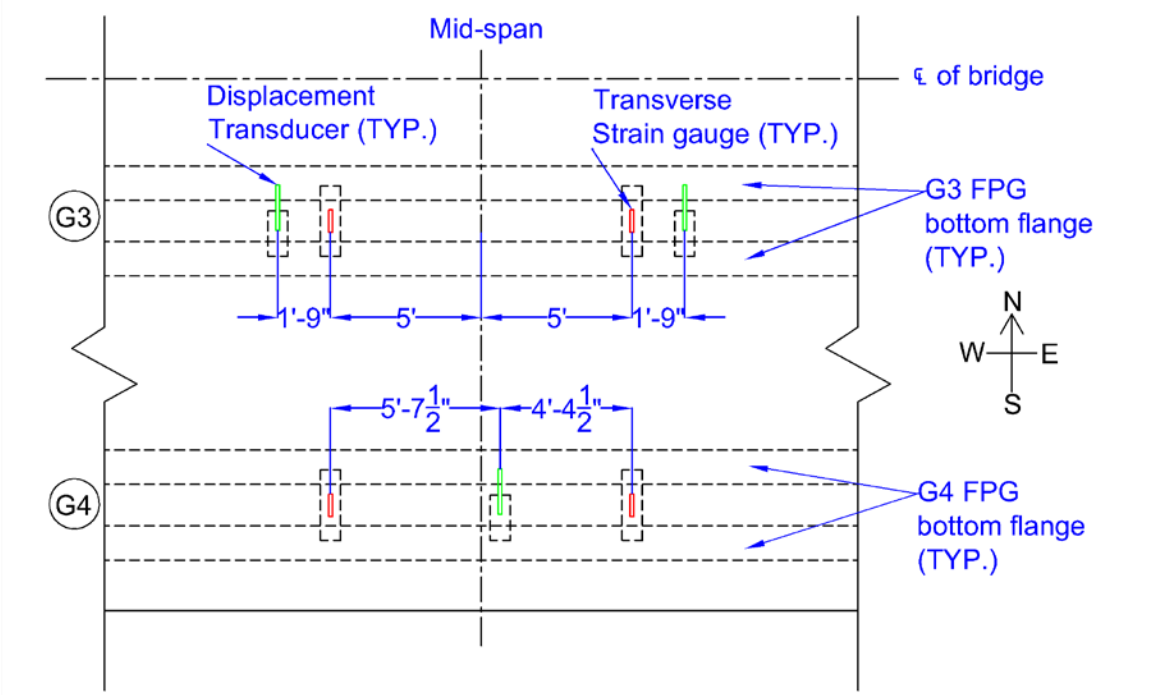

Figure 6-17 Plan view of bridge showing locations of transverse strain gauges on tie-plates and displacement transducer between bottom flange

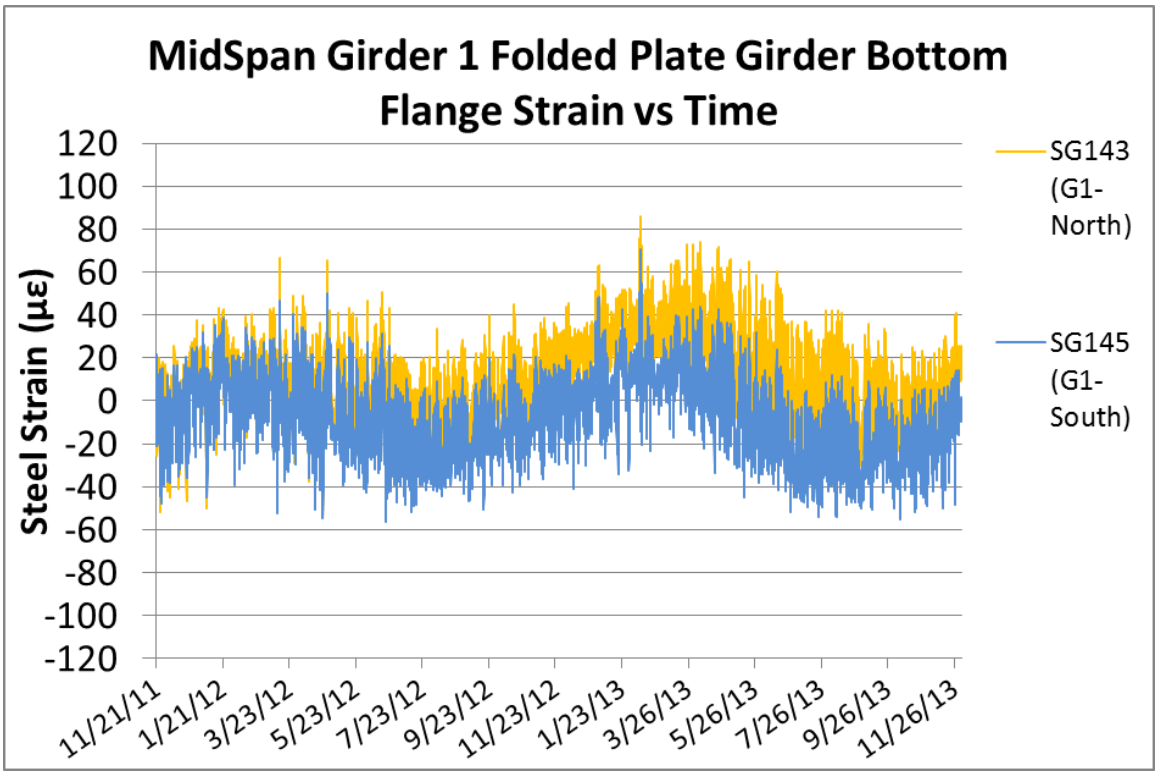

Figure 6-18 Girder 1 FPG Bottom Flange Strain at Mid-span

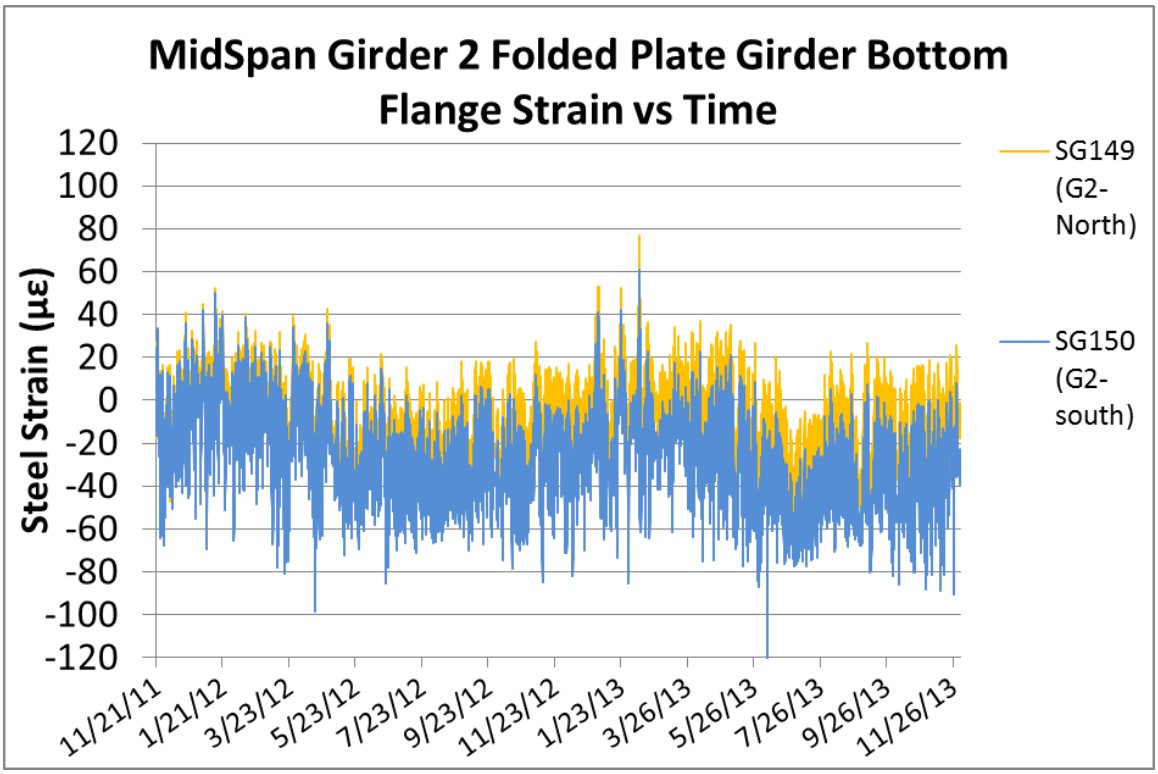

Figure 6-19 Girder 2 FPG Bottom Flange Strain at Mid-span

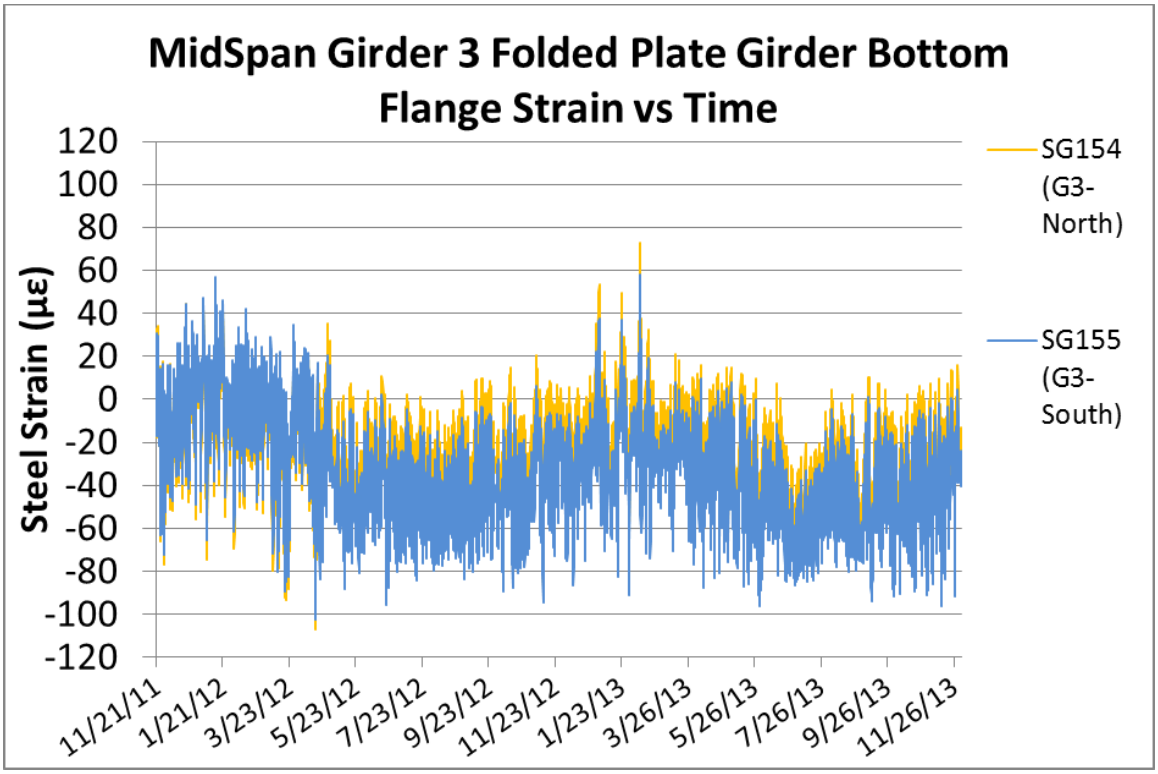

Figure 6-20 Girder 3 FPG Bottom Flange Strain at Mid-span

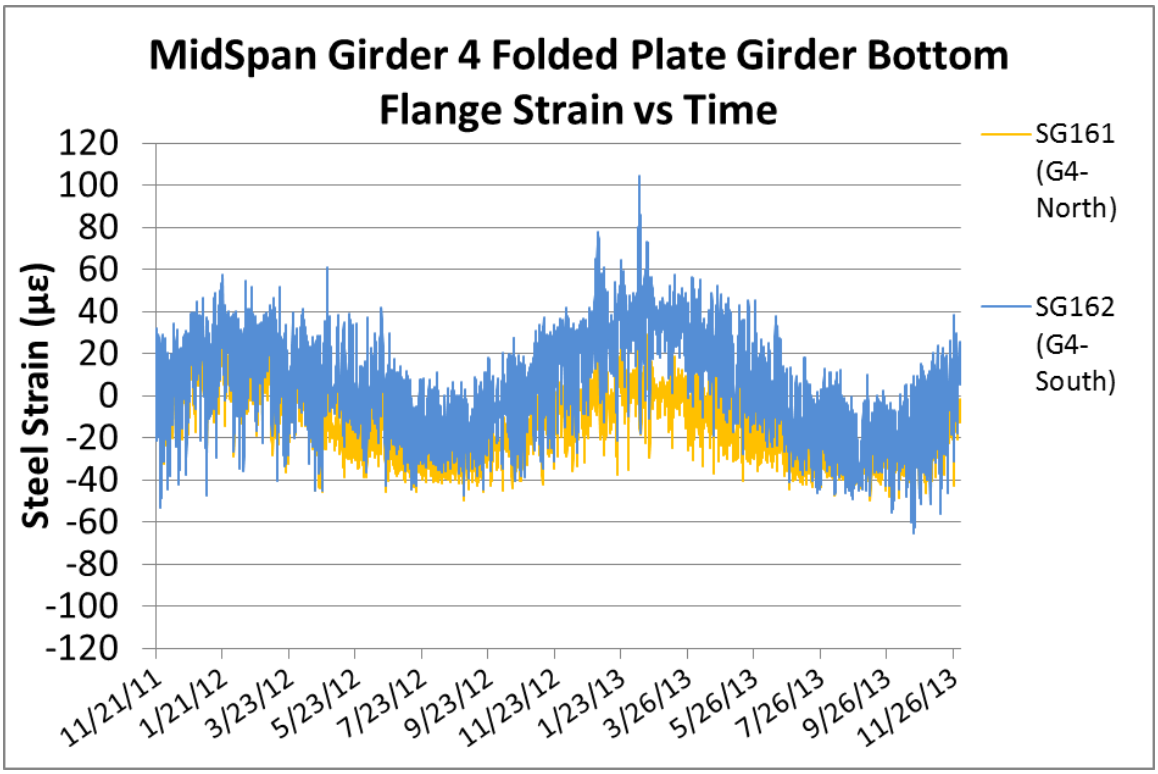

Figure 6-21 Girder 4 FPG Bottom Flange Strain at Mid-span

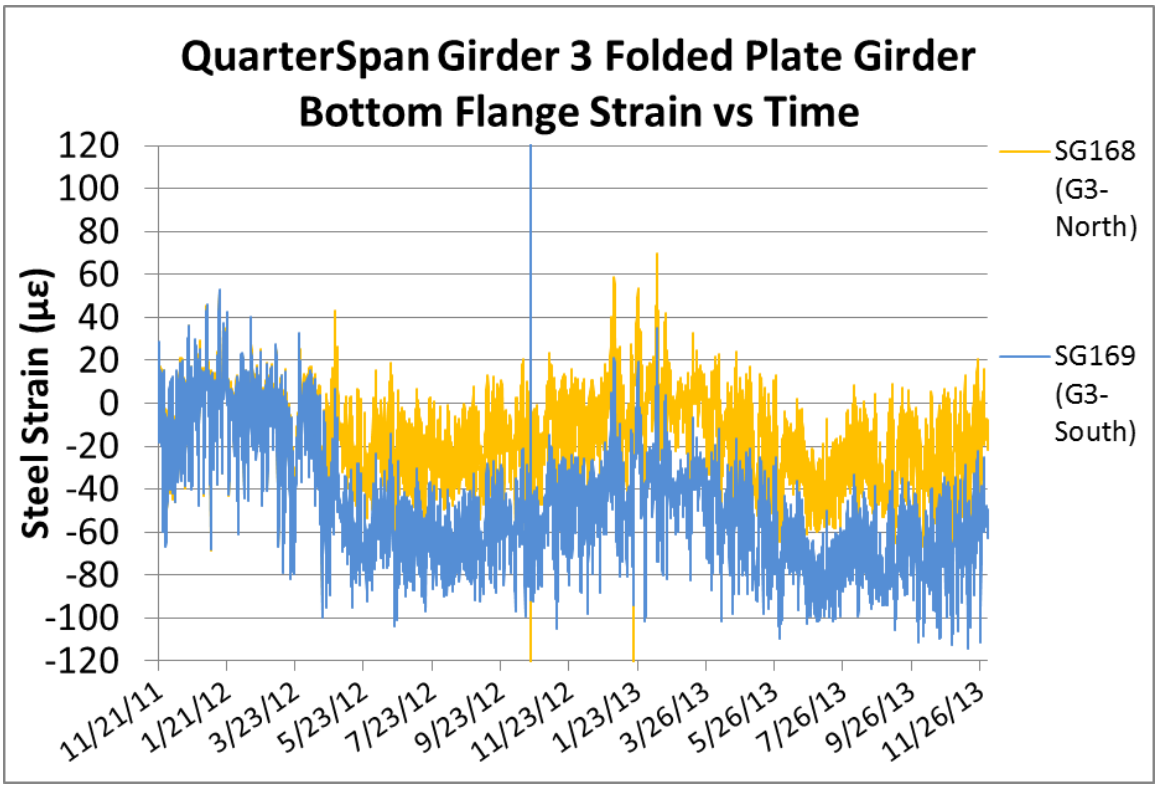

Figure 6-22 Girder 3 FPG Bottom Flange Strain at Quarter-Span

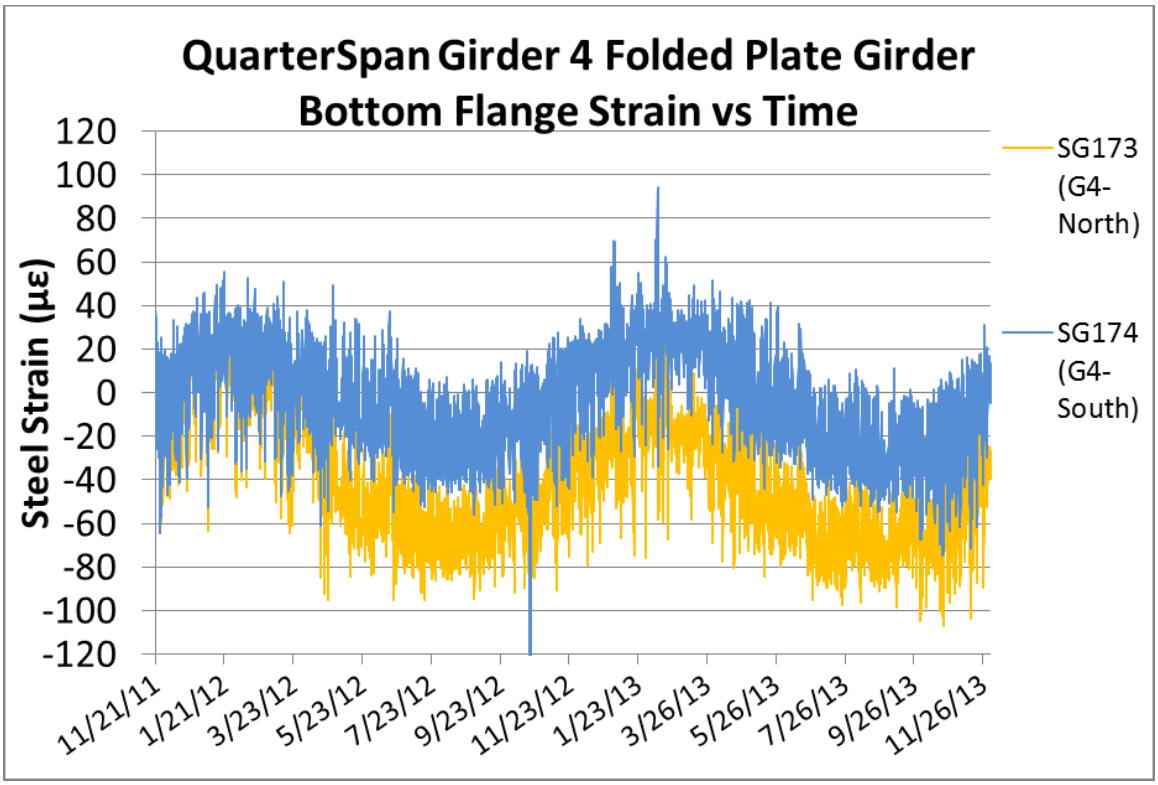

Figure 6-23 Girder 4 FPG Bottom Flange Strain at Quarter-Span

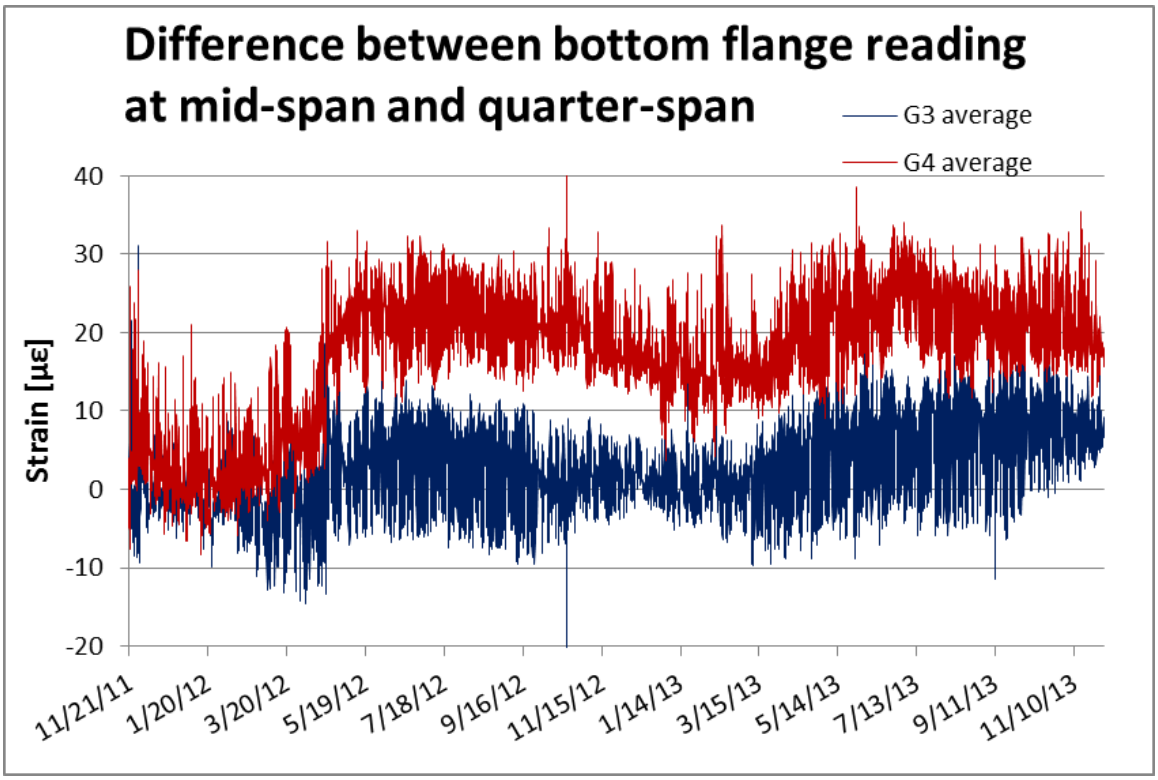

Figure 6-24 Difference between bottom flange reading at mid-span and quarter-span

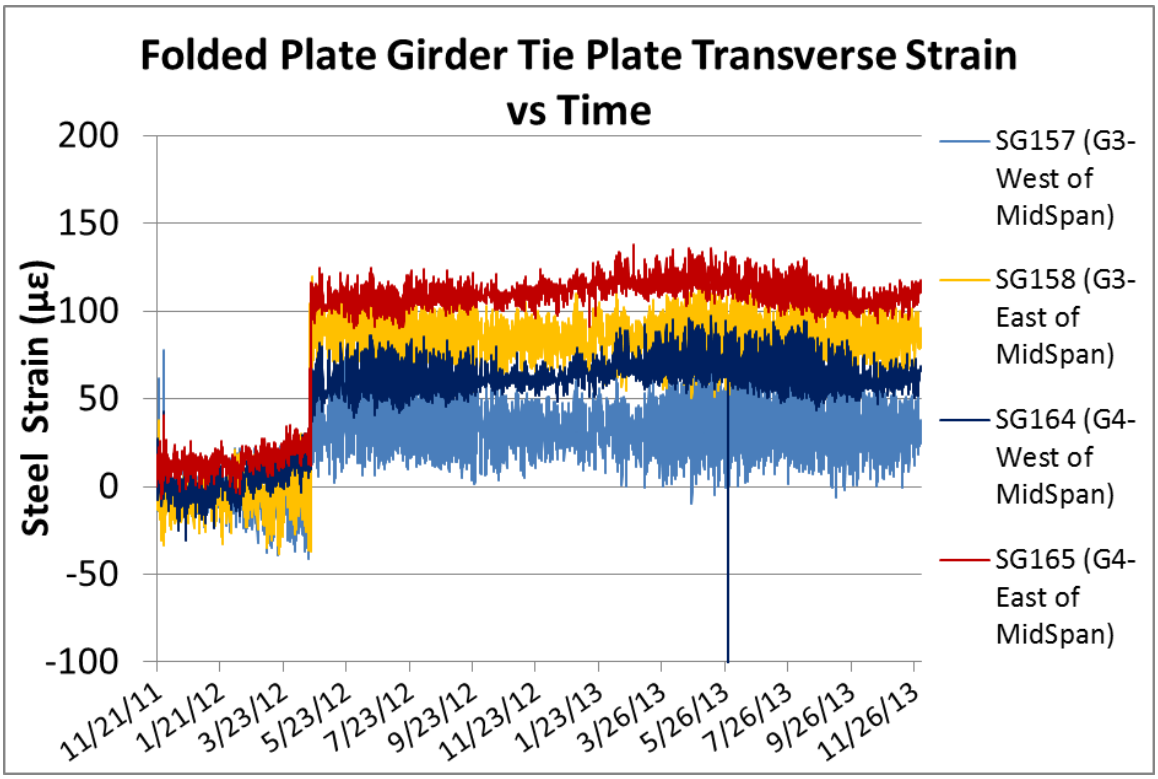

Figure 6-25 FPG Girder Tie Plate Transverse Strain

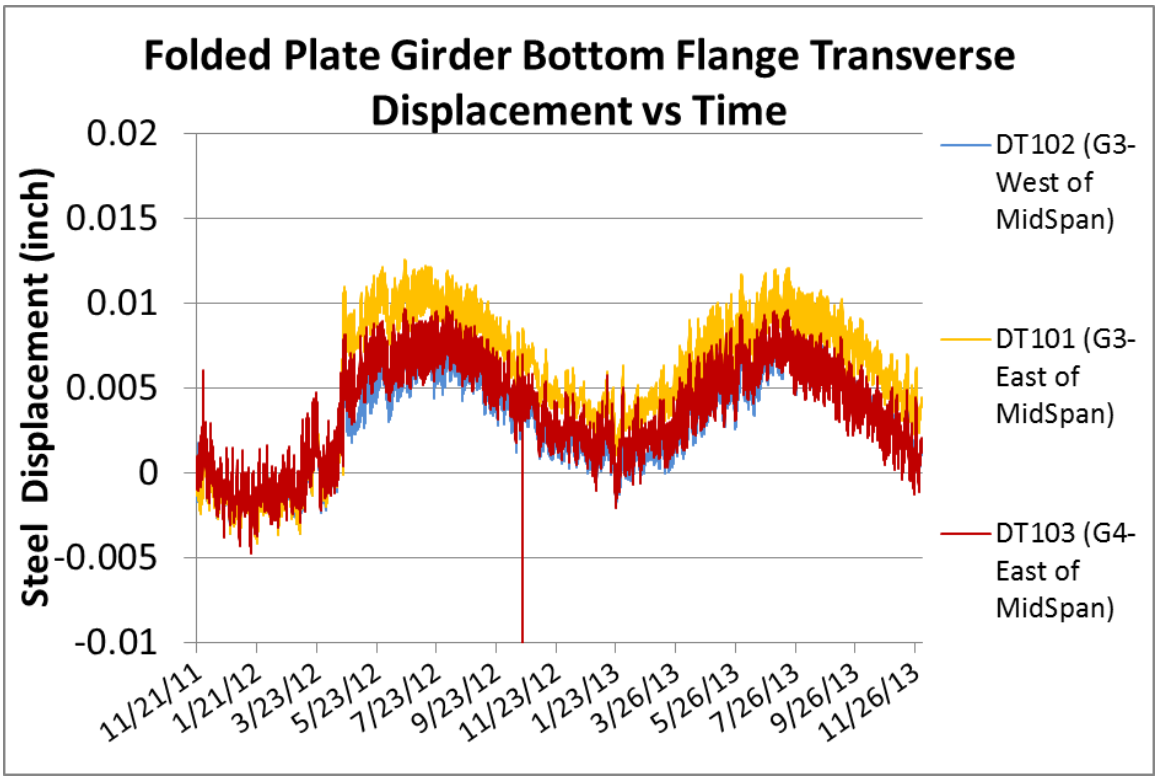

Figure 6-26 FPG Bottom Flange Transverse Displacements

6.4 Bridge global effects

Abutment rotation is shown in Figure 6-29, with positive values indicating a rotation toward the span and negative values a rotation toward the approach. Pictures of the abutments rotation tilt-meter is shown in Figure 6-27. The maximum and minimum abutment rotations are approximately 0.046 degree and -0.13 degree. Rotations of the two abutments are similar with the rotation in the East abutment being larger. The rotations follow the seasonal temperatures with a drift towards negative rotation in the 2nd year. There is a slight discrepancy between top and bottom abutment rotations which may indicate slightly non-uniform behavior across the abutment construction joint.

Transverse displacements of retaining walls at the corners of the abutments are shown in Figure 6-30. Picture of retaining wall transverse displacement transducer is shown in Figure 6-28. Positive values indicate displacement away from the abutments and negative values a displacement toward the abutments. The maximum retaining wall displacement is approximately 0.9 in [2.3 cm]. Greater retaining wall movements are indicated at the East abutment side. In addition, the displacements were larger at the south than North edges of the bridge. This was confirmed by inspection in the field on 16th and 18th of December 2013.

Figure 6-27 Abutment rotation tilt-meter

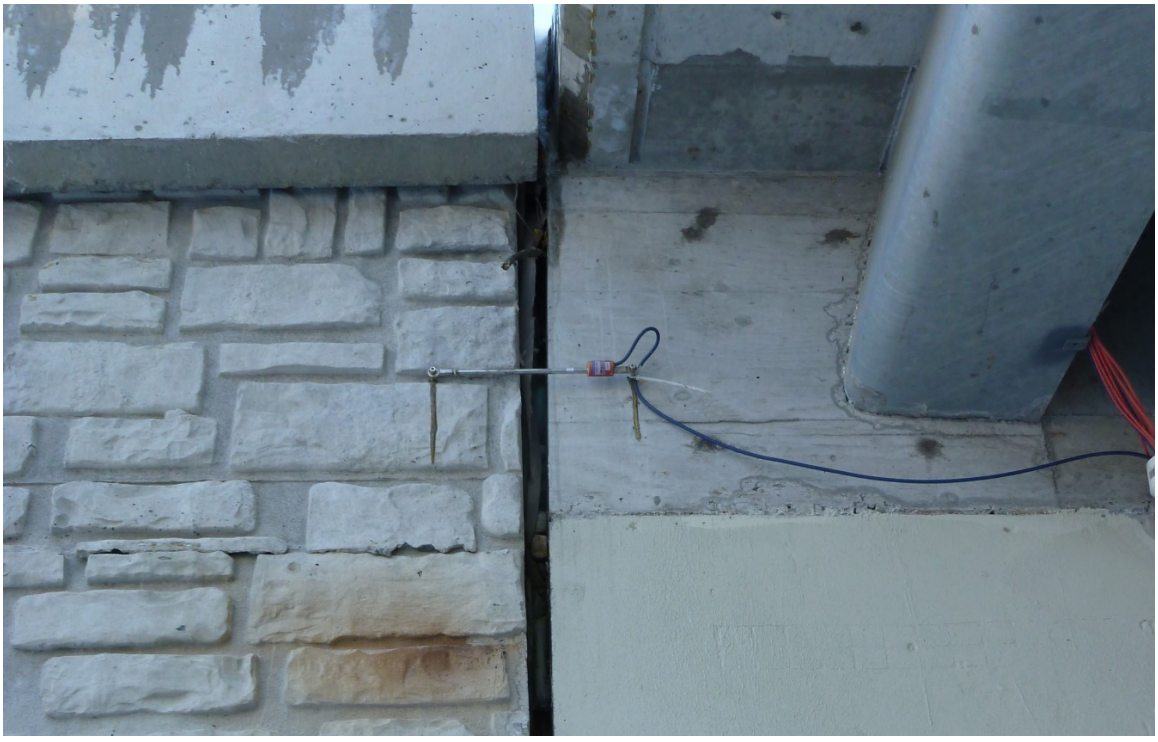

Figure 6-28 Retaining wall transverse displacement transducer

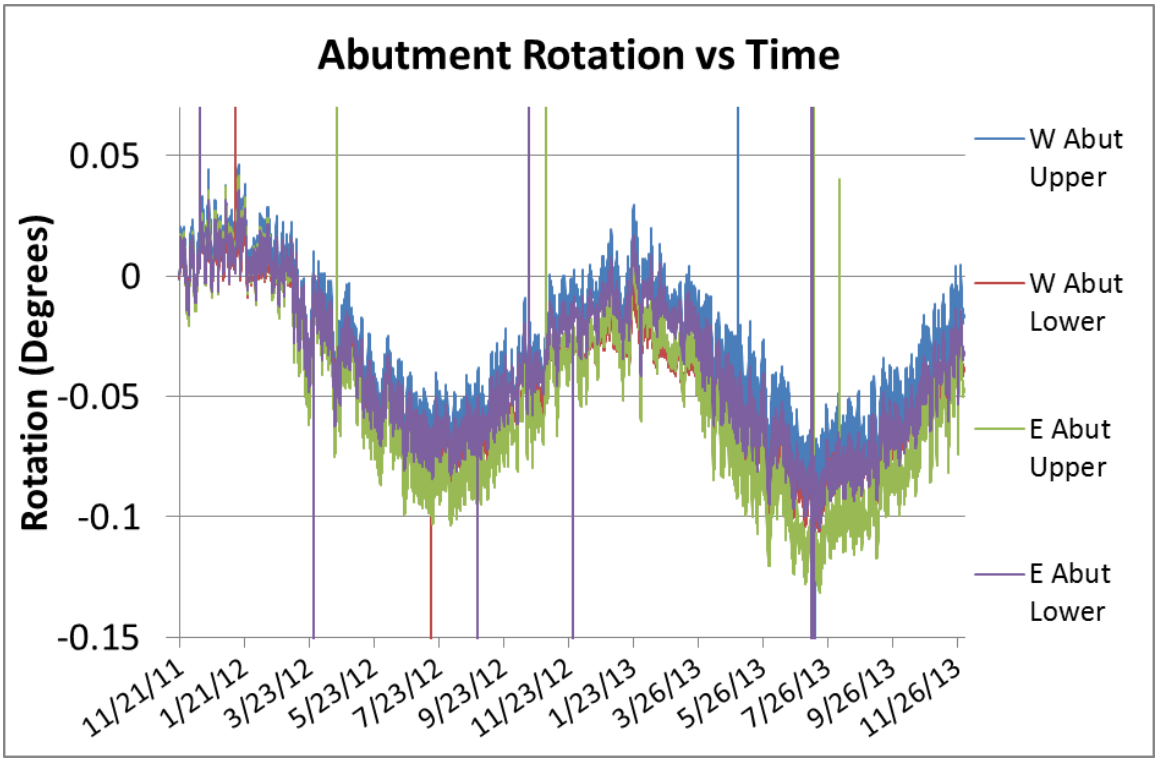

Figure 6-29 Abutment rotations

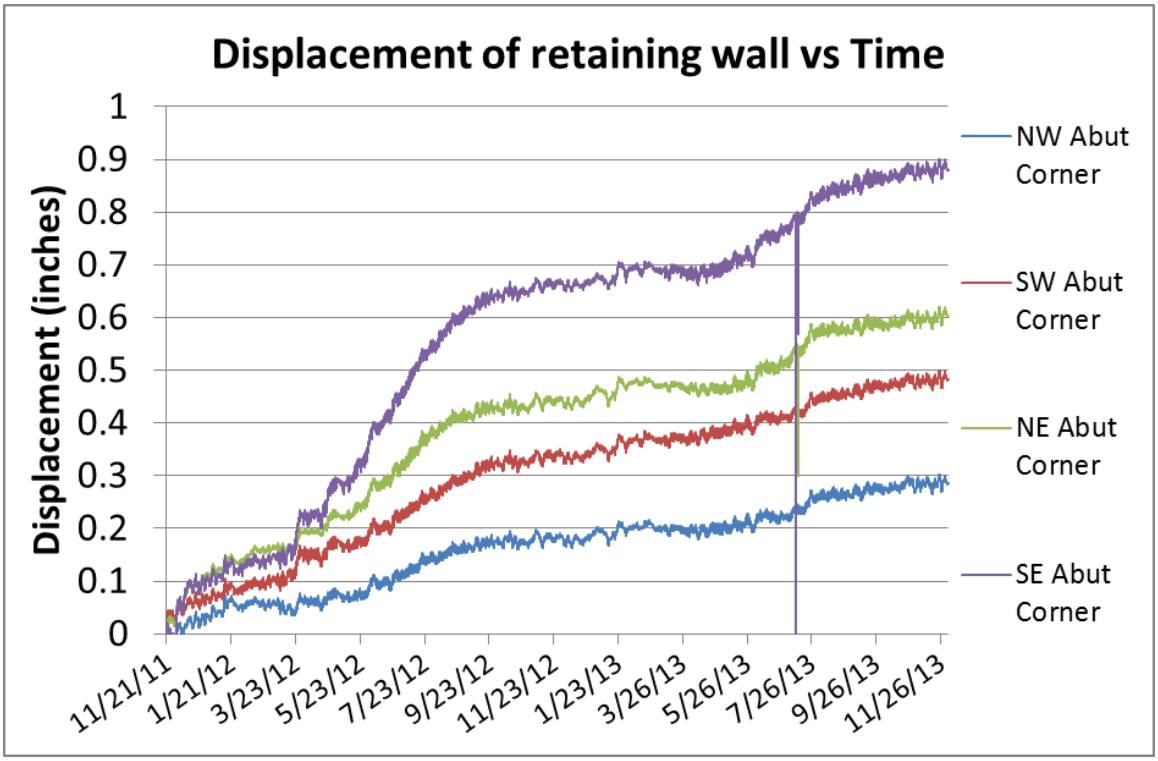

Figure 6-30 Abutment Displacements

6.5 Summary

Long term data have been presented for the Uxbridge Folded Plate Bridge from 11/21/2011 to 12/03/2013. Long term monitoring data includes the overall bridge deformations in terms of abutment rotations, longitudinal and transverse strains in concrete (precast and closure pours) and strains in the steel FPG sections. Overall, a combination of seasonal effects as well as long term shift in readings is apparent which is expected to converge to seasonal effects after the first 2-4 years of cycling.

The total strain at the bottom flange of FPG due to long term thermal loading and self-weight effect in exterior and interior girder are 241 με and 254 με respectively, which are equivalent to 7 ksi [48.3 MPa] and 7.4 ksi [51.0 MPa] respectively. Note that the strain values due to self-weight effect are obtained by hand calculation (no field data is available), while the strain values due to long term thermal loading are from actual field data. The strain values show that currently there are no readings that are outside of expected behavior (no yielding in the steel).

CHAPTER 7
THERMAL BEHAVIOR

In this chapter, the thermal behaviors of the bridge under seasonal temperature are studied. A parametric analysis was performed using a detailed finite element model developed in ANSYS APDL as described in Section 2.3. Thermal values as well as gradients were applied to the model and results of the model were compared to the field long term data.

7.1 Parametric analysis models

In the parametric analysis, several parameters were considered to possibly capture the actual behavior of the bridge. In integral abutment bridges, the longitudinal thermal displacements of the superstructure will cause movements of the abutments, and the backfill soils behind the abutments and the soils at the foundation level surrounding the piles will provide resistance to the movement. Therefore the soil properties in these locations are important parameters for thermal behavior of the bridge. The expect soil type at the bridge site were medium dense sand soil for both the backfill and the pile soil. However, the soil properties can vary due to construction detail and temperature changes. Thus, dense sand soil properties and conditions with no soil resistance at backfill and/or piles were also considered in the parametric analysis. The soil properties considered were listed in Table 7-1.

On the other hand, since the piles were connected to the bottom of the abutments with self-consolidating concrete that injected into the piles sleeve at the

top of the abutments, it was considered that movement during the curing period of the concrete could decrease the fixity of the pile in the concrete and therefore the continuity of the piles to the abutments. From this assumption, a condition with piles pin connected to the abutments was also considered in the parametric analysis.

Last, in thermal analysis, the applied temperatures were considered to be an additional parameter. Actual temperatures of the bridge were obtained from the thermistor of the instrumented gauges. In the superstructure, the temperature of the deck gauges and the steel FPG gauges were looked at separately. Within the FPG gauges, individual gauges at the same level record similar temperature (less than 3°F [1.7°C] different) with the exception of one or two gauges recording a different temperature at certain date (for instance, the far south web gauge SG163 recorded temperature 12°F [6.7°C] higher than average FPG temperature at mid-span at 4 pm on 10th of Feb 2013). Similar consistency was observed in the deck gauges as well. On the other hand, by comparing the gauges at different levels, temperature gradients were found along the depth of the bridge section. During summer, the average temperature at the deck gauges level, which represent approximately the middle level of the deck, was much higher than the average temperature in the steel FPG (about 15°F [8.3°C] higher due to sun radiation). Whereas within the FPG, the average temperature in top flanges was found to be slightly higher (about 5°F [2.8°C] higher) than that in the mid-height web gauges and the bottom flange gauges. During winter, the temperature gradient was much smaller, with the average deck gauges temperatures being about 4°F [2.2°C] lower than the average

steel FPG gauges and the FPG gauges at different levels having similar temperatures. The average temperature of all FPG gauges and the average temperature of all concrete deck gauges were plotted and compared in Figure 7-1, showing the difference predominantly occurring in the summer months. In a similar manner, the temperature at the tilt-meters (located about 2 feet and 4 feet below the top of the deck on the river side of the abutments) and temperature at the pressure cells (4 feet below the bottom of approach slab on the backfill side of the abutments) were also investigated and used to represent the temperatures at the river side and the backfill side of the abutments. To show the temperature gradients, the temperatures of all gauges mentioned above were plotted for the hottest days and coldest days among the two years data record period in Figure 7-2 and Figure 7-3. In this data it is shown that the gradient is much more pronounced in the summer, and also that the gradient in the summer is a consistent daily fluctuation. Since the effect of the temperature gradient is unknown, both ambient temperatures and gradient temperatures were considered in the analysis, in which the average temperatures of the FPG gauges were used as the ambient temperature and the actual temperatures of different gauges were used as the gradient temperature. Also, the average temperature of FPG gauges at the end of construction was used as the reference temperature in the analysis. The temperature used in the analysis are values recorded on the hottest (7/18/2013) and coldest day (1/24/2013) within the data record period and values are listed in Table 7-2, with gradient temperatures at the top of the deck obtained by linear interpolation of the deck gauges readings and the

FPG top flange gauges readings, which may underestimate the top of deck temperatures.

In total, 9 models were created in the parametric analysis. Models 1 to 4 account for the effect of different soil properties on the bridge under extreme ambient temperatures. Model 5 and Model 6 account for the effect of the pinned connections between piles tips and bottom of the abutments. It should be noted that ambient temperature is only applied to the superstructure with other components (abutments and piles) using reference temperature in these 6 models. Model 7 and Model 8 account for the effect of gradient temperature at the superstructure and the abutments separately, while Model 9 account for gradient temperature at both superstructure and abutments. Note that in Model 8 and Model 9, the original shell elements at the abutment were changed and modeled as solid elements in order to allow for the effect of gradient temperature within the abutment elements. The summary of different models and parameters used in them are listed in Table 7-3.

Table 7-1 Soil properties of backfill and soil around piles

Material	Type	Location of ground water table	Unit weight [Pcf (kN/m3)]	Internal friction angle (degree)	Lateral subgrade constant [Pci (kN/m3)]
Abutment backfill soil	Very dense	below	140 (22)	45	220 ($60x10^3$)
	Medium dense	below	120 (19)	35	60 ($16x10^3$)
Soil around Pile	Dense to very dense	above	135 (21)	40	155 ($42x10^3$)
	Medium dense	above	120 (19)	35	40 ($11x10^3$)

Table 7-2 Temperature values used in the parametric analysis

Ambient temperature [°F (°C)]		**Reference temperature [°F (°C)]**
Summer	93 (51.7)	49.5 (27.5)
Winter	7 (3.9)	

Gradient temperature[°F (°C)]					
Superstructure					
	Top of deck [°F (°C)]	Middle of deck [°F (°C)]	Bottom of deck/ FPG Top flange [°F (°C)]	FPG Web [°F (°C)]	FPG Bottom flange [°F (°C)]
Summer	119.1 (66.2)	107.8 (60.0)	96.5 (53.6)	91.3 (50.7)	90.2 (50.1)
Winter	-1 (-0.6)	3.1 (1.7)	7 (3.9)	7 (3.9)	7 (3.9)

Abutments		
	River side [°F (°C)]	Backfill side [°F (°C)]
Summer	87 (48.3)	76 (42.2)
Winter	11 (6.1)	36 (20)

Table 7-3 Summary of different models used in parametric analysis

Model number	Piles to Abutment connection	Abutment Soil Spring properties	Pile soil spring properties	Superstructure Temperature	Abutment Temperature
Model 1	fixed	Medium dense sand	Medium dense sand	Ambient	Ref. Temp
Model 2	fixed	Dense Sand	Dense Sand	Ambient	Ref. Temp
Model 3	fixed	No soil spring	No soil spring	Ambient	Ref. Temp
Model 4	fixed	Dense sand	No soil spring	Ambient	Ref. Temp
Model 5	Pinned	Dense sand	Dense Sand	Ambient	Ref. Temp
Model 6	Pinned	Dense sand	No soil spring	Ambient	Ref. Temp
Model 7	fixed	Dense Sand	No soil for summer Dense Sand for winter	Gradient	Ref. Temp
Model 8	fixed	Dense Sand	No soil for summer Dense Sand for winter	Ambient	Gradient
Model 9	fixed	Dense Sand	No soil for summer Dense Sand for winter	Gradient	Gradient

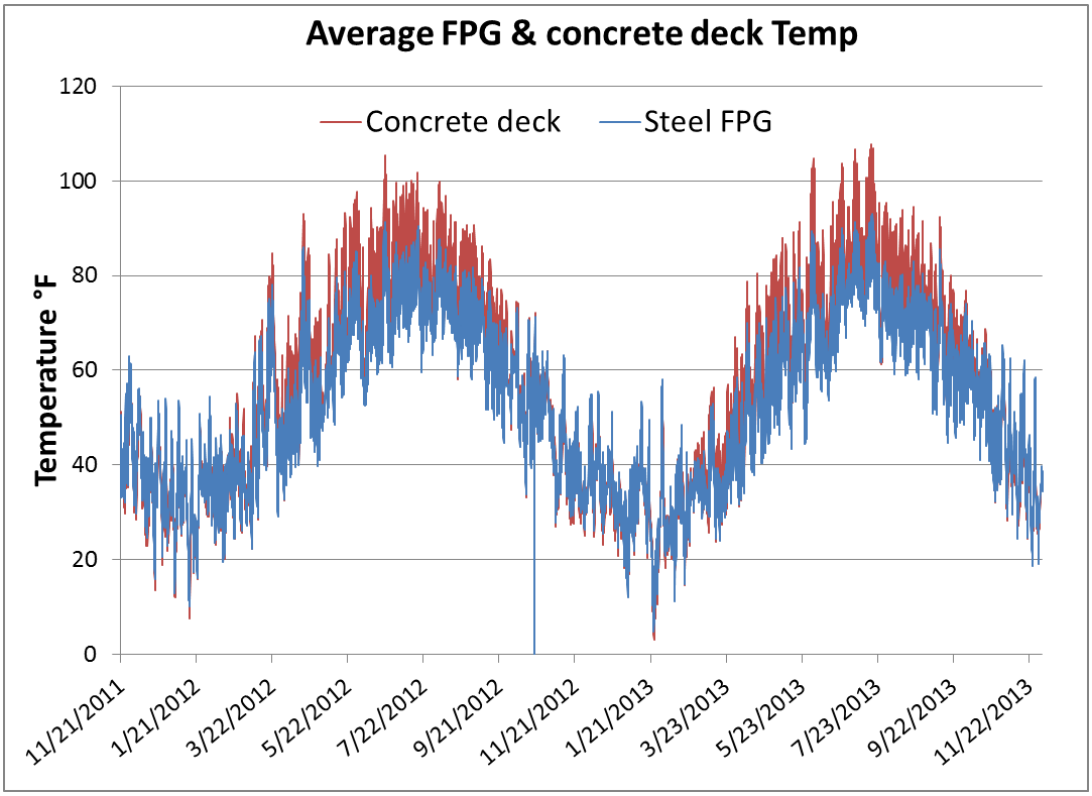

Figure 7-1 Average FPG and concrete deck temperature

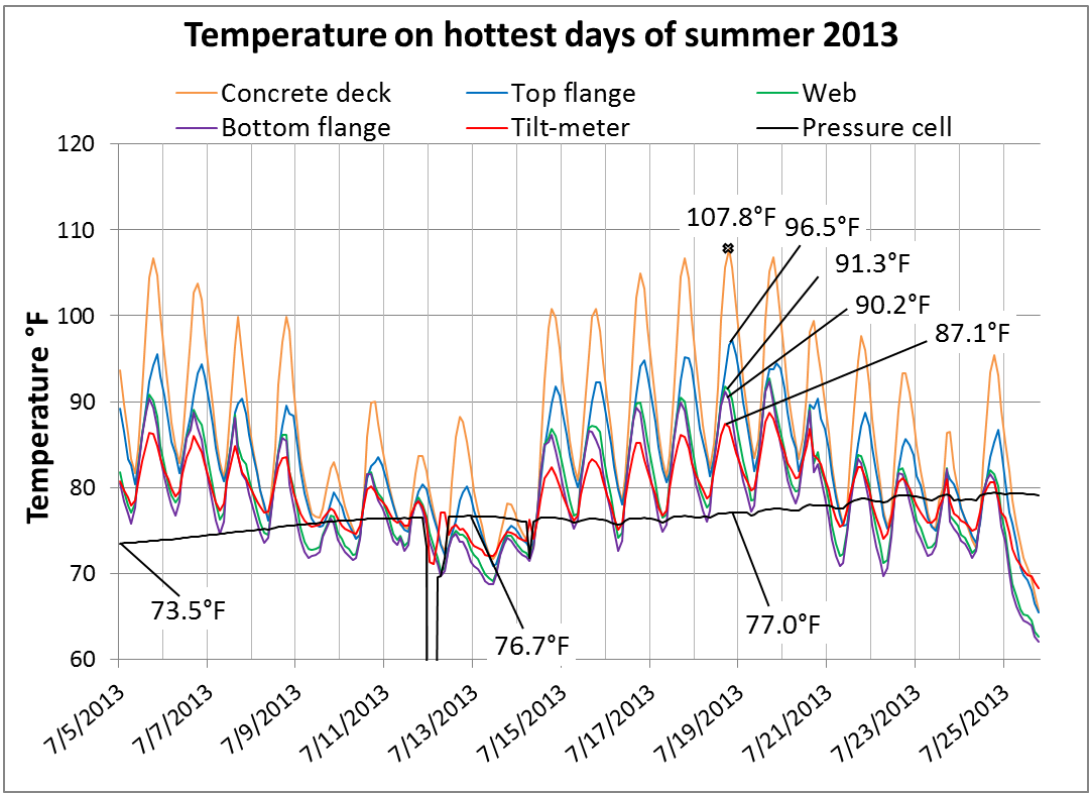

Figure 7-2 Temperatures of different gauges during the hottest days of 2013

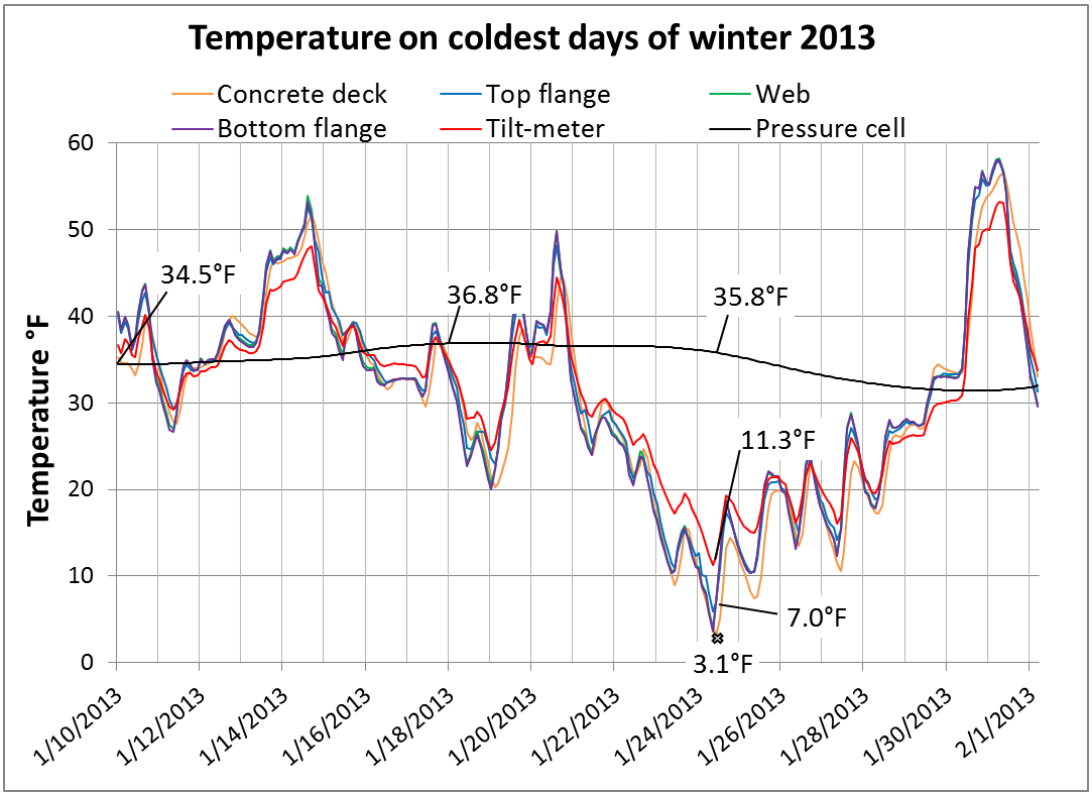

Figure 7-3 Temperatures of different gauges during the coldest days of 2013

7.2 Abutments rotation

In this section, the abutment rotation results of the parametric analysis is presented and compared to the field data. In general, abutment rotations toward the backfill (negative value) are expected during bridge span expansion and rotations toward the river/superstructure (positive value) are expected during contraction. Also, the behavior of the integral abutment bridges during expansion are affected by soils at both abutments and pile levels, while during contraction it is only affected by the soils at pile level. Therefore, it is possible that the abutment rotations can be expected to have a different slope (vs temperature) during temperature increase versus temperature decrease.

The long term abutment rotations were shown in Figure 6-29 in Section 6.4, rotations towards backfill were recorded during expansion and rotations toward the river/superstructure were recorded during contraction as expected. A shift in the rotation toward the backfill soil (negative values) was observed. One of the explanation for this could be permanent displacement was induced at the bottom of the abutments due to backfill soil movement during expansion and contraction. Another explanation could be that during expansion of the superstructure, cracks at the top of the deck expanded and were filled with dust and dirt. Subsequently, the top of the deck is effectively slightly expanding each year, and results in permanent rotations towards the backfill soils.

The upper tilt-meters readings were used to compare with the parametric results. In order to show comparison better, the tilt-meters readings on both east and west abutments were plotted against ambient temperature in Figure 7-4, and

blue dots represent data recorded in 2011, red dots for 2012 and green dots for 2013. Furthermore, the data were investigated separately based on instantaneous temperature increase and temperature decrease, plotted in Figure 7-5. Linear trend lines were added to the data to show the slope. In west abutment, the slope of abutments rotation with respect to instantaneous temperature increase is shallower compare to temperature decrease in the first two years [2011~2012] and become similar in the third year [2013]. This indicates that soil movements happened at the backfill in the first two year [2011~2012] while soils become almost stabilized at the third year [2013]. Similar behavior is observed in the east abutment, except the slope respect to instantaneous temperature increase is still shallower (but less shallow compare to the first two year [2012~2013]) than that of temperature decrease in the third year [2013]. This indicates soil movements are still happening at the end of third year but will likely become stabilized at the following year. Yearly shift in the abutment rotation is also shown in Figure 7-4 and Figure 7-5, as the x-intersect became more negative (rotation toward backfill) in subsequent years.

The results of the parametric analysis were listed in Table 7-4 and compared to the trend lines of upper tilt-meters data in Figure 7-6 and Figure 7-7, in these two figures the slopes of third year data and Model 9 result correspond to instantaneous temperature increase and decrease are stated in the lower left corner. Noted that only result of Model 2, Model 4, Model 7, Model 8 and Model 9 are shown in Figure 7-6 and Figure 7-7 as these models are found to be more significant in the next paragraph.

From Table 7-4, first, observed that the parametric analysis result in similar values between west and east abutments. This suggests that the difference in rotation between the two abutments observed in field data is likely due to that the actual soil properties between the two abutments are different. Second, from Model 1 to Model 2, changing from medium dense sand to dense sand at both the abutments and piles levels do not have big effect at abutments rotation. While in Model 3 when no soil is employed, it will result in opposite rotation values compare to the Model 1, Model 2, Model 4 and the field data. And in Model 4, which was intended to model extreme soil condition in summer, the results showed that it will slightly increase the rotation toward the backfill compare to Model 1 in summer. Among the 4 models, Model 4 gives largest absolute reading in summer while Model 2 gives largest reading in winter. Third, by comparing Model 5 and Model 6 to Model 2 and Model 4 respectively, observed that when the piles were pinned to the abutments, rotations do not change much in both summer and winter. Last, gradient temperatures were used in Model 7 and Model 8. It was observed that in Model 7, the temperature gradient (due to sun radiation) at the superstructure in summer increased the rotation by about 2 times (compare Model 4 and Model 7), while in winter the thermal gradient is minimal so variations between Model 2 and Model 7 are negligible. On the other hand, when gradient temperature is employed in the abutments in Model 8, the rotation increased by about 30 percent in summer (with a temperature difference of 10 °F [5.6°C] between the backfill and river faces of the abutments), whereas the rotations increased by about 2 times in winter (with a temperature difference of about 25 °F [13.9°C] between the faces of the abutments).

Result of Model 9 is used to compare to the field data as it employed thermal gradient effect at both the abutments and superstructure, and third year field data is used in the comparison since soils are the most stable within the data record period. Also, only the slopes (vs temperature) of model results and field data are used as the quantity for comparison while the x-intersect of the linear trend line of the field data is ignored, since it represents the shift of the data which is not captured in FEM. Again, the slopes (vs temperature) of Model 9 result and third year field data are stated in Figure 7-6 and Figure 7-7. During instantaneous temperature increase, the slope of Model 9 result equals to about 85 percent of the field data in west abutment, whereas it is about 71 percent in east abutment. The difference between the two abutments is likely because soils movements are still found in east abutment in the third year while soils in west abutment are almost stabilized as noted before. During instantaneous temperature decrease, the slope of Model 9 result equals to about 52 percent of the field data in both abutments. This shows that the ANSYS model is able to capture the rotations of the abutments under thermal loading in summer (temperature increase) when thermal gradient is accounted for, while underestimating the rotation in winter (temperature decrease). The possible reasons for the less accuracy of the model in winter could be the active soil pressure due to backfill compaction during construction (or possibly due to abutment movements happened before the reference point of field data), i.e. soils are pushing the abutments even when no temperature change is induced, and it is assumed to be zero in the model.

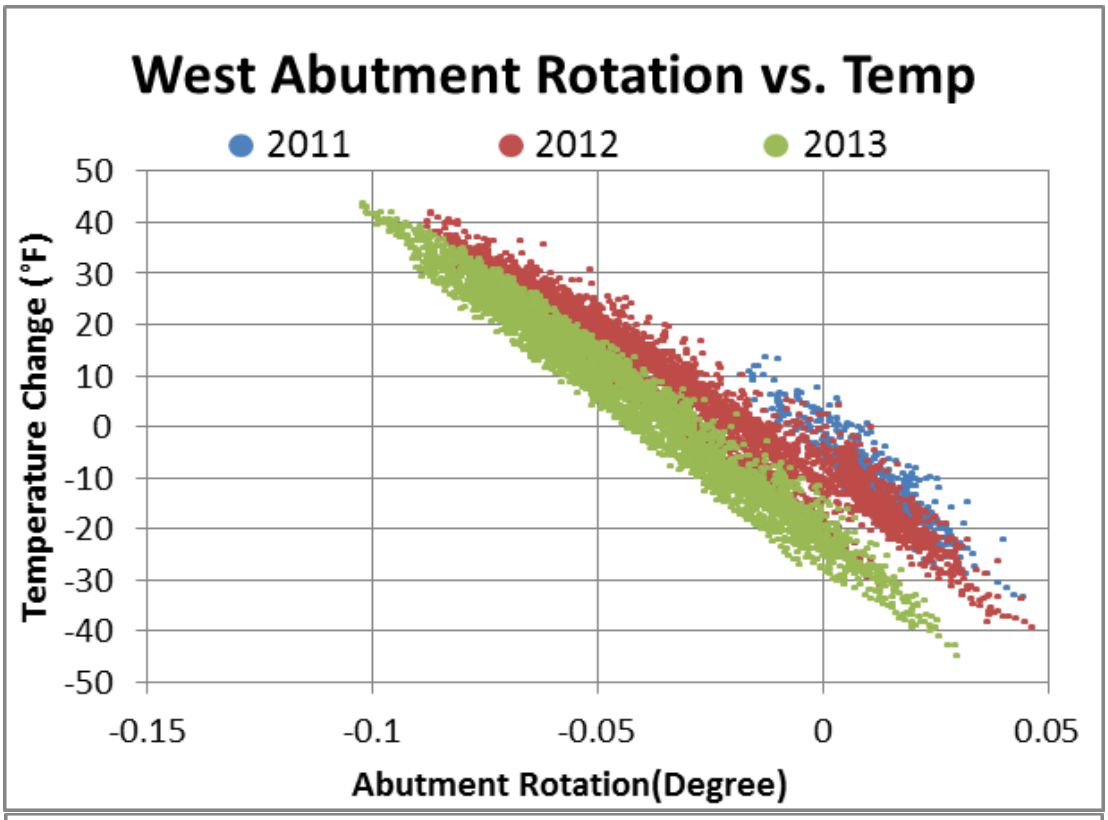

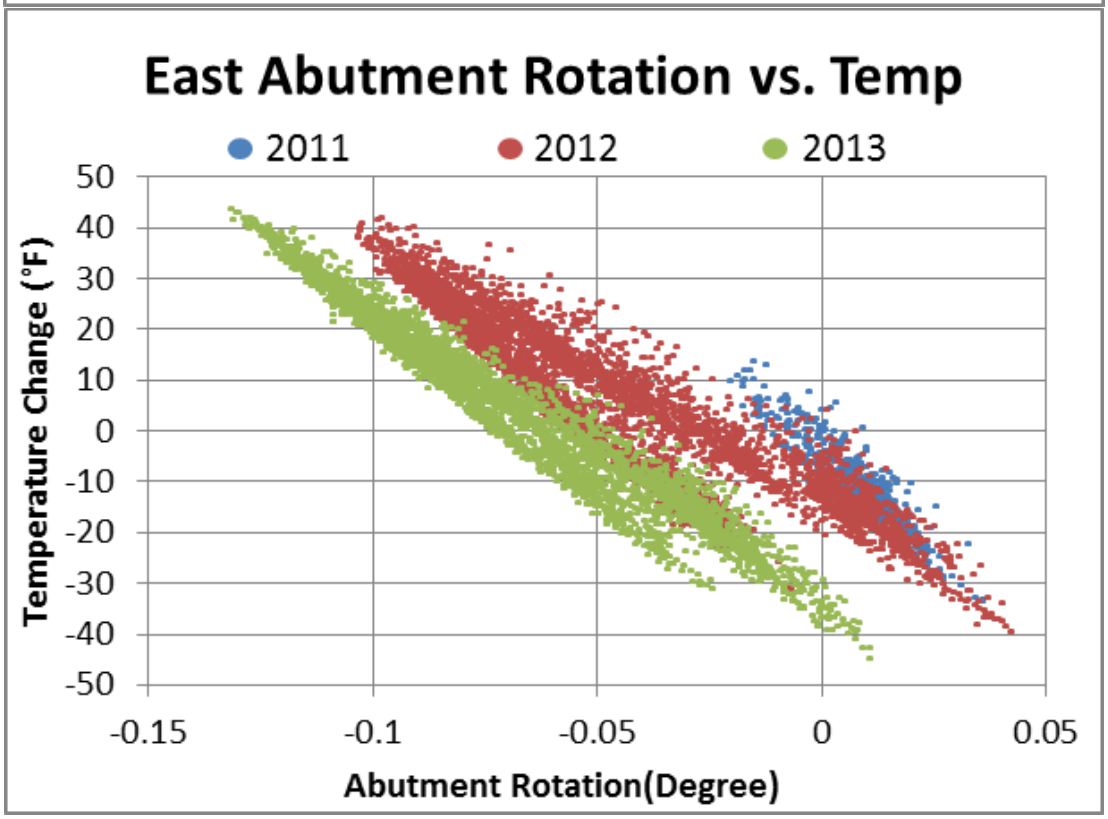

Figure 7-4 Abutments rotation plotted against ambient temperature change

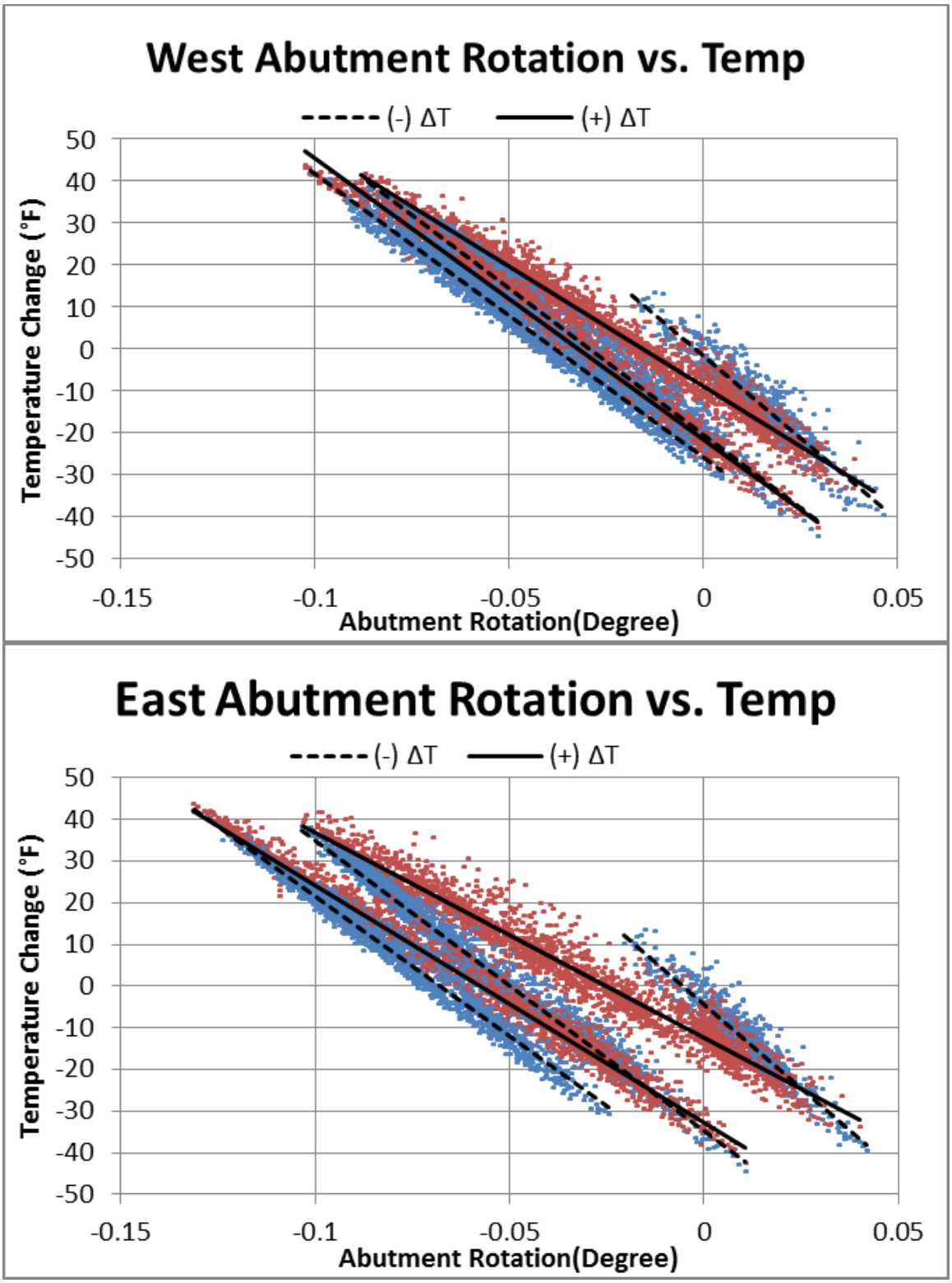

Figure 7-5 Abutments rotation plotted against increasing and decreasing instantaneous temperature change

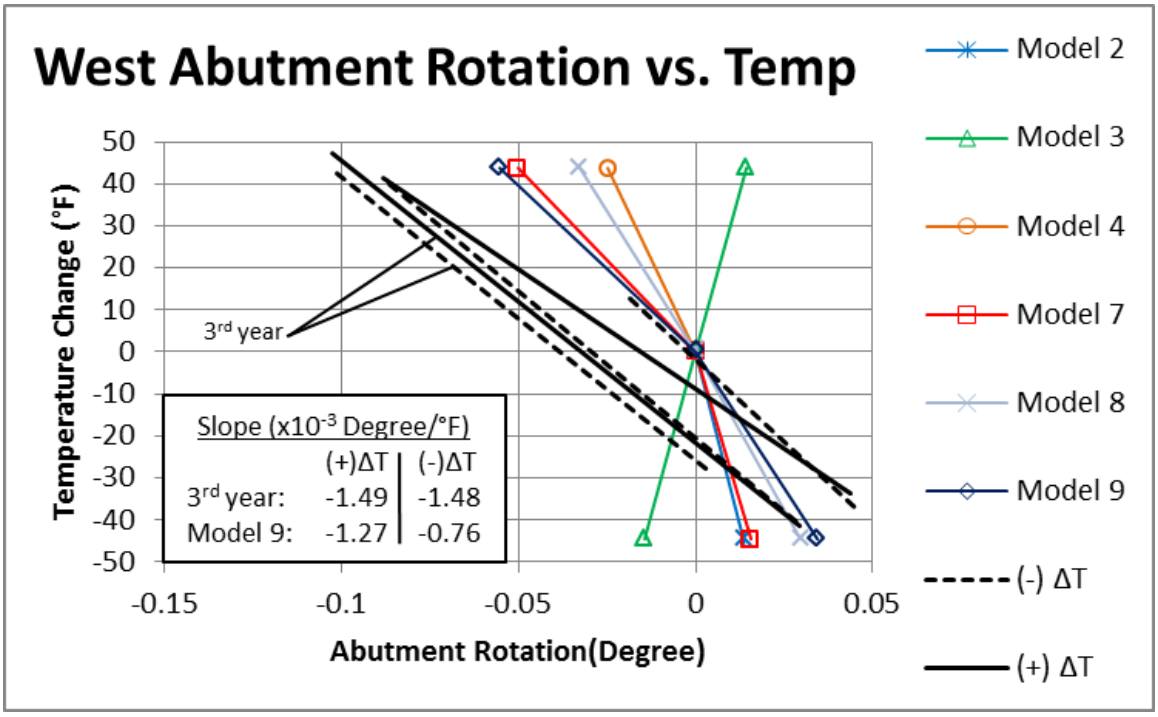

Figure 7-6 Comparison between parametric analysis result and west abutment field rotation readings

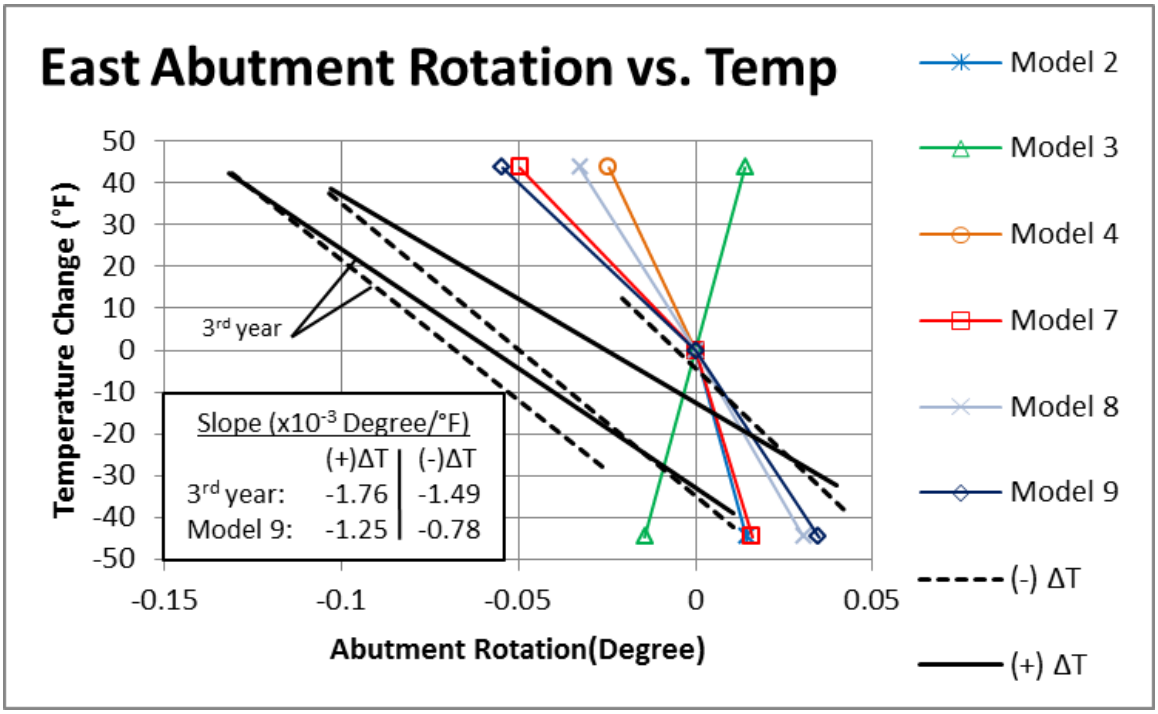

Figure 7-7 Comparison between parametric analysis result and east abutment field rotation readings

Table 7-4 Parametric analysis abutment rotation results

Rotation (degree)	WEST Abutment		EAST Abutment		Description
	Summer	Winter	Summer	Winter	
Model 1	-0.021	0.012	-0.020	0.013	Medium-dense sand
Model 2	-0.021	0.014	-0.020	0.014	Dense sand
Model 3	0.014	-0.015	0.014	-0.014	Without soil
Model 4	-0.025	-0.015	-0.025	-0.014	Dense sand at abutments, but no soil at piles
Model 5	-0.023	0.013	-0.022	0.013	Model 2 with piles pinned to abutments
Model 6	-0.025	-0.022	-0.025	-0.022	Model 4 with piles pinned to abutments
Model 7	-0.050	0.016	-0.050	0.016	Model 2 (winter) and Model 4 (summer) with gradient temp at superstructure
Model 8	-0.033	0.030	-0.033	0.030	Model 2 (winter) and Model 4 (summer) with gradient temp at abutments
Model 9	-0.056	0.034	-0.055	0.035	Model 2 (winter) and Model 4 (summer) with gradient temp at superstructure and abutments

7.3 Superstructure longitudinal strain

In this section, the behavior of the bridge longitudinal strain under seasonal temperature will be discussed. The first part of this section will talk about the general behaviors of thermal induced strain in bridges with deck joints and integral abutment bridges. The second part will talk about the result of the parametric analysis and comparison to the field data. The third part will talk about the bridge longitudinal strain behavior under daily temperature change. At last, the summary of this section will be presented.

7.3.1 General behavior of thermal induced strain

In general, for a single structural element under thermal loading, the total strain ε_T of the element will consist of two parts: the free strain ε_F and the mechanical strain ε_M. The free strain represents the part of deformation of the element if it were to expand /contract freely without any constraint and $\varepsilon_F = \alpha\Delta T$,

where α is the coefficient of thermal expansion of the element and ΔT is the change in temperature. The mechanical strain represents the part of deformation of the element due to compatibility and boundary condition constraints. Based on these two definitions, one can see that the free strain does not develop any stress in the element, while the mechanical strain components develop thermally induced stresses in the element due to compatibility and boundary conditions. Therefore, the mechanical strain $\varepsilon_M = \sigma/E$, where σ is the stress in the same direction and E is the modulus of elasticity. A simple example is shown in Figure 7-8 to illustrate the above definition: The example is a one dimensional (1-D) thermal expansion of a fixed end beam. The coefficient of thermal expansion of the beam is α_b, and the uniform temperature increase is ΔT. The free strain ε_F is therefore equal to $+\alpha_b \Delta T$ (positive indicates tension, negative indicate compression). Due to the fixed end condition, no deformation at the ends of the beam is allowed, and therefore the total strain is equal to zero. As a result the mechanical strain ε_M is equal to $-\varepsilon_F = -\alpha_b \Delta T$, and the stress in the beam is equal to $E^*\varepsilon_M = -E\alpha_b \Delta T$ (compression).

For the steel girder bridges considered in this research, the deck and girders are made of different materials with corresponding differences in coefficients of thermal expansion and moduli of elasticity between the two components. This means that at the interface of the two components, the free strain is discontinuous as the two components deform different amounts under the same temperature change, and the difference in strain $\Delta\varepsilon_{interface}$ is equal to $(\alpha_G - \alpha_D)\ \Delta T$, where α_G is the coefficient of thermal expansion of girders and α_D is that for the deck. Due to compatibility, (the total strain profile is continuous), the mechanical strain is also

discontinuous at the interface. Also, stresses will be induced in the superstructure even without any end restraint, due to the compatibility at the interface. This is illustrated in an example shown in Figure 7-9. In the example, the superstructure is expanded under a uniform temperature increase. The girder is expanding more compare to the deck and at the interface the mechanical strain at the bottom of the deck expanded more and the top of the girder expanded less in order to achieve the compatibility. As a result, the superstructure undergoes a curvature, and tension is induced in the bottom of both components and compression is induced at the top of both components.

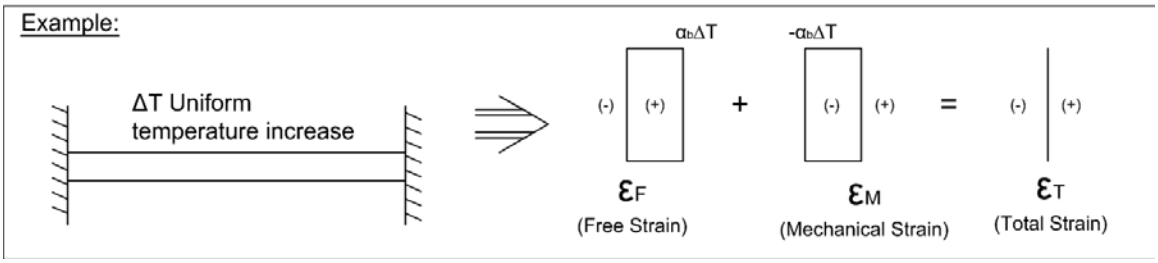

Figure 7-8 Example of different parts of strain under thermal loading

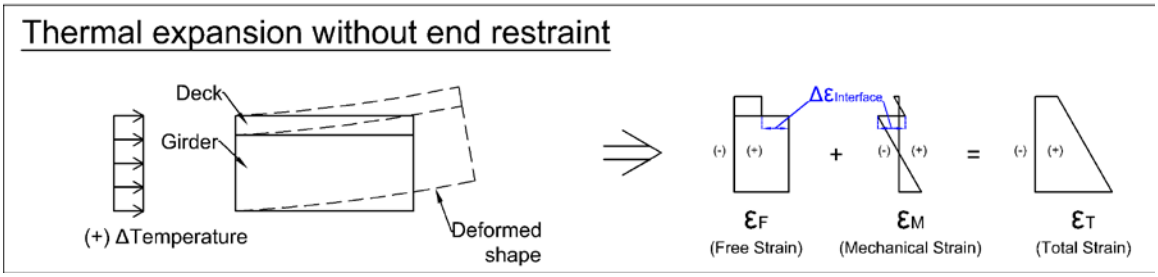

Figure 7-9 Example of thermal expansion without end restraint

7.3.2 **Field data behavior**

Before showing the strain result of the parametric analysis, the long term longitudinal strain data of FPG are plotted against ambient temperature to show the behavior of the data in Figure 7-10 and Figure 7-11. One thing should be keep in mind that the gauges readings represent the mechanical strain part of the total

strain in the girder since temperature corrections were done in all gauges when interpreting the reading. Thus, the gauge readings represent the stress in the girder when multiplied by the modulus of elasticity of the steel. In the plots, negative readings indicate compressive strain and positive reading indicate tensile strain, and blue dots represent data recorded in 2011, red for 2012 and green for 2013.

From these plots and the data, first, the FPG longitudinal strain exhibit large variations versus the same temperature, with a maximum variation of about 120με found in interior girders (G2 N-side Web) and 200με in exterior girders (G4 S-side Web). Second, similar strain distributions were observed year to year. Third, similar distributions were found between exterior girders (G1 and G4) and between interior girders (G1 and G2) with the exception between the far north web gauges SG144 (G1) and the far south web gauge SG163 (G4). These two gauges record typically larger readings compare to other gauges. Also, the far south web gauge SG163 records more negative (more compressive) strain readings between -40°F [-22.2°C] to 10°F [5.6°C] temperature change but less negative readings between 10°F [5.6°C] to 40°F [22.2°C] temperature change compare to the far north web gauge SG144. Last, it was found that maximum readings (both compressive and tensile) did not occur at the maximum ambient temperature change, but at a smaller ambient temperature change. The most negative and positive FPG strain readings at different depth locations are shown in Table 7-5. The maximum readings are found to be happened at the far south web gauges (SG163), and are equal to -112με (compression) and 131με (tension) which correspond to a maximum compression of 3.3 ksi [22.8 MPa] and tension of 3.8 ksi [26.2 MPa] in the steel FPG.

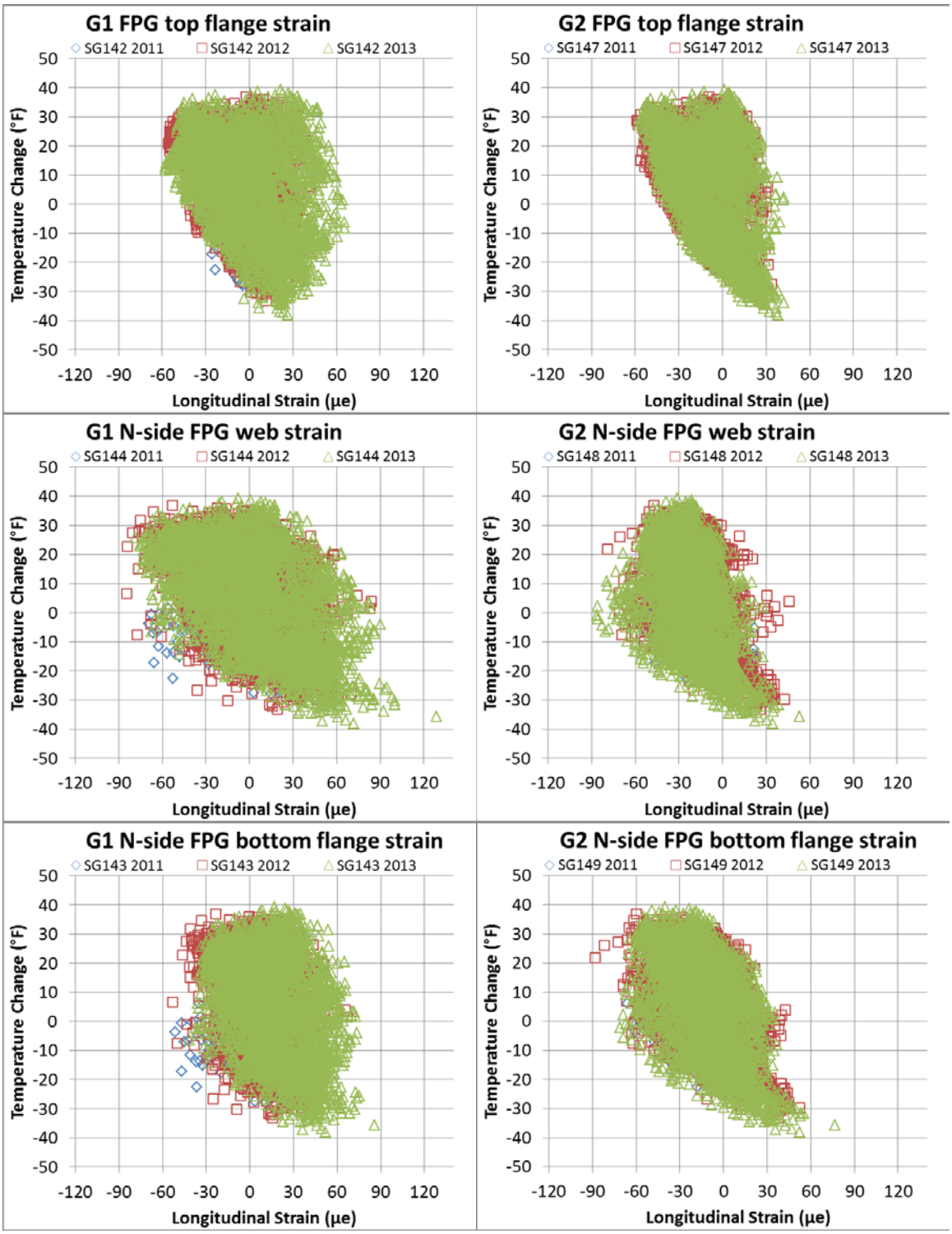

Figure 7-10 FPG longitudinal strain Girder 1 and Girder 2 plotted against ambient temperature change

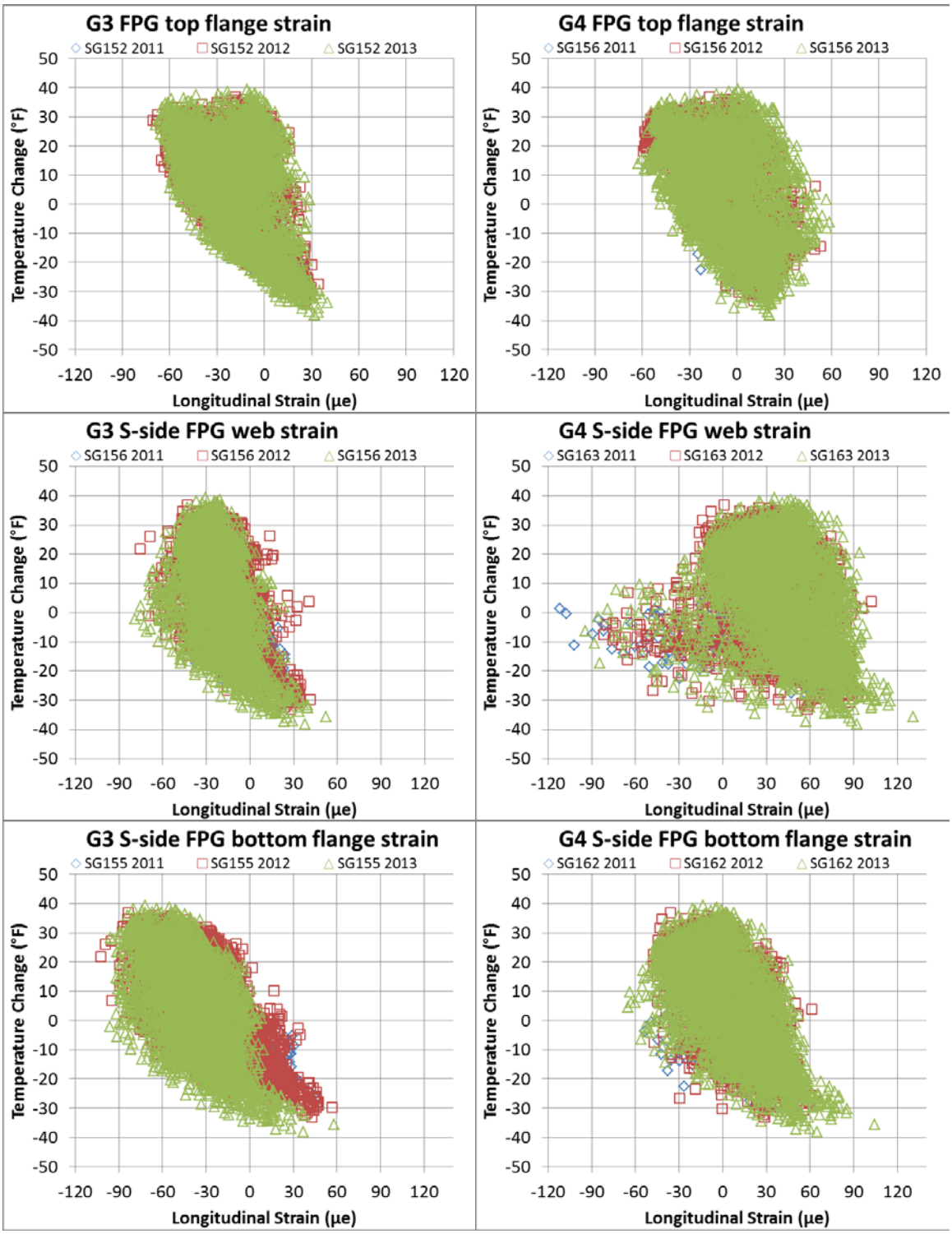

Figure 7-11 FPG longitudinal strain at Girder 3 and Girder 4 plotted against ambient temperature change

Table 7-5 Maximum strain readings at different locations

Location	Top flange	Mid-height web	Bottom flange
Int. girders	-70 to 40 με	-86 to 66 με	-107 to 77 με
Ext. girders	-62 to 66 με	-112 to 131 με	-65 to 104 με

7.3.3 Parametric analysis result and comparison to field data

FEM parametric analysis strain results at the gauge locations were retrieved from the ANSYS models and are shown in Table 7-6 and Table 7-7 with negative values indicate compressive strain and positive values indicate tensile strain. In the two tables, the result of Model 3 in summer and Model 3, Model 4 and Model 6 in winter are not listed as it was found in Section 7.2 that they show opposite behavior compare to the rotation field data. Also, note that due to symmetry of the bridge, the ANSYS results are symmetric about the center-line of the bridge and therefore only results of G1 and G2 are shown. The differences between FEM results in exterior and interior girders are listed in Table 7-8. The field data recorded on the hottest and coldest day is shown in Table 7-9.

From Table 7-6 and Table 7-7 the ANSYS FEA results between Models 1, 2, 4, 5 and 6 are very similar, this indicates that pinned pile to abutment connection and different backfill and pile soil properties do not affect the strain distribution in the girder. However, it should be kept in mind that the presence of soil spring in the model is still important since model without soil spring (Model 3) shown opposite behavior to the field data. Model 7, which includes thermal gradient in the superstructure, results in lower strain values (less compressive in summer and less tensile in winter, especially in exterior girders) compare to other models that do not consider thermal gradient in the superstructure. This implies that the thermal

gradient at the maximum temperature can significantly change the strain distribution in the girder and result in a less compressive (in summer)/ tensile (in winter) strain reading at the bottom flange. Model 8, which includes thermal gradient in the abutments, results in larger strain values (at web and bottom flange) compared to Model 1 to 6 which contradicts the results of Model 7. Moreover, from Table 7-8, by comparing Model 7 and Model 8 to other models, observed that thermal gradient in the superstructure and the substructure will alter the load distribution between exterior and interior girders. Last, model 9 results are used to compare with the field data (in Table 7-9), it was found that results in interior girders give similar trend and closer values to the field data compared to that in the exterior girders.

Table 7-6 Parametric analysis longitudinal strain results at interior girders

Interior girders (G2, G3)	Strain in Summer (με)					Strain in Winter (με)				
	Top flange	N-side web	S-side web	N-side Bottom flange	S-side Bottom flange	Top flange	N-side web	S-side web	N-side Bottom flange	S-side Bottom flange
Model 1	-46.16	-56.59	-60.36	-70.89	-73.29	44.55	48.68	52.56	56.53	58.99
Model 2	-47.25	-57.57	-61.34	-71.77	-74.17	44.58	49.89	53.78	58.96	61.43
Model 4	-46.05	-59.94	-63.71	-77.82	-80.22	-	-	-	-	-
Model 5	-46.50	-58.92	-62.69	-75.29	-77.69	44.61	49.06	52.94	57.25	59.71
Model 6	-45.92	-60.02	-63.78	-78.10	-80.50	-	-	-	-	-
Model 7	-15.96	-21.90	-28.24	-54.56	-58.26	26.17	34.85	38.68	46.80	49.15
Model 8	-38.21	-61.58	-63.07	-87.36	-88.93	40.74	60.47	63.43	83.38	86.65
Model 9	-8.69	-20.84	-24.83	-58.88	-61.58	23.88	48.71	52.07	76.71	80.06

Table 7-7 Parametric analysis longitudinal strain results at exterior girders

Exterior girders (G1, G4)	Strain in Summer (με)					Strain in Winter (με)				
	Top flange	N-side web	S-side web	N-side Bottom flange	S-side Bottom flange	Top flange	N-side web	S-side web	N-side Bottom flange	S-side Bottom flange
Model 1	-24.74	-37.44	-43.59	-56.35	-59.49	21.68	28.13	34.49	40.71	43.96
Model 2	-25.78	-38.40	-44.56	-57.25	-60.38	21.83	29.45	35.82	43.25	46.51
Model 4	-25.09	-41.25	-47.37	-63.70	-66.83	-	-	-	-	-
Model 5	-25.33	-40.03	-46.17	-61.00	-64.13	21.79	28.57	34.92	41.49	44.73
Model 6	-24.98	-41.34	-47.45	-63.98	-67.12	-	-	-	-	-
Model 7	19.56	25.69	8.87	-0.92	-17.78	3.65	9.50	17.75	21.60	28.41
Model 8	-32.55	-55.03	-56.14	-79.08	-80.76	26.36	41.85	44.44	58.72	63.26
Model 9	12.33	15.05	2.93	-11.37	-26.84	6.81	22.46	28.04	40.62	49.41

Table 7-8 Difference between parametric results in interior and exterior girders

Difference between Ext. and Int.	Strain in Summer (με)					Strain in Winter (με)				
	Top flange	N-side web	S-side web	N-side Bottom flange	S-side Bottom flange	Top flange	N-side web	S-side web	N-side Bottom flange	S-side Bottom flange
Model 1	-21.42	-19.15	-16.77	-14.55	-13.80	22.87	20.55	18.07	15.82	15.03
Model 2	-21.47	-19.17	-16.78	-14.53	-13.78	22.75	20.44	17.96	15.71	14.92
Model 4	-20.96	-18.69	-16.35	-14.12	-13.39					
Model 5	-21.17	-18.89	-16.53	-14.29	-13.56	22.82	20.50	18.02	15.76	14.98
Model 6	-20.94	-18.67	-16.33	-14.12	-13.39					
Model 7	-35.52	-47.58	-37.11	-53.64	-40.49	22.52	25.36	20.94	25.21	20.74
Model 8	-5.66	-6.54	-6.93	-8.28	-8.17	14.39	18.61	18.99	24.65	23.40
Model 9	-21.02	-35.89	-27.76	-47.51	-34.74	17.07	26.25	24.02	36.09	30.65

Table 7-9 FPG strain field data

Field data	Strain in Summer (με) [7/18/13 6:00PM]					Strain in Winter (με) [1/24/13 10:00AM]				
	Top flange	N-side web	S-side web	N-side Bottom flange	S-side Bottom flange	Top flange	N-side web	S-side web	N-side Bottom flange	S-side Bottom flange
G1	1.09	11.24	N.A.	27.42	-6.28	23.56	50.25	N.A.	36.10	25.90
G2	-20.75	-20.51	-7.51	-18.50	-38.96	36.86	22.40	36.22	35.79	22.61
G3	-29.31	-25.34	-22.39	-38.48	-51.17	34.18	22.95	23.27	32.32	17.97
G4	-13.16	-9.92	50.04	-21.53	-0.87	19.62	31.17	57.07	17.16	50.25

***Note: "N.A." implies gauge is out of order and no data is available.

7.3.4 **Daily temperature fluctuation**

This section investigated the daily temperature fluctuation effect on the FPG strain. Strain data were plotted separately for the hottest and coldest 5 days within the two year period of data collection, along with the average deck, average top flange, average web and average bottom flange temperature plotted in the secondary vertical axis, in Figure 7-12, Figure 7-13, Figure 7-14, and Figure 7-15. The strain readings of the deck gauges located directly above the FPG were included in these plots. In the plots, solid lines represent strain readings and dashed lines represent average temperature readings

From the plots, it was found that the maximum tensile strain in winter and maximum compressive strain in summer happened at time when the temperature in the deck and the FPG are similar (thermal gradient is small or zero), whereas lower

readings were found when a thermal gradient exists (with the deck being hotter during expansion in summer and colder during contraction in winter). This matches the ANSYS FEA results previously presented which concluded that including the thermal gradient in the superstructure resulted in smaller FPG strain values compared to similar models that neglected the thermal gradient. Additionally, the strain in the FPG can change from all in tension to all in compression (reverse curvature of superstructure) within a day during winter when the temperature rises, especially in G1 and G4 during the winter of 2012. On the other hand, the maximum tensile and compressive FPG strain field data (shown previously in Table 7-5) did not occur during maximum and minimum temperatures in the summer and winter (respectively). Instead, the maximum readings are recorded in the far south gauge SG163 on Nov 2011 and Feb 2013, plotted in Figure 7-16. On these dates a reverse temperature gradient is observed in Figure 7-16, in which the girders are warmer than the deck during expansion and colder during contraction of the superstructure. In this case the strains add to the thermal results and provide maximum effects.

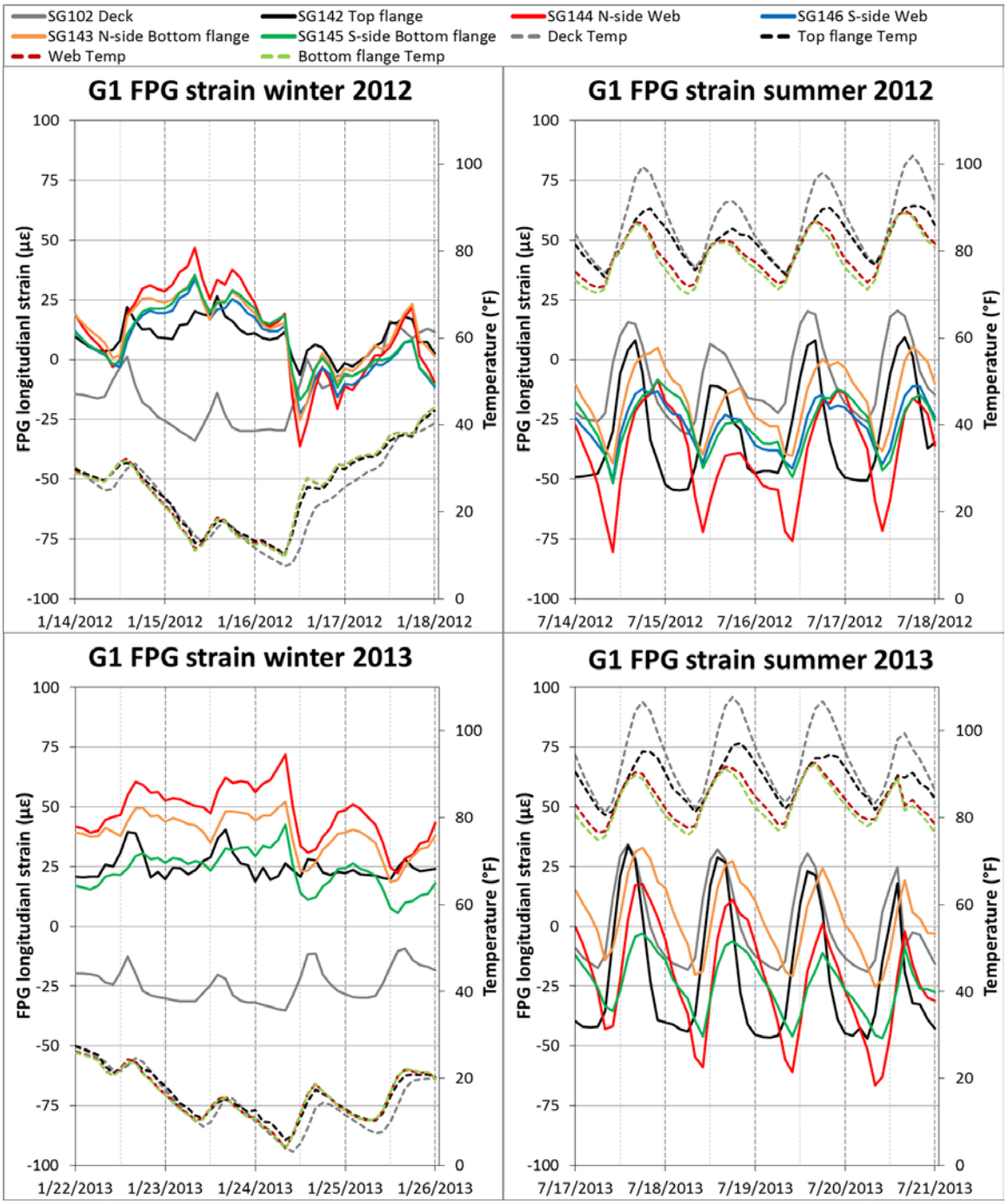

Figure 7-12 Longitudinal strain readings of girder 1 during the hottest and coldest 5 days in each year alongside with the temperatures fluctuation

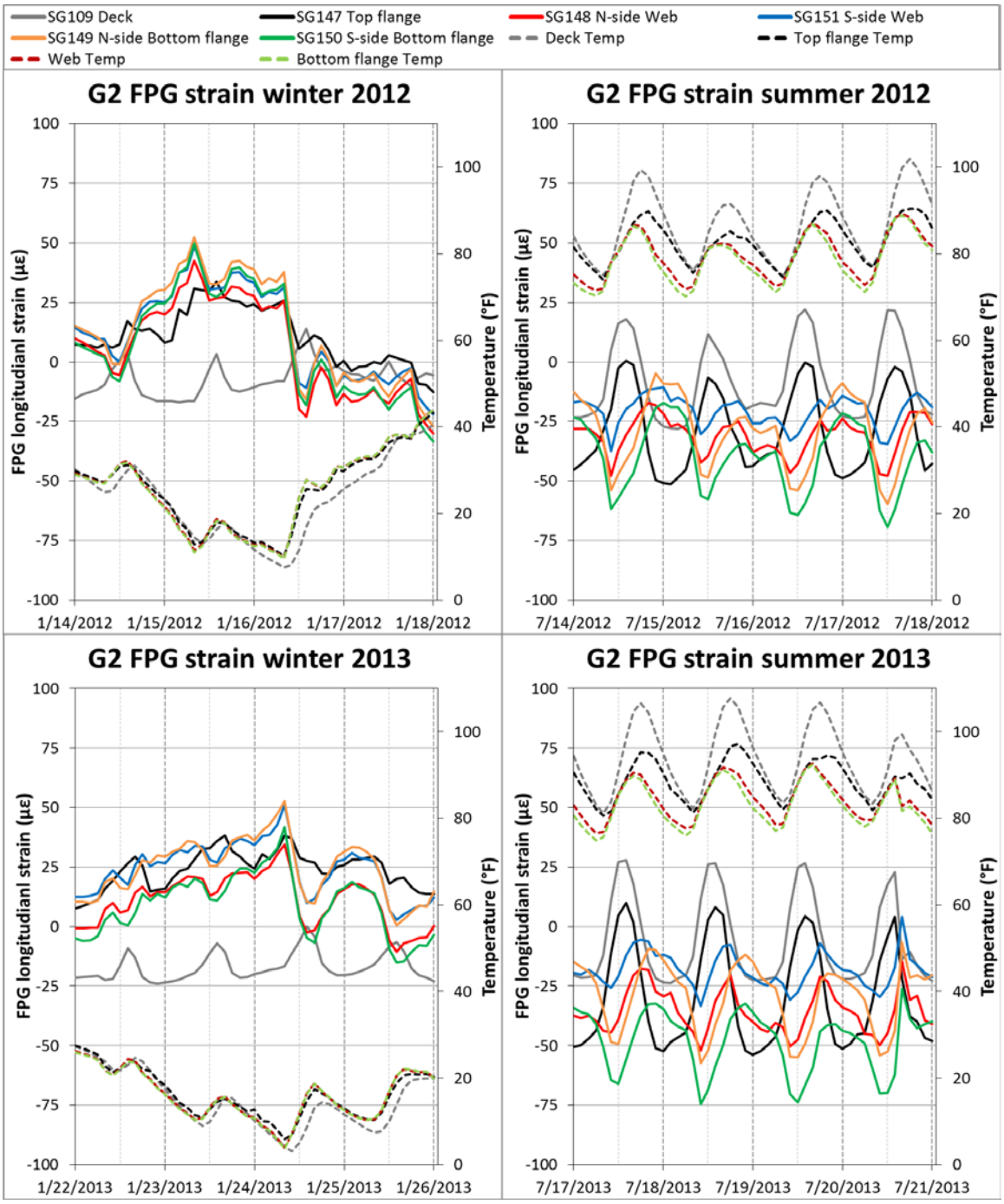

Figure 7-13 Longitudinal strain readings of girder 2 during the hottest and coldest 5 days in each year alongside with the temperatures fluctuation

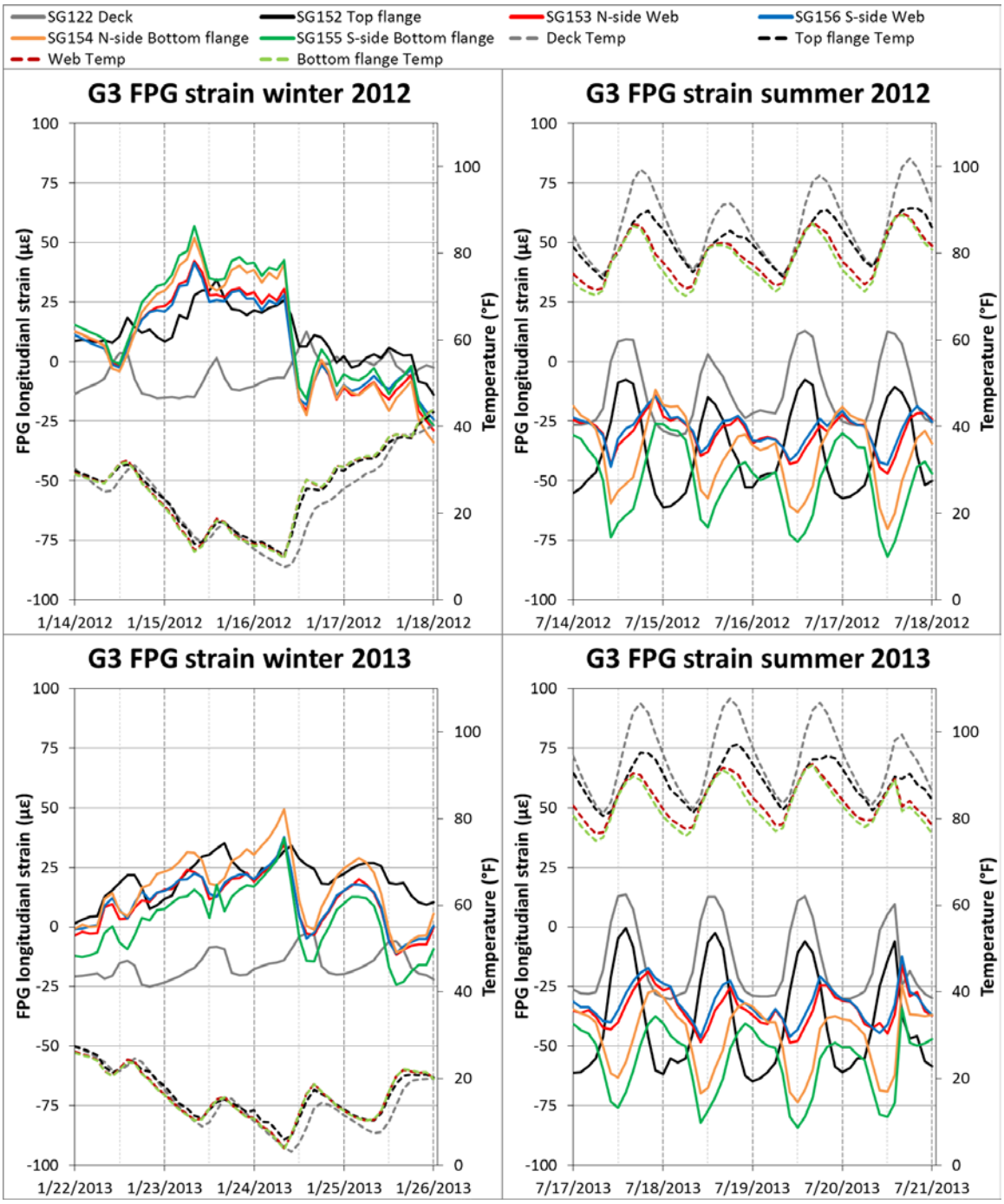

Figure 7-14 Longitudinal strain readings of girder 3 during the hottest and coldest 5 days in each year alongside with the temperatures fluctuation

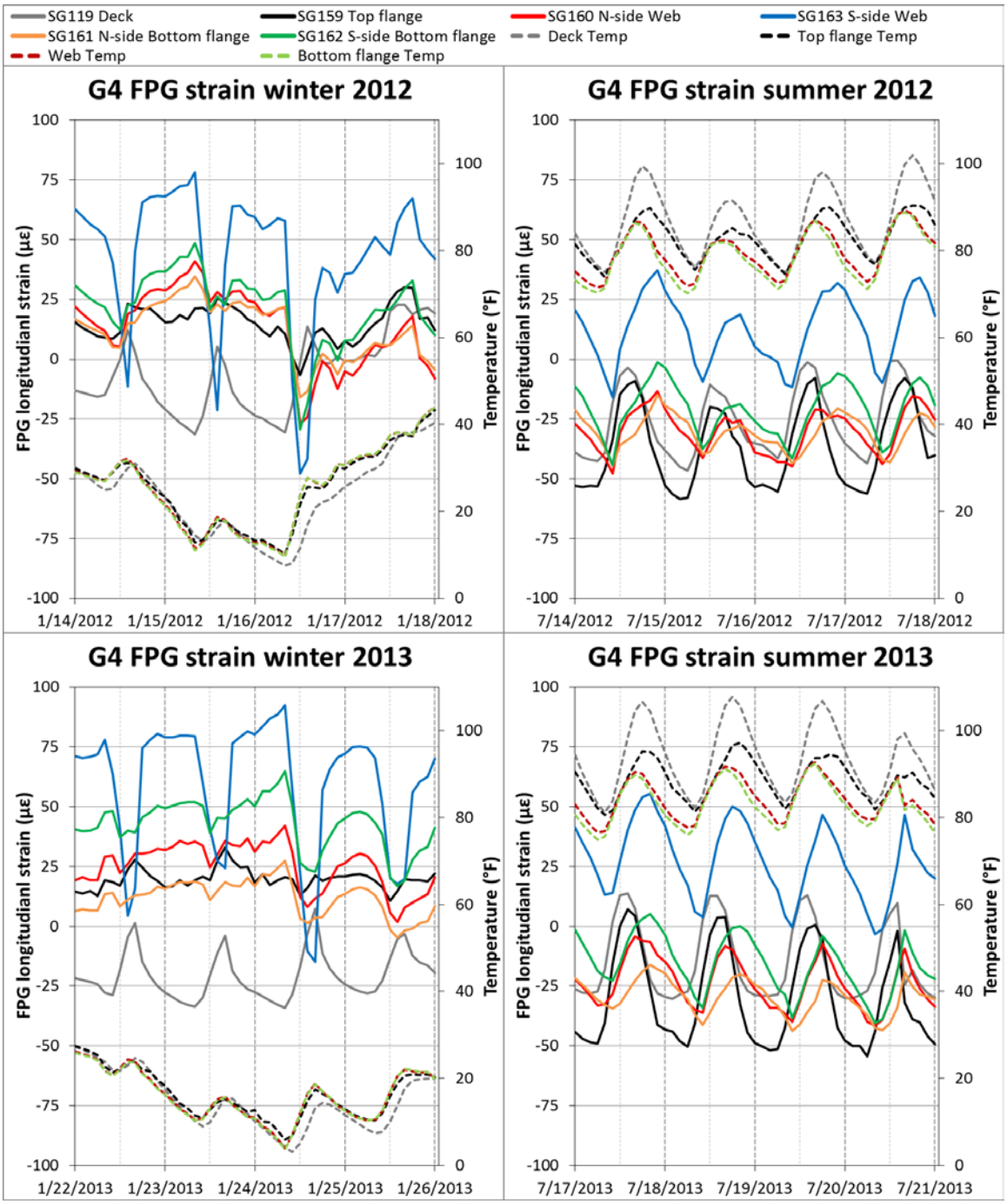

Figure 7-15 Longitudinal strain readings of girder 4 during the hottest and coldest 5 days in each year alongside with the temperatures fluctuation

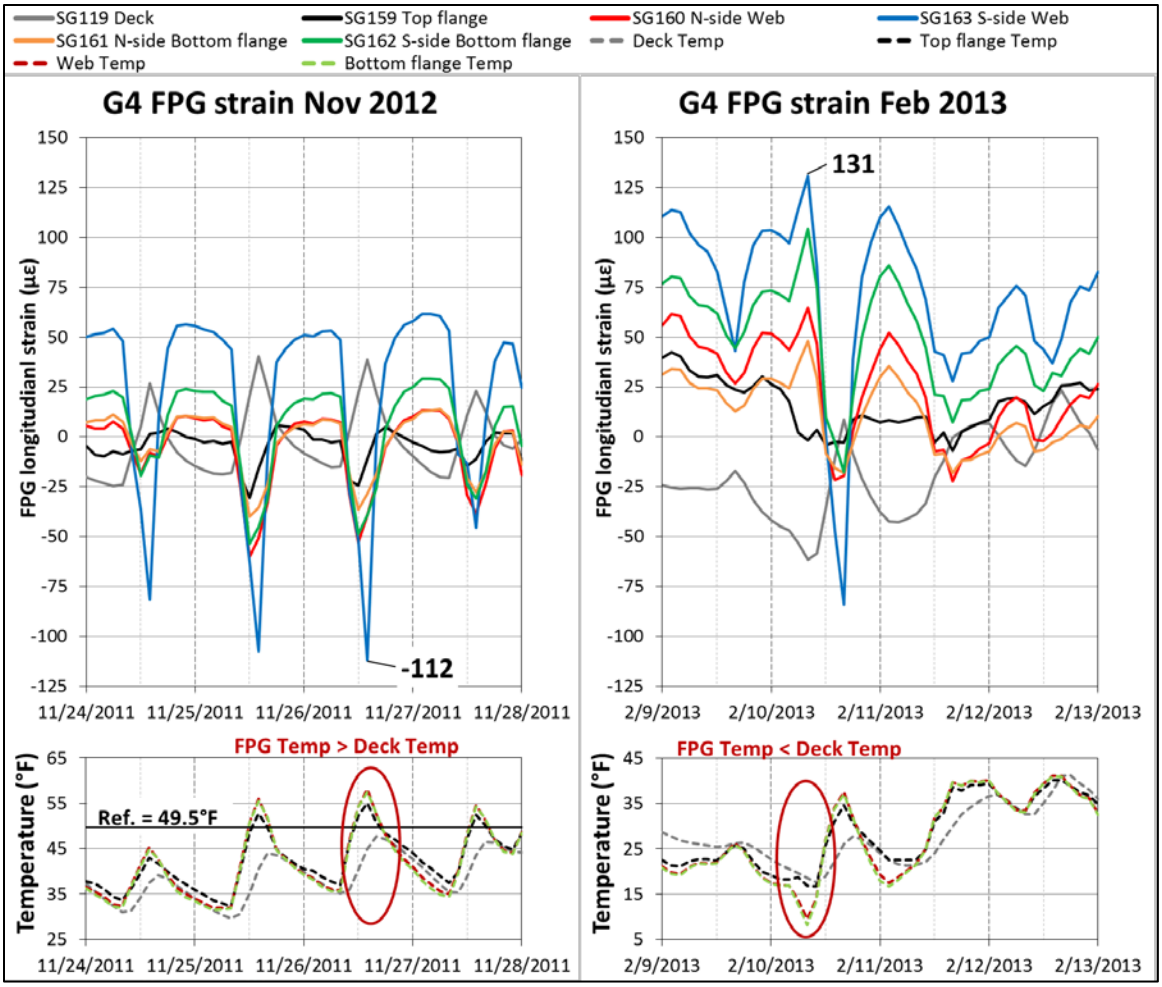

Figure 7-16 Maximum longitudinal FPG strain readings alongside with the temperature

In order to further confirm the effect of thermal gradient in the superstructure strain distribution, a daily cycle of temperature fluctuation during the hottest day in summer (07/18/2013) is analyzed using the FEM and compared to the field data in the form of strain profiles, the temperature on the hottest day is plotted in Figure 7-17. Since discrepancies were found in the exterior girders, the field strain data of interior girder G3 were used in the comparison. In the ANSYS model, the actual temperature changes recorded in the gauges of Girder 3 were applied, and 4 points on the daily thermal cycle were modeled. Point 1 is at 10 a.m.

when the temperature of the deck is similar to the girders and maximum compressive strain readings are recorded in the girders; point 2 is at 2 p.m. when the FPG top flange recorded the least compression; point 3 is at 6 p.m. when the FPG web record the least compression; and point 4 is at 10 p.m. when the FPG bottom flange record similar compression as the web and the top flange recorded the maximum compression of the day. Besides, since the maximum was found to be happened at spring/fall when a reverse thermal gradient existed (FPG girders are warmer than the deck during expansion and colder during compression), a point when maximum compressive strain is recorded (on 4/16/12 at 12 p.m.) in Girder 3 bottom flange is also modeled.

Strain profiles of field data and ANSYS results at the four points in summer are plotted in Figure 7-18 and values are listed in Table 7-10, and strain profiles at when maximum strain is recorded are plotted in Figure 7-19. In the two figures, "Δ" dots represent the field data while "+" dots represent the ANSYS results, and the "□" dots represent the field reading at the bottom of the deck which were calculated based on the top flange reading and the difference in coefficient of thermal expansion between the deck and FPG. Also, the temperature changes, the expected free strain, and the expected total strain were plotted alongside the mechanical strain (field data and ANSYS results). The expected free strains were calculated from the temperature changes and the expected total strains were calculated by summing up the calculated free strain with the measured mechanical strain. .

From Figure 7-18, the ANSYS results at point 1 to 3 are found to be very close to the field data while result at point 4 is not as good of a correlation but still

provides a similar strain distribution (shape). When the thermal gradient became larger (with the deck being warmer) the compressive strain in the FPG became smaller, while that in the deck became larger. This confirms that when the deck is being heated up by sun radiation, it expands more and causes more longitudinal displacement at the abutments, and in turn reduced the compression in FPG even though the rotation of the abutment increased.

From Figure 7-19, the ANSYS results are also found to be very close to the field data except at the deck and girder interface, which the model gives out larger compressive strain values than field data. This confirms that when reverse thermal gradient exist (the girders are warmer than the deck during expansion), the FPG expands even more and causes larger compression in the FPG and larger tension in the deck.

Nevertheless, by comparing point 3 (7/18/13 6:00 p.m.) in Figure 7-18 and Figure 7-19, shows that a smaller temperature change with a reverse/negative thermal gradient (the girders are warmer during expansion than the deck and colder during contraction) can result in larger strain values (more compressive at the bottom of FPG and more tensile at top of deck) compare to a larger temperature change with a positive thermal gradient (the deck is warmer during expansion than the girders and colder during contraction).

Note that the axial loads in all these points were found to be in the order of about 18 psi [0.12 MPa] (equivalent to 0.6 με in the steel girder), which is small and not significant.

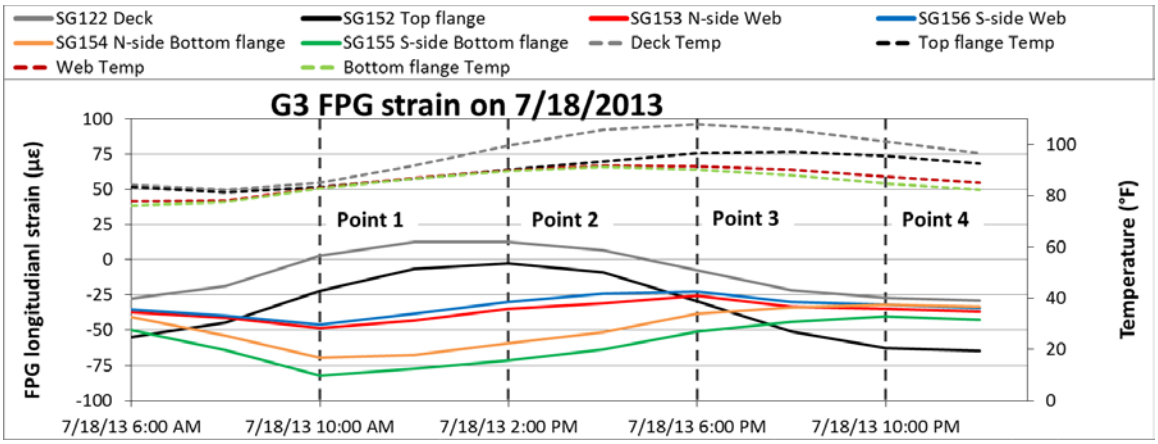

Figure 7-17 The 4 points on the daily cycle

Table 7-10 Field data readings and ANSYS results of Girder 3 at the 4 points of the daily cycle in summer

ANSYS result (με)	Deck	Bottom of deck	Top flange	N-side web	S-side web	N-side Bottom flange	S-side Bottom flange
Point1	7.21	14.76	-20.66	-42.36	-40.82	-64.13	-62.79
Point2	3.74	32.55	-11.71	-45.46	-42.74	-77.24	-75.04
Point3	-2.51	32.72	-19.25	-33.97	-30.09	-64.96	-62.07
Point4	-3.12	17.76	-32.33	-29.05	-25.44	-43.85	-41.26
Field data (με)	SG122	SG152'	SG152	SG153	SG156	SG154	SG155
Point1	2.66	12.21	-22.26	-48.44	-46.17	-69.74	-82.21
Point2	12.61	38.48	-2.44	-34.99	-29.91	-59.23	-71.65
Point3	-7.38	18.24	-29.31	-25.34	-22.39	-38.48	-51.17
Point4	-26.99	-15.18	-62.51	-34.78	-32.02	-31.93	-40.36

Table 7-11 Field data readings and ANSYS results of Girder 3 at when maximum compressive strain is recorded at spring

ANSYS result (με)	Deck	Bottom of deck	Top flange	N-side web	S-side web	N-side Bottom flange	S-side Bottom flange
ANSYS	21.712	-30.075	-56.075	-84.051	-82.653	-106.88	-104.61
Data	17.86	-6.00	-35.54	-79.59	-75.59	-107.05	-102.60

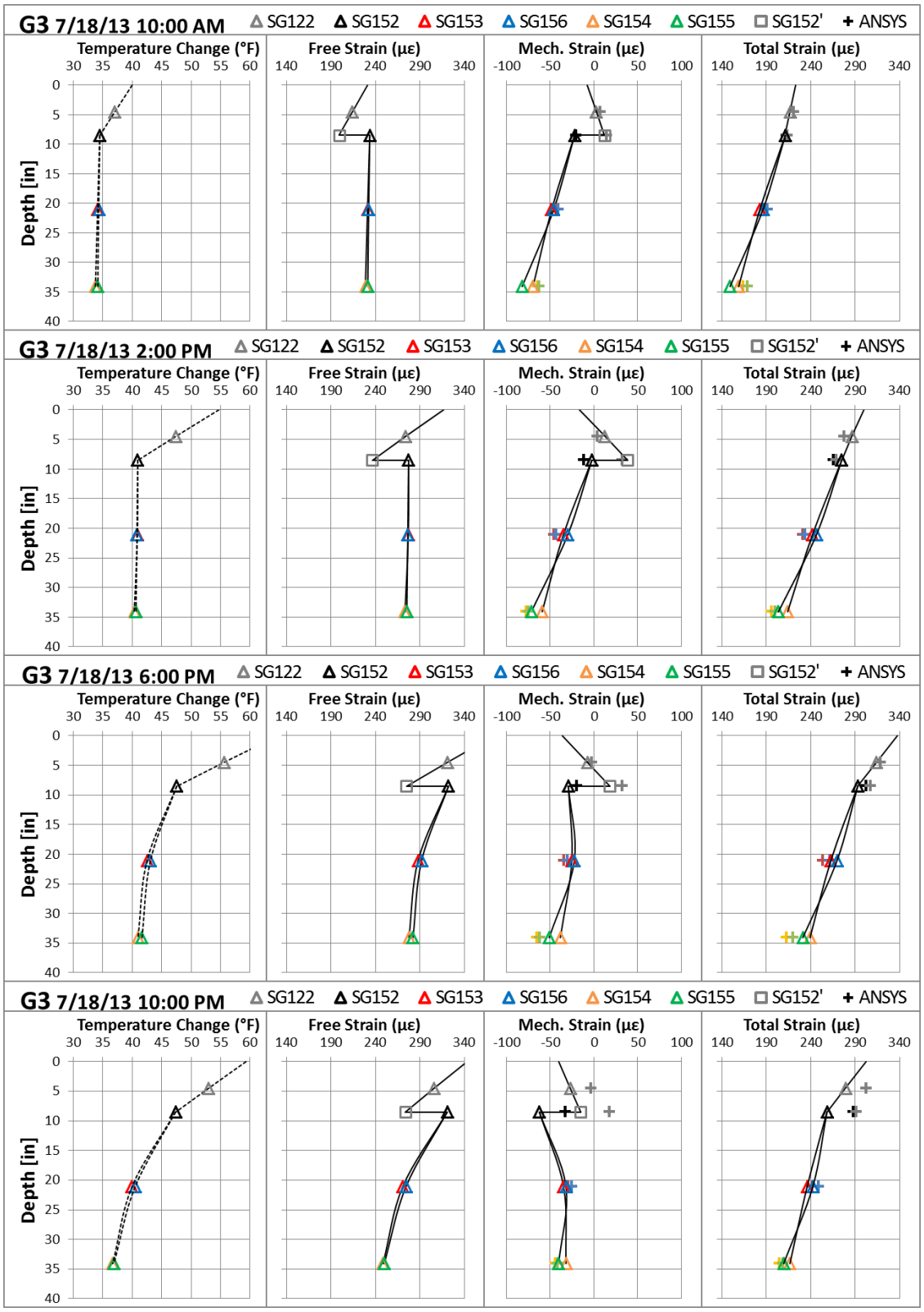

Figure 7-18 Strain profiles of field data and ANSYS results of Girder 3 at the 4 points of the daily cycle

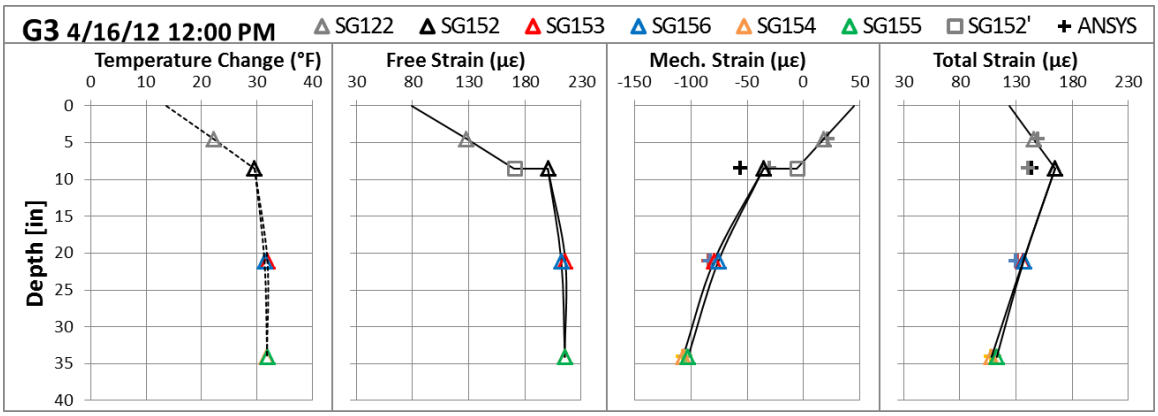

Figure 7-19 Strain profiles of field data and ANSYS results of Girder 3 at when maximum compressive strain is recorded at spring

7.3.5 Summary of superstructure longitudinal strain

The field FPG longitudinal strains readings show large variation versus temperature. Some discrepancies were found in the far north (SG144) and far south (SG163) web gauges. The presence of soil pressure (soil spring) in finite element model is important, but using different soil properties did not result in much variation in strain values and distribution. The ANSYS model is able to give quite close strain values to the field data in interior girder. Thermal gradient in the superstructure and the substructure greatly affects the longitudinal strains in this bridge, affecting the load distribution between exterior and interior girders, causing non-linear stress distribution along the depth of the cross-section, and changing the mechanical strain (or stress) distribution between the girders and the deck. It was found to be a significant factor in when maximum FPG strains were realized, though these maximum strains corresponded to stresses of less than 4 ksi.

CHAPTER 8
BRIDGE PERFORMANCE

A bridge survey was performed on 16th and 18th of December, 2013 to examine the actual bridge conditions. Cracks from 2 foot [61 cm] to 6 foot [183 cm] in length were observed on the center part of the bridge concrete deck. Due to snow coverage on the roadway shoulders the two sides of the deck (about 5 foot [152 cm] from edge) were not able to be examined. Cracks on the deck are shown in Figure 8-1. Also, the locations of the cracks were measured and they were found to be located directly above the FPG top flange edges. The locations and dimensions of cracks are shown in Figure 8-2. This indicates that the cracks were possibly initiated from the FPG-to-Abutments junction and propagate along the top of the FPG. Representatives from MassDOT indicated that this was likely due to improper curing of topping slab materials that included silica fume, though it is possible that the cracking would have initiated in the upper abutment cast in place sections. These cracks also led to leakage of water to the FPG below the deck as shown in Figure 8-3.

At the bottom flange of the FPG, shown in Figure 8-4, the corrosion shown appears to be at locations where blocking was provided during transport of the girders to the site and wore off the galvanizing coating. These damaged areas would require touch-up galvanizing coating per MassDOT specifications, but this does not appear to have been completed. This points out the importance of oversight and inspection on projects where new or non-typical construction processes or materials are used, as is increasingly typical on Accelerated Bridge Construction projects.

The interface between the cast in place upper abutments and the precast, prestressed lower abutments appears to be acting as a monolithic section as shown in Figure 8-5. Also, no obvious leakage was found at the closure pour looking from the bottom of the bridge, the closure pour condition is shown in Figure 8-6.

Figure 8-1 Cracks found on the concrete deck

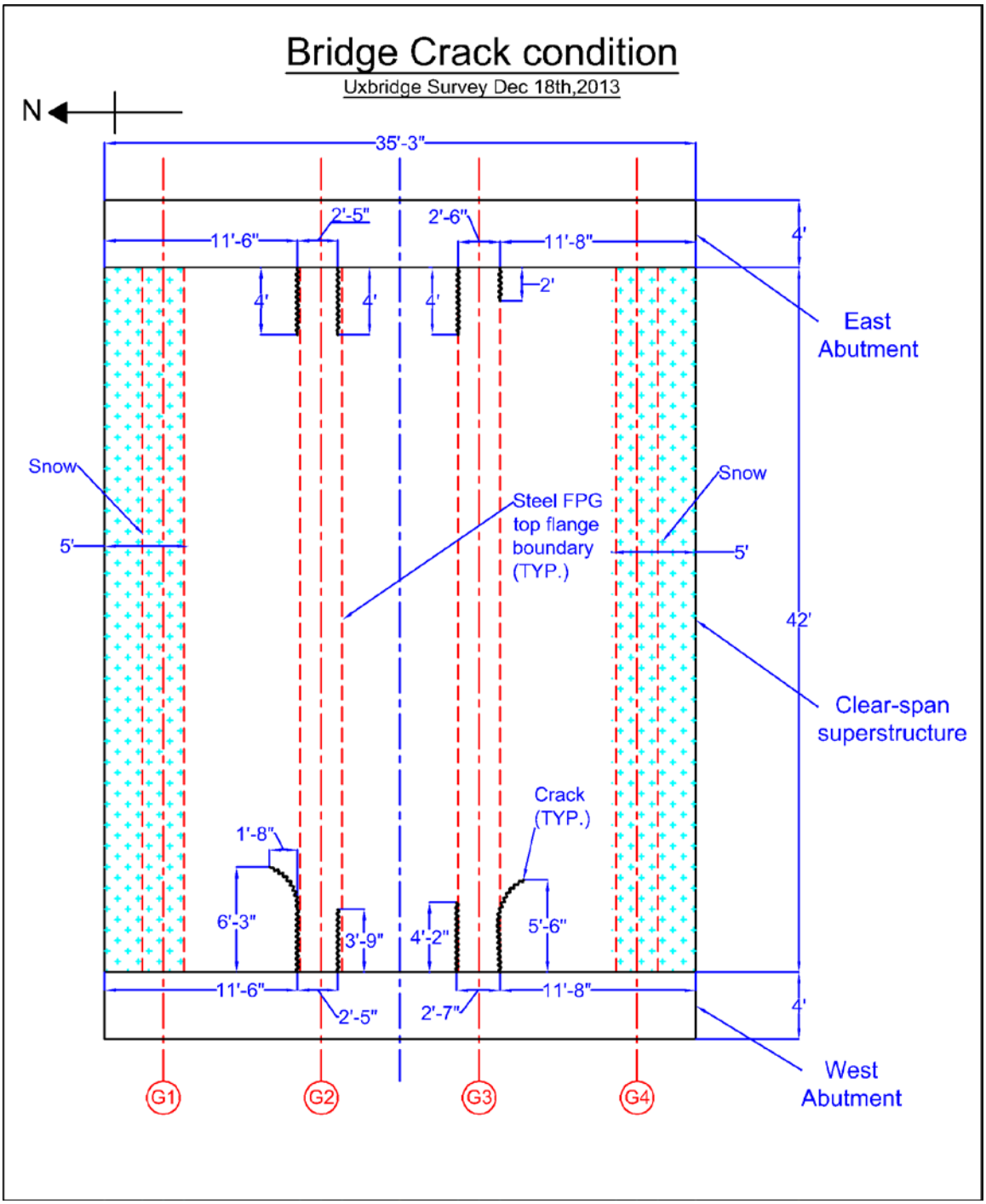

Figure 8-2 Cracks locations and dimensions

Figure 8-3 Leakage from top of deck to FPG

Figure 8-4 Rusts found at the bottom of FPG

Figure 8-5 Upper abutments to lower abutments interface condition

Figure 8-6 Closure pour condition

CHAPTER 9
CONCLUSION

Two years of field data and comparison with FEM on the live load testing and the seasonal behavior of the first Folded Plate Girder Bridge have been presented. Results from FEM and field data are concluded in the following:

1) The bridge is performing well and maximum steel girder strains recorded in the field data are -112 με (≡ 3.2 ksi [22.1 MPa] in compression) and 131 με (≡ 3.8 ksi [26.2 MPa] in tension) due to long term temperature effect and 52.1 με (≡ 1.5 ksi [10.3 MPa] in compression) due to the live load test after temperature correction. Whereas the maximum girder strain predicted by FEM due to live load test is 74.7 με (≡ 2.2 ksi [15.2 MPa] in compression) at the bottom flange-to-web junction where no gauge is instrumented.

2) Shear lag effects were present under concentrated loads and led to stress concentration at the web-to-bottom flange junction. Under self-weight and thermal loading, no significant shear lag effect is presented. The bottom flange tie-plates have effect in restraining the bottom flange from shear deformation and reduced the shear lag effect.

3) During summer (maximum temperature increase),FEM that included thermal gradient on the superstructure and the substructure, dense sand backfill soil properties and no soil resistance at the piles fitted abutment rotations field data values well.

4) During winter (maximum temperature decrease), FEM that included thermal gradient on the superstructure and substructure, dense sand soil properties

at both the backfill and the piles was the closest fit to field data abutment rotations but is still less than the field data values by about 50 percent.

5) Thermal gradient at the superstructure can significantly change the strain profile distribution of the bridge, whereas thermal gradient at the substructure can change the load distribution between exterior and interior girders.

6) For positive thermal gradient, (deck warmer than the girders during expansion and colder during contraction, typically happened at maximum temperatures in summer and winter), the FPG bottom flange will result in less compressive (during expansion)/tensile (during contraction) strain compare to the case when the temperatures at deck and girders are similar, or a negative thermal gradient. The maximum girder strains occurred at times when a negative thermal gradient was present on the structure.

BIBLIOGRAPHY

[1] Folded Plate Girder System, http://foldedplate.com/

[2] Narendra Taly, Design of Modern Highway Bridges, McGraw Hill, 1998.

[3] U.S. Government Accountability Office, http://www.gao.gov

[4] Folded Plate Girder System, http://foldedplate.com/

[5] Accelerated Bridge Program,
http://www.eot.state.ma.us/acceleratedbridges/default.htm

[6] American Galvanizers Association, http://www.galvanizeit.org/

[7] Mohannad HMA, Ghaidak AF. Effect of Stiffeners on Shear Lag in Steel Box Girders. Al-Khwarizmi Engineering Journal, Vol.8, No.2, 2012, pp 63-76.

[8] Chang ST and Zheng FZ. Negative shear lag in cantilever box girder with constant depth. Journal of Structural Engineering, Vol. 113, No.1, January 1987, pp. 20-35

[9] Kalayci E. Analysis of Curved Integral Abutment Bridges. Masters Theses~Paper 389. University of Massachusetts Amherst, USA.

[10] Civjan SA, Bonczar C, Brena SF, DeJong J, Crovo D. Integral abutment bridge behavior: parametric analysis of a Massachusetts Bridge. J. Bridge Eng. 2007

[11] Ting JM, Faraji S. Force–deformation testing for integral abutment bridges, University of Massachusetts Transportation Center, UMTC- 97-13, 1998.

[12] Baker RM, Duncan JM, Rojiani KB, Ooi PS, Tan CK, Kim SG, Manuals for the Design of Bridge Foundations. National Cooperative Highway Research Program (NCHRP), Transportation Research Board: Washington, DC, 1991.

[13] American Petroleum Institute. Recommended Practice for Planning, Designing and Constructing Fixed Offshore Platforms–Working Stress Design. American Petroleum Institute: Washington, DC, 1993.

[14] Bogard D, Matlock H. Simplified Calculation of p − y Curves for Laterally Loaded Piles. Unpublished Report, Ertec Inc., 1980.

[15] Ugural and Fenster, Advanced Strength and Applied Elasticity. 4th edition, Prentice Hall, 2003, pp83